AD-777 915

# STUDY OF ELECTRONIC TRANSPORT AND BREAKDOWN IN THIN INSULATING FILMS

Murray A. Lampert, et al

Princeton University

Prepared for:

Air Force Cambridge Research Laboratories

January 1973

ARPA Order No. 2180

Program Code No. 4D10

Contractor: Princeton University

Effective date of contract: 1 July 1972

Contract No. F19628-72-C-0298

Principal Investigator and phone no.
  Prof. Murray A. Lampert/609-452-4635

AFCRL Project Scientist and phone no.
  Dr. John C. Garth/617-861-4051

Contract expiration date: 30 June 1975

Qualified requestors may obtain additional copies from
the Defense Documentation Center. All others should
apply to the National Technical Information Service.

AD 777915

## DOCUMENT CONTROL DATA - R & D

*(Security classification of title, body of abstract and indexing annotation must be entered when the overall report is classified)*

| 1. ORIGINATING ACTIVITY *(Corporate author)* | 2a. REPORT SECURITY CLASSIFICATION |
|---|---|
| Princeton University<br>Department of Electrical Engineering<br>Princeton, New Jersey 08540 | Unclassified |
| | 2b. GROUP |

3. REPORT TITLE

STUDY OF ELECTRONIC TRANSPORT AND BREAKDOWN IN THIN INSULATING FILMS

4. DESCRIPTIVE NOTES *(Type of report and inclusive dates)*

Scientific. Interim.

5. AUTHOR(S) *(First name, middle initial, last name)*

Murray A. Lampert
Walter C. Johnson
Wilmer R. Bottoms

| 6. REPORT DATE | 7a. TOTAL NO. OF PAGES | 7b. NO. OF REFS |
|---|---|---|
| January 1973 | 95 | 22 |

| 8a. CONTRACT OR GRANT NO. ARPA Order No. 2180 | 9a. ORIGINATOR'S REPORT NUMBER(S) |
|---|---|
| F19628-72-C-0298 | Semi-Annual Technical Report No. 1 |
| b. PROJECT NO. Project Task, Work Unit Nos. | |
| 2180 n/a      n/a | |
| c. DoD Element    61101D | 9b. OTHER REPORT NO(S) *(Any other numbers that may be assigned this report)*<br>AFCRL-TR-73-0263 |
| d. DoD Subelement    n/a | |

10. DISTRIBUTION STATEMENT

A - Approved for public release; distribution unlimited

| 11. SUPPLEMENTARY NOTES | 12. SPONSORING MILITARY ACTIVITY |
|---|---|
| This research was sponsored by the Defense Advanced Research Projects Agency | Air Force Cambridge Research Laboratories (LQ)<br>L. G. Hanscom Field<br>Bedford, Massachusetts 01730 |

13. ABSTRACT

A comprehensive research program is under way for the characterization of electronic transport and dielectric breakdown properties of thin insulating films on Si which are technologically important, namely $SiO_2$, $Al_2O_3$, $Si_3N_4$ and their composites. The main experimental approaches are

i) Non-destructive breakdown of un-metallized films exposed to a corona discharge in a suitable gas (dry air, $N_2$, rare gas, etc.)

ii) Locally destructive, self-quenching breakdown of MIS capacitor structures.

iii) Optical charge - optical and thermal discharge studies of electronic traps in the films,

iv) Kilovolt electron-beam probe studies of the films, including damage induced by the beam,

Accompanying theoretical studies initially are concerned with Monte Carlo calculations of hot-electron distributions induced by high electric fields in the film. Very substantial progress was made on this problem, including:

i) the identification of useful scaling laws for constant mean-free-path problems, including anisotropy of scattering,

ii) demonstration of the usefulness of one-dimensional, random-walk simulations of three-dimensional problems, and

iii) development of a powerful graphical technique for studying distribution instability (runaway) induced by an energy-dependent mean free path.

DD FORM 1473 (PAGE 1)
1 NOV 65

S/N 0102-014-6600

i

| 14. KEY WORDS | LINK A | | LINK B | | LINK C | |
|---|---|---|---|---|---|---|
| | ROLE | WT | ROLE | WT | ROLE | WT |
| Electronic transport | 8 | 2 | | | | |
| Dielectric breakdown | 8 | 3 | | | | |
| Insulating films | 9 | 3 | | | | |
| Corona chrging | | | 10 | 3 | | |
| Nondestructive breakdown | | | 9 | 3 | | |
| Tunneling into oxide | | | 7 | 2 | | |
| Self-quenching breakdown | | | | | 8 | |
| Scanning electron microscopy | | | | | 10 | |

AFCRL-TR-73-0263

STUDY OF ELECTRONIC TRANSPORT AND BREAKDOWN
IN THIN INSULATING FILMS

by

Murray A. Lampert, Walter C. Johnson, Wilmer R. Bottoms

Princeton University
Department of Electrical Engineering
Princeton, New Jersey 08540

Contract No. F19628-72-C-0298
Project No. 2180

Semi-Annual Technical Report No. 1

January 1973

Contract Monitor: John C. Garth
Solid State Sciences Laboratory

ic

## Abstract

A comprehensive research program is under way for the characterization of electronic transport and dielectric breakdown properties of thin insulating films on Si which are technologically important, namely $SiO_2$, $Al_2O_3$, $Si_3N_4$ and their composites. The main experimental approaches are

i) Non-destructive breakdown of un-metallized films exposed to a corona discharge in a suitable gas (dry air, $N_2$, rare gas, etc.)

ii) Locally destructive, self-quenching breakdown of MIS capacitor structures.

iii) Optical charge - optical and thermal discharge studies of electronic traps in the films.

iv) Kilovolt electron-beam probe studies of the films, including damage induced by the beam.

Accompanying theoretical studies initially are concerned with Monte Carlo calculations of hot-electron distributions induced by high electric fields in the film. Very substantial progress was made on this problem, including:

i) the identification of useful scaling laws for constant mean-free-path problems, including anisotropy of scattering,

ii) demonstration of the usefulness of one-dimensional, random-walk simulations of three-dimensional problems, and

iii) development of a powerful graphical technique for studying distribution instability (runaway) induced by an energy-dependent mean free path.

## Table of Contents

## 1. Introduction

A comprehensive research program is under way for the characterization of electronic transport and dielectric breakdown properties of thin insulating films on Si which are technologically important ($SiO_2$, $Al_2O_3$, $Si_3N_4$ and their composites. Completely non-destructive breakdown of the film is readily achieved by charging the exposed (unmetallized) surface through either an impacting ion beam or a corona discharge in a suitable gas. We are concentrating on the corona discharge, which has two strong advantages: i) either sign of charging is equally convenient, and ii) there is negligible kinetic energy of impact. A direct comparison technique, employing a dummy metal sample, has been developed which makes it possible, for the first time, to measure the surface potential of the exposed film during steady-state charging. A special environmental chamber with desiccation capability and with gloves for manipulation of objects inside the chamber from the outside has been constructed for the systematic study of corona-induced breakdown under highly controlled conditions in a variety of suitable gases. A second technique for studying film breakdown employs thin metallization, leading to local removal of gate material, on the scale of microns, at the site of a breakdown, ending in an open circuit at that site. Thus, the breakdown is self-quenching. Initially, we are studying pyrolytically deposited $Al_2O_3$ films, of approximately 1000Å thickness, with gold metallization. A third technique for studying transport properties of the film is the charge-discharge technique. The charging of traps in the oxide film is done optically, either thru electron-hole pair generation throughout the film bulk by soft X-rays or by internal photoemission of electrons (or holes) into the film from either the Si substrate or the metal gate. The discharging of the traps is done either by heat (at elevated temperatures) or by sub-bandgap light. Initially, we are using these charge-discharge techniques to study thermally

grown $SiO_2$ films, both without further treatment and with ion
implants (Na and Al). The implants have been carried out to
controllably dope the oxide with electron traps and our interest
is accordingly focussed on the trapping properties of the films.
A fourth technique for styding electronic transport through the
films utilizes direct electron injection into the film by a
moderate-energy electron beam (energy in the low kilovolt
range). The beam probes the as-grown film and also probably
produces characteristic forms of damage (e.g. at the oxide-
substrate interface, and possibly throughout its range).
The latter will influence the I-V characteristic of the film and
can also be monitored by other, more standard techniques.
Results have been obtained with all four techniques and they are
presented in the appropriate sections. Since all of the
experimental results are preliminary at this stage they are
not highlighted in the present Introduction.

The above experimental programs are designed to
explore the film bulk and film-substrate interface influences
on transport and breakdown. These programs are complemented
by a program of film surface studies based on secondary electron
spectrometry. This spectrometry makes it possible to identify
atomic species on the film surface, to explore the chemical
environment of a species, to map out valence-band structure
for the host film in the neighborhood of the exposed surface,
and to determine near-surface plasmon and phonon energies. A
specially designed spectrometer has been built at Princeton
with both unusually high sensitivity (better than $10^{-3}$ monolayer
under optimum conditions) and excellent spatial resolution
limited only by the incident electron beam spot size.

The experimental programs are complemented by a
theoretical program aimed particularly toward elucidating the
physical mechanisms underlying film breakdown and the develop-
ment of simple models for the dynamical spatial and temporal
evolution of breakdown events. Initially we have made extensive
Monte Carlo calculations of the behavior of hot electrons at

high fields in the insulating films. We have shown that with a
constant (energy-independent) mean free path for energy-loss
scattering, there is always a stable hot-electron distribution,
no matter how anisotropic the scattering is, short of pure
(100%) forward scattering. We have developed scaling laws for
the average energy of the stable distribution and for the
spatial development distance of the distribution. We have
also successfully simulated the full three-dimensional problem
with highly simplified one-dimensional analogs. Finally, we
have shown that with an energy-dependent mean free path the
problem of stability (non-runaway) of the distribution can be
successfully analyzed by a very simple graphical method.

2. Non-Destructive Breakdown of Un-Metallized Films (Z. Weinberg
   collaborating)

   A. Background Discussion

        The study of charge transport in insulating films is
confronted with the problems of achieving controlled injection
of charge and avoiding destructive breakdown of the sample.
One solution to these problems which is being vigorously
pursued utilizes atomic or molecular ions to make direct
electrical contact to an exposed, unmetallized surface of the
insulator. Either a directed beam of ionized atoms may be
used, in which case a substantial ion kinetic energy must be
reckoned with, or alternately a gas discharge may be used, in
which case the ion kinetic energy will be negligible. A
negative gas ion that has an electron affinity smaller than that
of the insulator (which is on the order of 1 ev for the
insulators of interest) can, in principle, deposit its excess
electron directly into the conduction band of the insulator.
If electron trapping, at the exposed surface or in the film
bulk, is not too strong, the electron so injected can transport
through the film to the silicon substrate where it will be
collected. If the electron so injected is trapped at or near
the exposed surface, this surface will become charged. The
potential of the surface, during charging, can be monitored

continuously by means of a direct comparison technique which is described below. Immediately following cessation of charging the potential of the charged, exposed surface can be monitored with a vibrating Kelvin probe. Film breakdown induced by charging of the exposed surface is completely non-destructive because of the absence of lateral conductivity along the exposed surface; thus, weak spots, which are normally present in any capacitor structure, cannot discharge the electrostatic energy stored in the structure. Note that if a negative ion with electron affinity exceeding that of the insulator arrives at the exposed surface, the ion will deposit its excess electron directly into a localized surface state of the insulator, which may be the gas ion itself adhering to the exposed insulator surface. This situation is virtually equivalent to the above-discussed one, in which the electron is first injected into the conduction band of the insulator and then captured into a localized state at or near the exposed surface. In fact, it is very difficult to distinguish these two situations experimentally.

The situation with regard to the arrival of positive gas ions at the exposed insulator surface is complementary to that discussed above for negative ions. A positive gas ion which has a (neutral) ionization energy (as modified by image forces) that exceeds the sum of the electron affinity of the insulator and its band gap will offer an empty state (below the edge of the valence band of the insulator) to which an electron from the valence band can make a transition; thus a hole is injected into the valence band of the insulator, where it may be either trapped or mobile. If the hole is trapped at or near the exposed surface, this surface will become charged and its potential will rise. If the hole is mobile, it can be transported through the insulator into the back contact. Even after nearly a decade of MOS technology, elementary information[1] bearing on hole mobility in the valence band of $SiO_2$, including the possibility of self-trapping of the hole in

non-bonding oxygen orbitals,[2] is still lacking. If the
(neutral) ionization energy of the incident, positive gas ion
is smaller than energetically required for hole injection, the
positive charge of the ion will be deposited directly into a
localized surface state of the insulator, which (as in the neg-
ative ion case) may be the gas ion itself adhering to the
exposed surface. As before, the surface potential can be
monitored both during and after charging.

Two types of experiments have been initiated. One
of these employs a beam of positive noble gas ions in a vacuum.
The other uses ions formed in a corona discharge, of either
positive or negative polarity, in a gas of the chosen type at
approximately atmospheric pressure.

B.  Description of Experiments

For the noble-gas ion-beam experiments we have designed
and constructed the apparatus shown schematically in Fig. 1. A
plasma is produced in a noble gas by a low-voltage arc dis-
charge between a hot tungsten filament and an anode. The
arc is confined by a short, narrow canal with metallic walls,
and positive ions are extracted from the plasma through an
aperture in the wall.[3] The ions are focused into a beam by
a set of cylindrical lenses. The specimen chamber is evacuated
to the range of $10^{-7}$ - $10^{-6}$ torr by a turbo-molecular pump.
The noble gas is bled into the plasma chamber to provide a
pressure at which the mean free path is suitably small for
maintenance of the arc discharge. A rotating sample holder is
capable of carrying several samples and is equipped with a
feedback-controlled heater. We are installing a vibrating
Kelvin probe for the measurement of the surface potential of
the samples (as shown schematically at the bottom of Fig. 1).
With this equipment we can observe, nondestructively, the
current-voltage characteristics of insulating films and the
dynamics of surface charging and decay.

For the corona experiments we have constructed the
equipment shown schematically in Fig. 2a. A high voltage, of

FIGURE 1. ION BEAM SYSTEM

GOLD PLATED
NEEDLE

HIGH VOLTAGE
SUPPLY

SHIELDS

**a.** CORONA SOURCE.

KEITHLEY
610B

SAMPLE

METAL
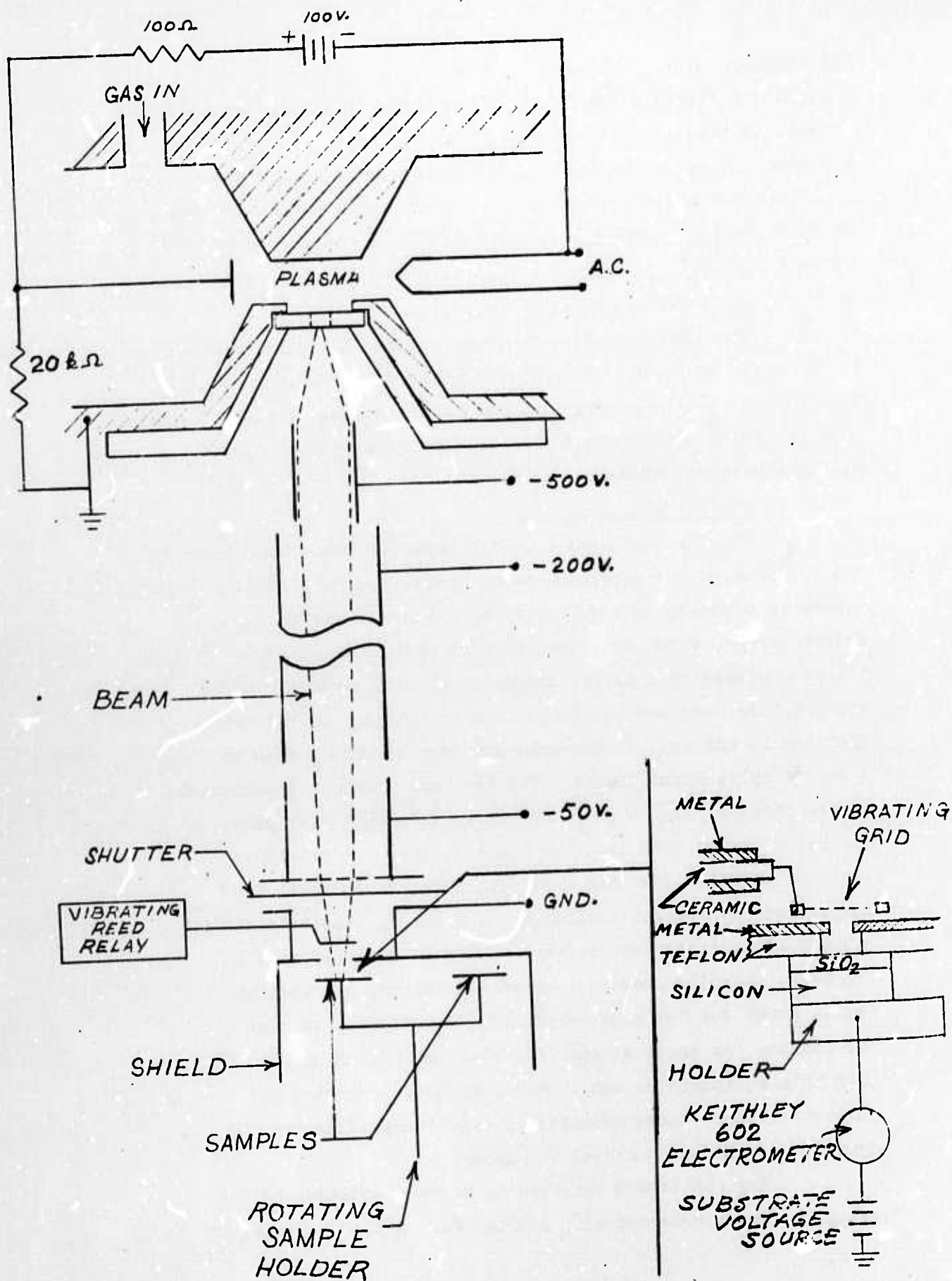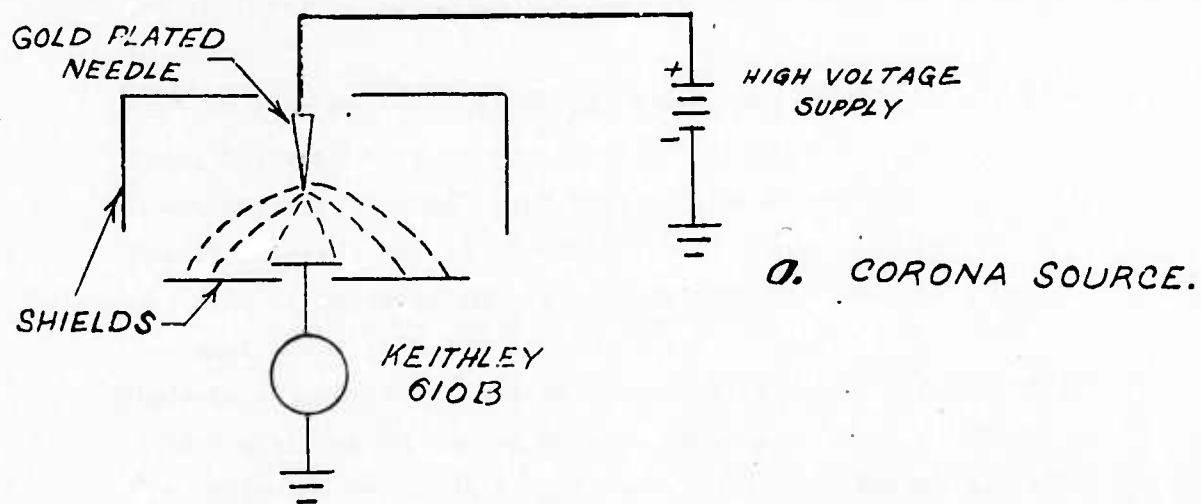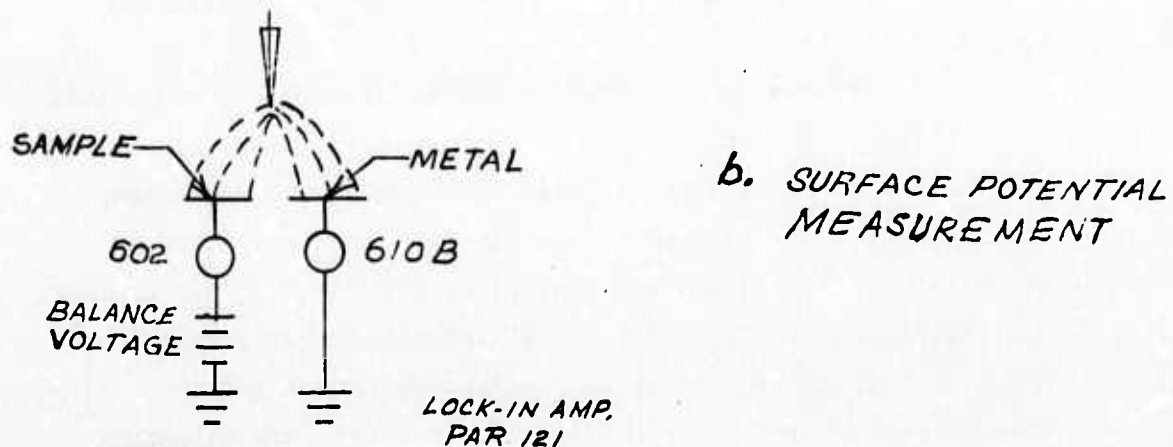
**b.** SURFACE POTENTIAL
MEASUREMENT

602

610B

BALANCE
VOLTAGE

LOCK-IN AMP.
PAR 121

VIBRATION

BUCKING
VOLTAGE
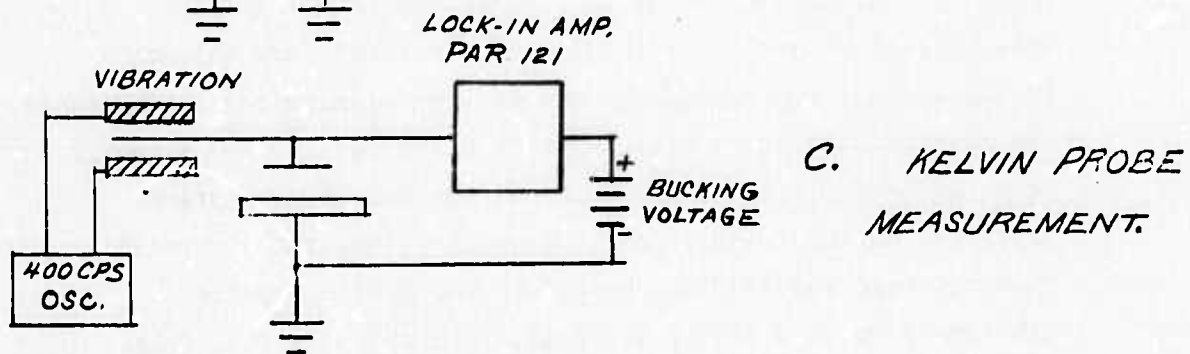
**c.** KELVIN PROBE
MEASUREMENT.

400 CPS
OSC.

CAPACITANCE
METER
BOONTON 72A.
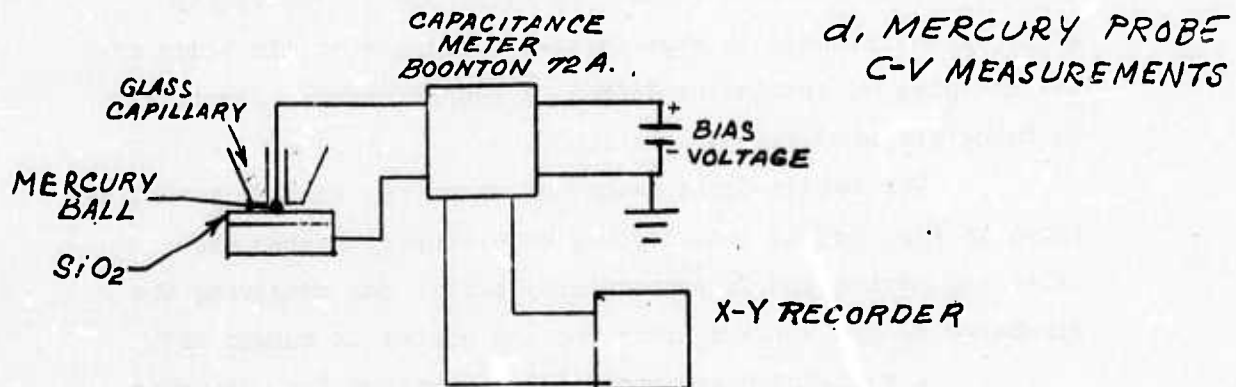
**d.** MERCURY PROBE
C-V MEASUREMENTS

GLASS
CAPILLARY

BIAS
VOLTAGE

MERCURY
BALL

$SiO_2$

X-Y RECORDER

FIGURE 2. CORONA SYSTEM

either positive or negative polarity, is applied to a needle electrode and produces a corona discharge in a selected gas at approximately atmospheric pressure. Ions of the corresponding sign are drifted to the sample by the electric field. Inasmuch as the mean free path is of the order of $10^{-5}$ cm, the ions are continuously thermalized and strike the sample with only the very small kinetic energy corresponding to their temperature. The negligible energy of impact avoids a host of complications which are just beginning to be appreciated,[4] and constitutes a marked advantage for the corona deposition technique.

The surface potential of the sample under steady-state current-flow conditions can be determined by a direct comparison scheme in the manner shown in Fig. 2b. The sample and a test plate are arranged in symmetrical manner. When the surface potentials of the sample and test plate are unequal, the asymmetry introduced into the electric field distribution will cause the drift of ions to be unequal to the two electrodes and an unbalance in current will result. The currents are balanced by adjusting the potential of one of the two electrodes, whereupon the potential of the sample and test plate can be read directly from the test plate. This technique for measuring surface potential during steady-state (or quasi-steady-state) current flow has been successfully tested in our Device Physics Laboratory on such widely different insulators as $SiO_2$ films and thermoplastic-resin films. We feel that it represents an important advance in experimental technique in the study of the charging of insulating films. A report on the technique is being prepared for publication.

The Kelvin-probe method of measuring surface potential, shown in Fig. 2c, is considerably more sensitive than the balancing method and is particularly useful for measuring the discharge of the surface after the ion source is turned off.

A well-known and convenient technique for measuring

MOS flatband voltage involves the use of a mercury probe, as illustrated in Fig. 2d. A bead of mercury projects from a glass capillary tube which is carried on micromanipulators, and this is used to provide a temporary metallic contact to the surface of the insulator without the need for conventional evaporated metallic field plates which would have to be removed and replaced various times during the course of the experiments. The flatband voltage directly gives the total charge stored in the insulator in the bulk and near the silicon interface.

### C. Experimental Results

At the present time our efforts are being concentrated on the corona discharge studies. At the outset, several interesting results have been obtained. We have found that when an $SiO_2$ film, thermally grown on a silicon substrate, is charged by corona in air, the field strength at breakdown depends on the polarity of the discharge, and is approximately $7 \times 10^6$ V/cm for positive corona and $1.3 \times 10^7$ V/cm for negative corona. These results are in agreement with independent measurements recently made at RCA Laboratories.[5] Further, our measurements of MOS flatband voltage show that after charging with negative corona, the $SiO_2$ has a positive accumulation of charge amounting to approximately $5 \times 10^{12}$ charges/$cm^2$, such as would occur if holes were injected from the silicon into the valence band of the insulator and were trapped. (Note that this result does not establish the identity of the dominant current-carrier in the oxide). Charging by positive corona in air results in a high-frequency (1 MHz) C-V curve that shows an unusually slow transition from accumulation to inversion. This effect has been attributed in the past to the presence of interface states,[6] but recent evidence indicates that it may be the result of lateral inhomogeneities in a distribution of impurity ions at the insulator-semiconductor interface,[7] these ions perhaps having been driven inward from the free

surface of the insulator by the high field established by the positive charge deposited by the impacting positive gas ions.[8] Identification of the mechanism involved here may be done by use of a-c conductance measurements made as a function of gate voltage on the MOS structure,[9] and we plan to pursue this line of attack at a later point in our investigations.

Breakdown measurements made on $SiO_2$ films by charging them from a negative corona in a nitrogen atmosphere indicated a breakdown field that was approximately 30% smaller than for the corresponding charging in air, whereas for charging from a positive corona the breakdown fields were the same for the two gases. This is a preliminary indication that for positive surface potentials the current through the silicon dioxide is controlled by the properties of the silicon/silicon-dioxide interface, presumably by the tunneling of electrons from the silicon into the conduction band of the silicon dioxide where they are transported to the exposed surface without strong trapping. In these experiments, if holes were injected into the valence band of the oxide (and this depends on the impinging ion species, as discussed above) they were rapidly trapped at or near the exposed surface. The identification of the impinging ion species in these early experiments is not certain because of the important role of impurities in the corona charging of insulator surfaces. Thus Shahin[10] found that the ion species critical for surface charging by corona in air are those deriving from trace constituents, namely $CO_3^-$ for negative charging and $(H_2O)_n H^+$ for positive charging.

We have concluded that the corona charging technique has a very high potential indeed for the elucidation of the electronic behavior of the oxide, and other insulating, films on silicon. However careful control of the discharge conditions is necessary. Therefore we have had constructed an environmental chamber with an air lock for the introduction and removal of samples and with provision for controlled circulation of the

ambient gas through a desiccator. Manipulation of the sample
and of probes can be achieved from the exterior via the use of
suitable gloves provided with the equipment. This chamber
will provide the required control of the ambient gas and will
enable us to make a comprehensive study of effects related
to the properties of different species of gas ions. In
addition to air and nitrogen, corona charging studies will be
made in $CO_2$, $SF_6$, argon and neon. These studies will be made
on $Al_2O_3$ and $Si_3N_4$ films on Si as well as on $SiO_2$ films, and
on composites of these films.

3.  Locally Destructive, Self-Quenching Breakdown of the Films
    (D. Y. Yang collaborating)

In the self-quenching technique of observing events
associated with insulator breakdown, a very thin metallization
of the top surface is used. A local breakdown event in the
insulator causes the metal in the immediate vicinity of the
fault to be removed by either vaporization, melting flow or
blow-out, thus achieving two results: the damage to the
insulator is confined to a very small area (of micron
dimension), and the removal of the metallic electrode from the
vicinity of the fault establishes an open circuit, which permits
one to continue testing the remainder of the sample.[11,12]
We have embarked on a program of experiments to utilize this
technique systematically in the study of breakdown in $SiO_2$,
$Al_2O_3$, and $Si_3N_4$ films and their composites. We have designed
and constructed a ramp-voltage generator which can be cycled
(i.e., produce breakdowns) at rates in the range of 1 to 100
per second. A sample holder has been built which provides
sample temperatures in the range of 77 to 500°K.

Preliminary measurements have been made at room
temperature on $Al_2O_3$ films pyrolytically deposited to a
thickness of approximately 1000Å on silicon substrates with
resistivities of approximately 1 ohm-cm and with gold contacts.
With the contact biased negatively, locally destructive breakdown
events were observed at field strengths of approximately

$1.1 \times 10^{7}$ V/cm for n-type substrates and $8.8 \times 10^{6}$ V/cm for
p-type substrates. When the gold contact was biased positively,
however, an unusual difference was observed between the results
obtained with the two substrates: for an n-Si substrate,
locally destructive breakdown events were observed at a field
strength of $8.7 \times 10^{6}$ V/cm, whereas for the p-Si substrate
there were no localized breakdown events at all, but, instead,
at field strengths approaching $8 \times 10^{6}$ V/cm the sample began to
conduct a comparatively large current which thereupon evaporated
the entire gold electrode. Measurement of the MOS flatband
voltage showed, for both n and p substrates, negative insulator
charging after breakdown produced with the gold contact positive,
and positive insulator charging after breakdown with the gold
contact negative. These results suggest that in both
polarities the breakdown is initiated by carrier injection from
the Si substrate into the oxide film.

The surface of each sample was observed through an
optical microscope during a sequence of breakdowns. Locally
destructive breakdown events were observed to produce removal
of metallic electrode over areas with diameters of a few
microns. We plan to examine samples which have undergone self-
quenching breakdown experiments in the chamber of the Princeton
high-resolution scanning electron microscope. This will allow
monitoring of the overall, as well as the local, state of the
sample as the number of breakdowns increase: the topography
of the sample, the induced current image, the surface composition
(Auger spectra), and the bulk composition (X-ray fluorescence),
all of which can be recorded on film to a high degree of
spatial resolution.

The difficulty of achieving direct experimental
observation of a local breakdown event is immediately evident
if we note that: i) the entire event is completed on a time
scale of a hundred nanoseconds or tens of nanoseconds, or even
less, depending on the particular structure, and ii) the lateral

spatial extent of the event is on the order of microns at most, and possibly much smaller in its earlier stages, and iii) until possibly well along in its individual history, the entire breakdown event is probably 'buried' underneath the electrode. With regard to the first point, sufficiently fast electronics is available to study the time evolution of a single breakdown event. Indeed in 'constant-voltage' mode studies of self-quenching breakdown of $SiO_2$ films on Si, electrode potential vs. time ($V(t)$ vs. t) was followed during a single breakdown event by Klein.[13] We believe that, by careful design of the experiment, it will be possible to obtain both $V(t)$ vs. t and $I(t)$ vs. t during a single breakdown event, hence also I vs. V. Such information, previously unavailable, will be a powerful aid in both developing and checking theoretical models for the breakdown. Another line of experiments, also not previously carried out, which we expect to yield valuable information on the second point above (the spatial extent of the local breakdown current) involves study of the local breakdowns in the scanning electron microscope for a series of almost identical samples, differing only in the thickness of metallization. A thickness range from approximately 100 to 2000Å will be employed. A third series of new experiments, also on our agenda for later undertaking, involves the study of laser-induced breakdown in the film.

4. <u>Charge-Discharge Studies of Trapping in the Films</u> (N. Johnson collaborating)

   A. <u>Background Discussion and Experiments</u>

   In this portion of our research effort we are studying the properties of deep traps in the insulating films by the technique of first charging the traps with carriers and then selectively detrapping the carriers, either by photon energy or thermally, from traps that are located progressively deeper in the forbidden gap.

   A particularly useful version of the charge-discharge technique, known as the method of Transient Polarization Currents,

was originally used by von Hippel et al for the alkali halides[14] and later by Tabak and Warter[15] for amprphous selenium. This technique eliminates the need for injecting contacts and requires, in fact, a blocking contact, the latter being far easier to obtain on an insulator. The traps in the insulator are first charged, for example by irradiation of the insulator with supra-bandgap UV photons to create hole-electron pairs with subsequent trapping, or alternatively by injection of charge carriers into the insulator by internal photoemission from a contact or by avalanche injection from the semiconductor substrate. Subsequent to the charging of the traps, a step of voltage is applied across the insulator. This results in a transient current as the traps are emptied of carriers (it is here that the blocking contact is required). If the voltage is sufficiently large so as to sweep all free carriers continuously from the sample, the resulting current for a single discrete trapping level is given by

$$ i(t) = \frac{qALN_t}{2\tau} \ e^{-t/\tau} \qquad , \qquad (1) $$

where q is the magnitude of the electronic charge, A is the area of the blocking contact, L is the thickness of the sample, $N_t$ is the density of the traps, and $\tau$ is the average time for emission of a trapped carrier. For purely thermal emission from the traps,

$$ \tau = \frac{1}{<\sigma v> N_c} \ e^{\Delta E/kT} \qquad , \qquad (2) $$

where $\sigma$ is the capture cross section of the trap, v is the carrier velocity, $<\sigma v>$ is the average over the free-carrier distribution function of the product $\sigma v$, $N_s$ is the effective density of states in the conduction band (assuming that the emitted carriers are electrons), $\Delta E$ is the energetic depth of the trap below the edge of the conduction band, k is the Boltzmann constant, and T is the absolute temperature.[16]

The foregoing expressions have been written for a single trapping level. In general, there may be a set of discrete levels or perhaps a continuum of levels. To examine these, the experiment is repeated at each of a set of successively higher temperatures to explore the traps that lie progressively deeper in the forbidden gap.

If the sample is irradiated with light having $h\nu \gg \Delta E$ during the progress of the transient, the emission of carriers will be enhanced above the thermal rate, i.e., the depth of the trap is effectively reduced in value. This is a particularly convenient technique for investigating traps which are relatively deep in the gap, and avoids the use of temperatures at which ionic currents would become appreciable. In studying wide bandgap insulators there is no problem whatever in obtaining light of sufficient intensity to dominate the thermal emission process. The minimum value of photon energy required for emission provides a further measure of $\Delta E$. The use of light, instead of temperature, to de-trap the electrons makes it possible to do the entire experiment at a fixed temperature, say room temperature or even lower. The range of trap energies in the forbidden gap which can be scanned by this optical technique is far greater than that which can be scanned by the conventional temperature technique.

B. Experimental Results

Typical results obtained by the use of this technique are shown in Figs. 3 and 4. Figure 3 shows the temperature controlled transient current obtained with a 4000A sample of $SiO_2$ on a substrate of n-Si with an Al field plate. The traps were first populated by irradiating the insulator with soft (5 kV) X-rays. In this example, the sample was held at a temperature of 75°C and a step of 10 volts (substrate negative) was applied. As evidenced by the straight-line segment on the semi-log paper, the transient was exponential over most of the time range. (Shallower traps can be seen emptying for t < 2 min.) Application of Eq. (1) yields the following results for this set

Figure 3.

Radiation-Induced
Transient Current

Sample HH-74-D
Temp. = 75°C
$V_{Si} = -10^{\underline{v}}$
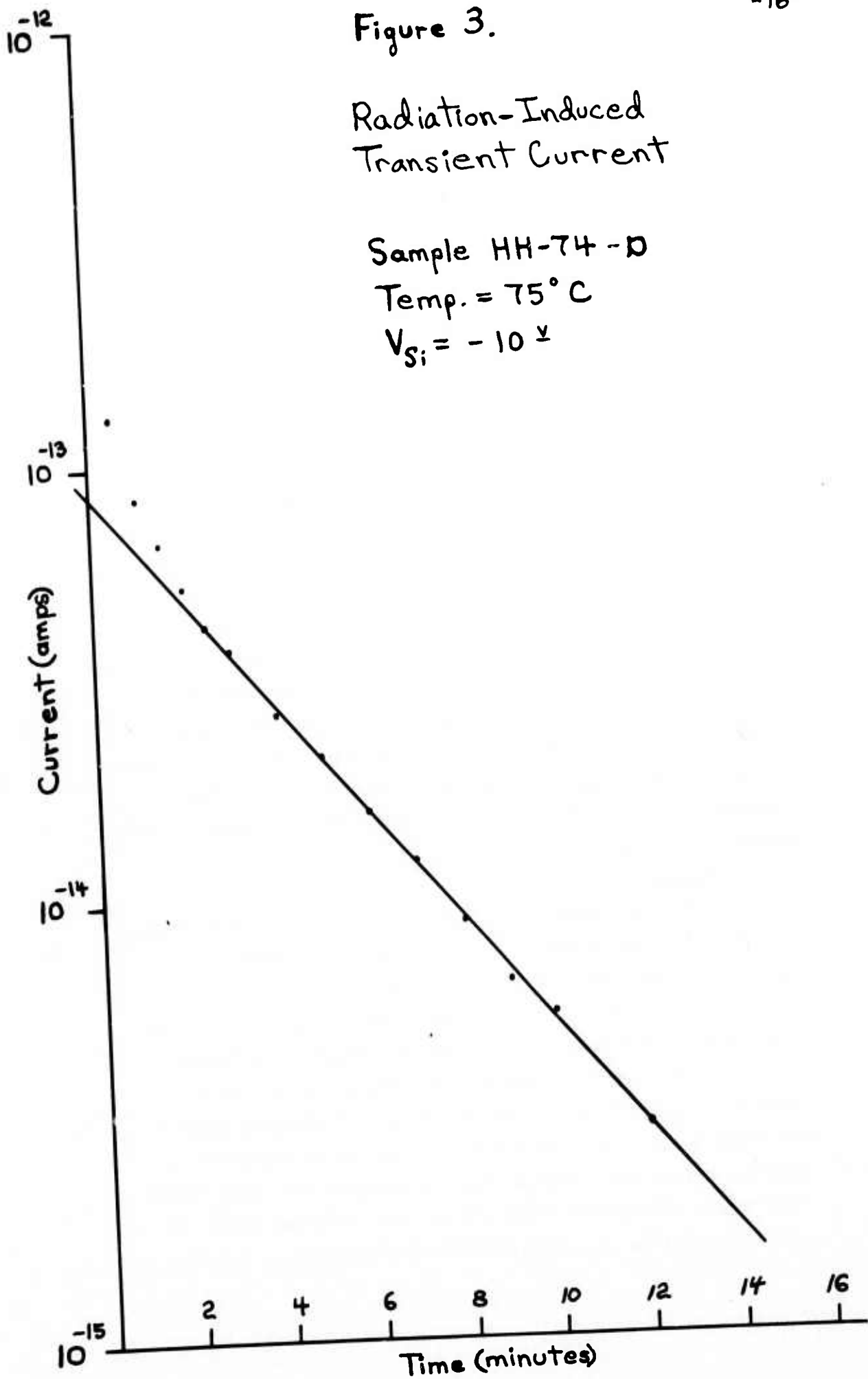
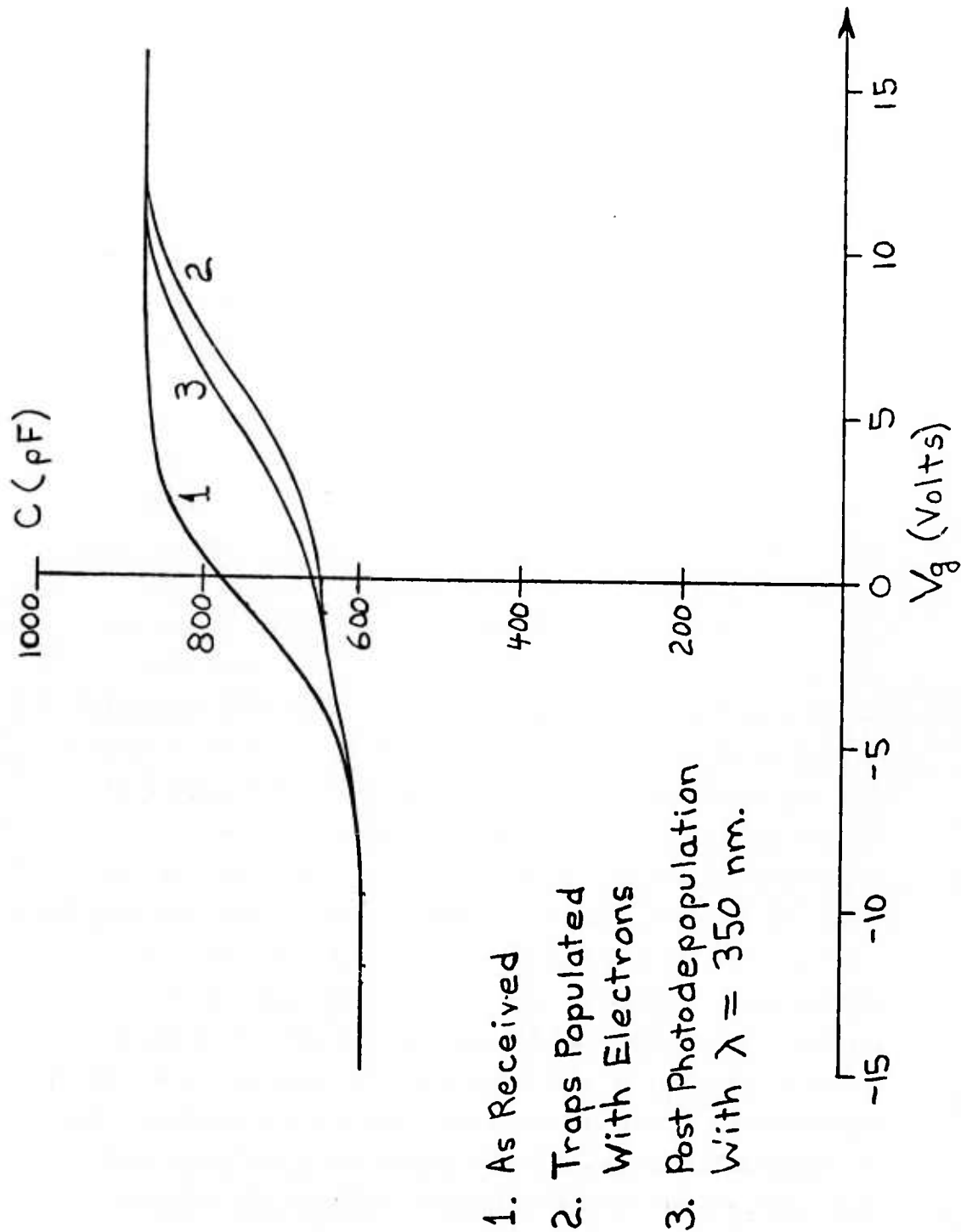Fig. 4. Capacitance vs. Applied Voltage (Sample HH-25-Na)

of traps: $N_t = 1.1 \times 10^{14}$ cm$^{-3}$ and $\tau = 2.2 \times 10^2$ sec. If we assume the reasonable values $\sigma \sim 10^{-15}$ cm$^2$, $v \sim 10^7$ cm/sec, and $N_c \sim 10^{19}$ cm$^{-3}$, the use of Eq. (2) yields the depth of the trap: $\Delta E \simeq 0.9$ eV. (The value of $\Delta E$ is not particularly sensitive to the exact values chosen for $\sigma$, $v$, and $N_c$.) The value of $\Delta E$ can be confirmed in two ways: either optically, or from the slope of log $\tau$ vs. 1/T. The confirmed value of $\Delta E$ can be used to check the value used for $\sigma$.

Another series of experiments were performed on a 3500Å sample of SiO$_2$ thermally grown on an n-Si substrate and implanted with sodium ions to a dose of $10^{15}$ cm$^{-2}$. The implantation energy was 20 kV, which produces a gaussian distribution of sodium atoms with the peak located about 400Å deep and with a half width of approximately 500Å. In this experiment the traps were populated by the internal photoemission of electrons from the substrate into the insulator, using light of the proper photon energy and a semitransparent field plate. The transient polarization current was produced at room temperature, using a bias of 24 volts (substrate negative). The sample was irradiated with light during the progress of the transient, and the intensity of the light was such that photon-stimulated emission dominated thermally-stimulated emission. Determination of the flat-band voltage from high-frequency (1 MHz) C-V tests provided a measure of the charge stored in the insulator. The results of C-V measurements are shown in Fig. 4. Curve 1 was taken on the sample as received. Curve 2, which was taken after charging the traps with electrons, shows a positive flat-band shift of approximately 6 volts, indicating the deep trapping of electrons. In producing the transient current using photon-enhanced emission, it was found that a minimum photon energy of approximately 3.5 eV was required. Curve 3 was obtained after the transient, during which the sample was illuminated with light with the aforementioned photon energy. The negative shift of flat-band voltage of approximately 1.3 volts indicates

that a fraction of the traps released their electrons during
the transient and are therefore located at a depth of 3.5 eV
or slightly shallower, but the majority of the traps retained
their charge and are therefore deeper in the gap than 3.5 eV.
After the current decayed to the background level, shutting
off the illumination and then reapplying it produced no
further effect; hence the traps at the 3.5 eV depth must be
considered to be empty. The experiment is repeatable in that
the traps can be charged and discharged repeatedly with
reproducible results.

If, for simplicity of analysis, we assume a
rectangular distribution of traps that extend to a depth of
600Å into the oxide (corresponding roughly to the distribution
of sodium atoms), computation shows that the flat-band shift
from Curve 2 to Curve 3 of Fig. 4 indicates a density of traps
of approximately $10^{17}$ cm$^{-3}$ at a depth of 3.5 eV or slightly
shallower. This corresponds to a number of traps per unit area
that is slightly less than $10^{12}$ cm$^{-2}$. This is considerably
smaller than the dosage of sodium ions, which was $10^{15}$ cm$^{-2}$.
At this time it is a matter of conjecture whether the electron
traps observed here are due to the displacement damage caused
by implantation or are caused by the sodium atoms directly. If
it is the latter, only a small fraction of the sodium atoms
are active in the trapping process. Note that with an
implantation dose of $10^{15}$ Na ions/cm$^2$ a maximum of approximately
1%, namely $10^{13}$/cm$^2$, can remain unneutralized, even during the
implantation. This is because the oxide breakdown field
($5 \times 10^6$ to $10^7$ V/cm) is reached at the latter concentration.
Thus, field-induced electron injection into the oxide must take
place throughout virtually the entire period of the implantation.
This is a complication requiring further investigation.

Examples of results obtained using another version
of the charge-discharge technique are shown in Figs. 5 through 7.
The sample here consisted of a film of SiO$_2$ thermally grown to
a thickness of approximately 1000Å on an n-Si substrate and

Fig. 5. Shifts of the C-V Curve Resulting from Electron Photoinjection at Progressively Higher Gate Biases.
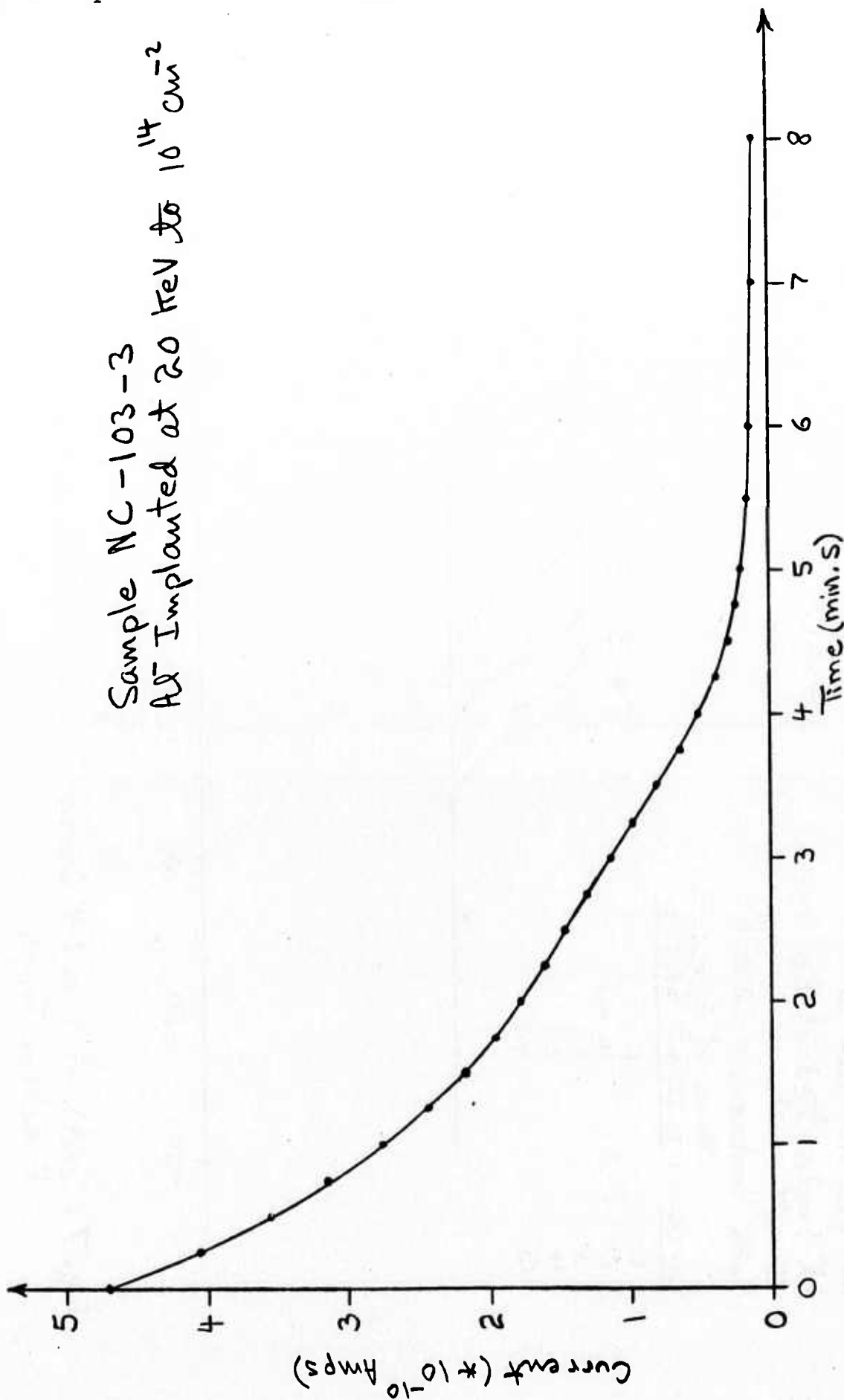
Fig. 6. Electron Injection Transient Current for Sample As Received with $V_g = +10 V$ and $\lambda = 250$ nm.
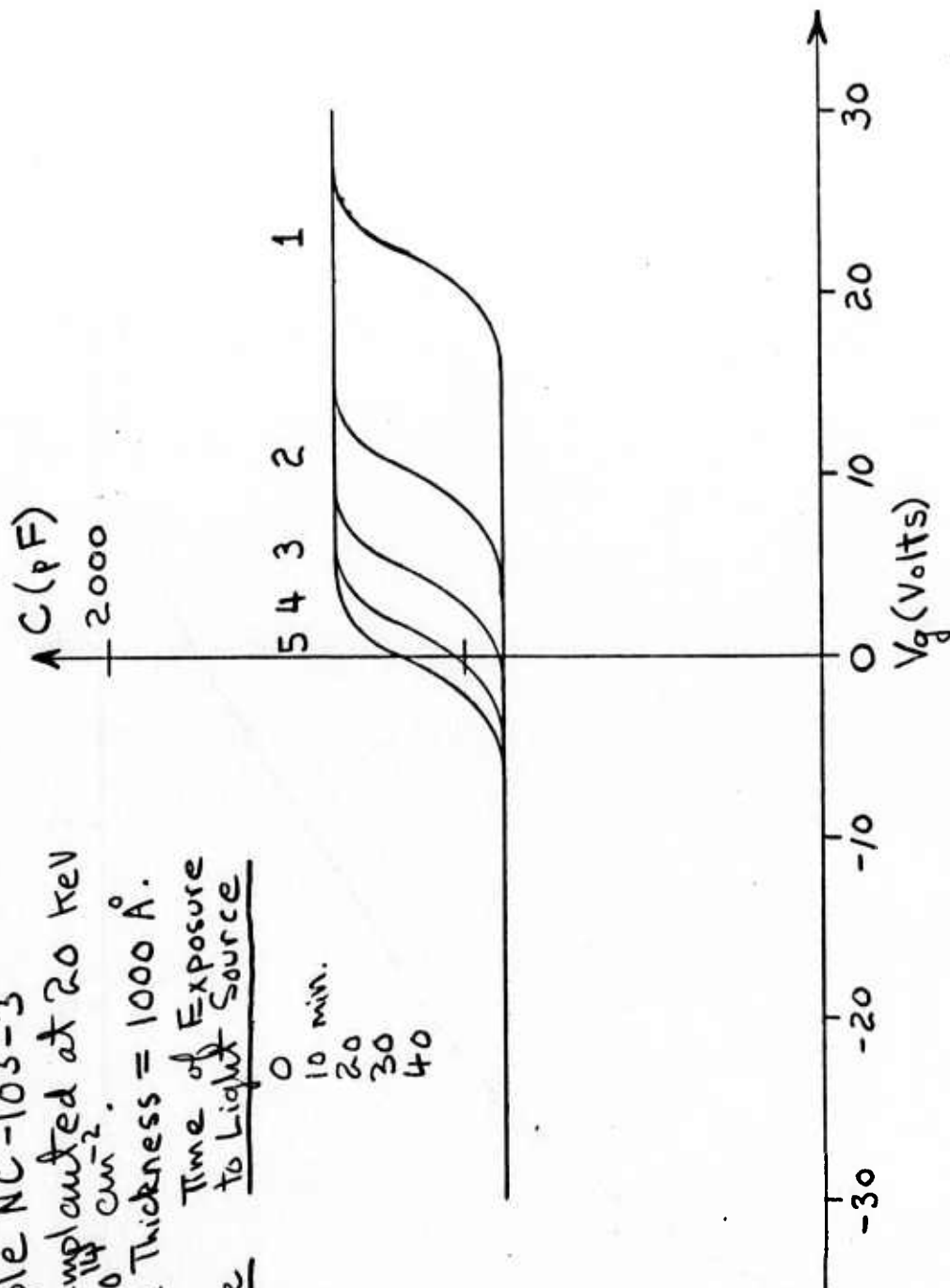
Fig. 7. Shift of the C-V Curve Due to Photodepopulation of Electron Traps.

subsequently implanted with aluminum ions to a dose of $10^{14}$ cm$^{-2}$.
The implantation energy was 20 keV, which produces a gaussian
distribution of aluminum atoms with the peak located approximately
at the middle of the insulating film and with a half width of
about 500Å. In Fig. 5 is shown a series of high-frequency
(1 MHz) C-V curves. Curve 1 is for the sample as received. The
flat-band voltage of -15 volts indicates an initial storage
of positive charge in the insulator equivalent to 3 x $10^{12}$
charges/cm$^2$ if the charge is located at the silicon-insulator
interface, and double this amount if the center of gravity of
the charge is located at the middle of the insulator. The
presence of deep electron traps in the insulator is shown by
Curves 2 through 7. These curves were produced in succession.
For each, the gate voltage was held at a constant positive
value and electrons were photoinjected from the silicon into
the insulator where they were deeply trapped. It will be seen
that the flat-band voltage of the MOS structure is very nearly
equal to the voltage at which the gate was held during the
photoinjection of electrons. Presumably the trapping of
electrons proceeds until the negative charge in the insulator
is sufficient to reduce the electric field at the silicon-
insulator interface to zero, thus bringing to a halt the
injection of further electrons. Furthermore, the electron
traps do not saturate with gate voltages of up to 35 volts.
This puts a lower limit on the number of traps: 1.5 x $10^{13}$ cm$^{-3}$
if the center of gravity of the charge is approximately at the
middle of the insulator. Figure 6 shows the transient current
that flowed in the trap-charging process that took the C-V
characteristics of the structure from Curve 1 to Curve 2 in
Fig. 5. Figure 7 shows the recovery (approximately exponential
in time) of the flat-band voltage of the sample when it is
irradiated with light from a xenon source with the field
plate of the sample biased negatively. Further experiments are
underway to determine more accurately the density of the traps

and to measure their capture cross sections and depth in the
forbidden gap. The results obtained to-date show the effective-
ness of the charge-discharge techniques for obtaining valuable
information on the electronic behavior of thin oxide films.
A brief summary of these results is being prepared for publi-
cation.

5. Electron-Beam Probe Studies of the Films (C. T. Shih
collaborating)

In this set of experiments, the problem of creating
a suitable, equivalently ohmic contact to the insulator is
dealt with by using a beam of electrons to create a reservoir
of electrons just under the surface of the insulator. A
front electrode, of very thin metal and comparatively transparent
to the electron beam, is used to impress voltage across the
sample. The energy of the electron beam can be adjusted in the
range of 1-5 kV.

The operation of the experiment can be visualized with
the aid of the upper band diagram shown in Fig. 8. The incident
high-energy electrons, after penetration of the thin field plate,
generate hole-electron pairs in the insulator up to their depth
of penetration R. (Also produced will be X-rays which can
penetrate the entire sample.) In $SiO_2$ the holes have a very
small mobility and are trapped and ultimately recombined with
electrons near their point of formation. In the vicinity of
the cathode, the density of electrons exceeds the density of
holes because of the electrons injected into the insulator
by the primary (incident) beam directly as well as by a
secondary current generated by the primary beam in the gate by
collisional excitation. The resulting negative space charge
creates a maximum in electron potential energy as shown in the
diagram. (This causes the effective sample voltage to be
larger than the applied voltage, $V_s$, and also causes the effective
sample length to be smaller than the actual length, as is
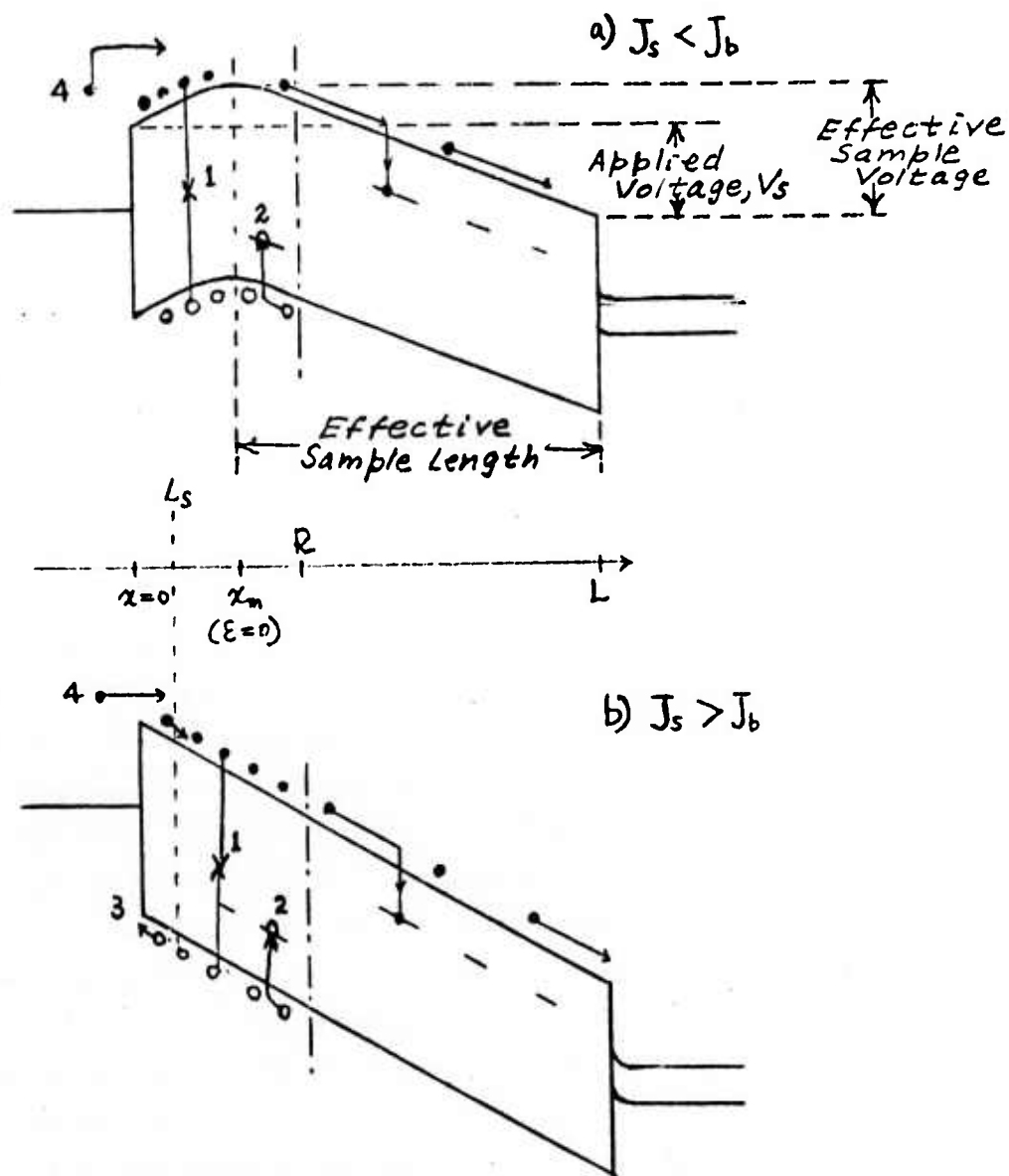indicated in the diagram. This effect must be taken into account

Fig. 8. High-field Separation of Electron-hole pairs

in the analysis of the data). In SiO$_2$ electrons are generally
not strongly trapped and therefore application of the voltage
across the sample results in their transport through the
insulator to the substrate, which serves as the anode. Figure 9
shows the sample current as a function of sample voltage for
Sample HH74, which consisted of 4000Å of SiO$_2$ thermally grown
on a substrate of n-Si. Here the beam voltage was 1.6 kV and
the beam current was 1.0 x 10$^{-7}$ amp. It can be seen that for
sample currents considerably smaller than the beam current,
the sample current follows approximately a sqaure law.  This
is followed by a steeply rising section beyond which the
current gain exceeds unity, that is, the sample current
exceeds the beam current. A possible explanation for this
effect is indicated by the lower band diagram of Fig. 8.  Here
the voltage applied to the sample has overcome the effect of
the negative space charge in the region of the cathode, and the
holes that have been created less than one Schubweg from the
contact (0 < x < L$_s$ in Fig. 8) are swept out and augment the
sample current. Inasmuch as one high-energy electron from the
beam will create many hole-electron pairs in the insulator,
the sample current can exceed the beam current if holes are able
to leave via the contact instead of recombining within the
insulator.  If this explanation for the current gains exceeding
unity were the only possible one it would be of considerable
importance, since it would directly establish hole motion in
the oxide and provide detailed quantitative information about
it.  Actually, it is highly likely  that some of the current
gain has its origin in the metal gate as already mentioned
above.  The thickness of metallization employed to-date is such
that a substantial fraction, up to one-half, of the incident
beam energy is lost in the metal gate producing a large number
of hot electrons in the gate. Some of the latter will escape
into the oxide providing a secondary contribution to the total
electron current delivered to the oxide.  In order to derive
any conclusions about hole motion in the oxide it is necessary
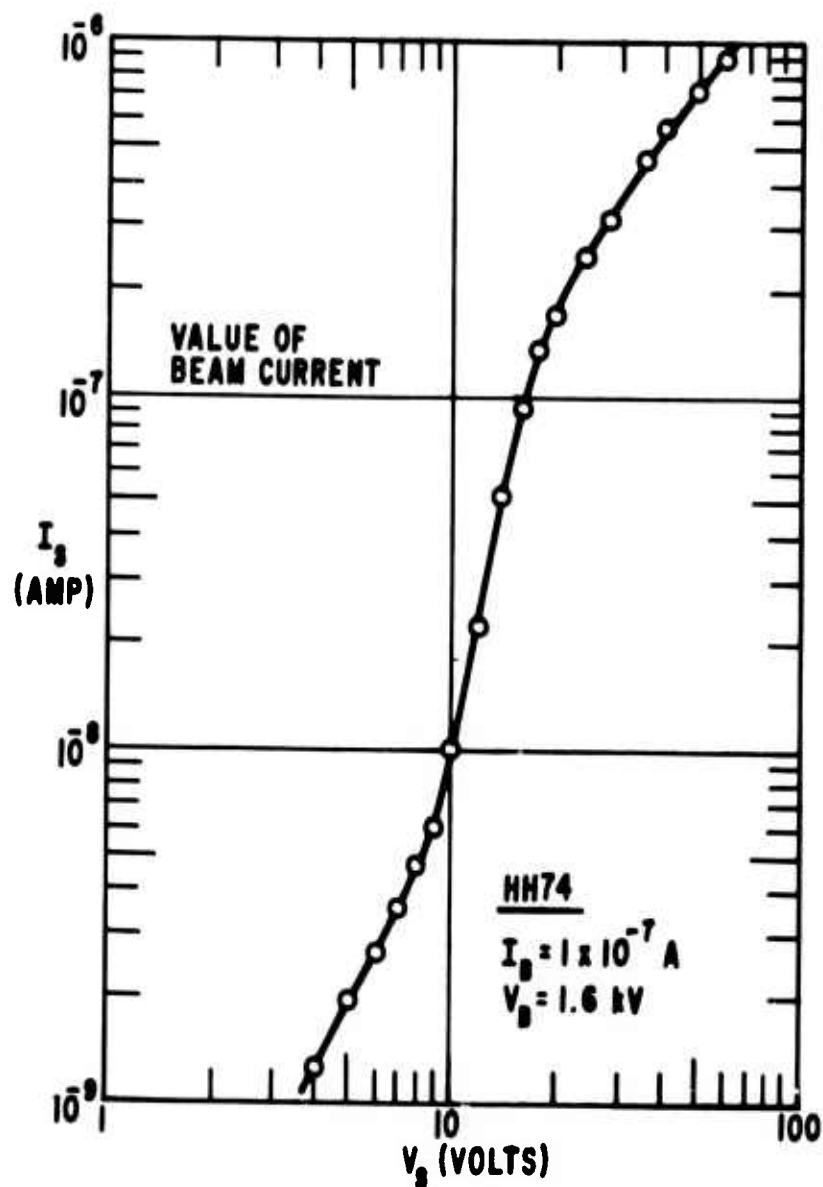to eliminate or separate out the secondary-current contribution

FIG. 9 SAMPLE CURRENT $I_s$ vs SAMPLE VOLTAGE $V_s$ FOR
FIXED INCIDENT BEAM PARAMETERS

of the gate. Towards this end we plan to prepare a series of samples with ultra-thin metallizations, down to 100Å thickness.

Further important results are shown in Figs. 10 and 11. Figure 10 shows the dependence of the sample current on the beam current in the square-law regime of $I_s$ vs. $V_s$, and indicates that the sample current is approximately linearly dependent on the magnitude of the beam current (the lack of parallelism among the curves is attributable to the difference between the applied and effective sample voltages; see Fig. 8). The results shown in Fig. 11 indicate that the sample current is only weakly dependent on the temperature. Finally, analysis of the data in the square-law regime shows that the sample current is considerably smaller than the magnitude predicted by the Mott-Gurney relationship for single-carrier space-charge-limited currents in a trap-free insulator: $J = (9/8)\epsilon\mu V_s^2/L^3$, where $\epsilon$ is the absolute dielectric constant of the insulator and $\mu$ is the mobility of the charge carrier. Taken together, these data lend themselves to the following interpretation: The current is predominantly single-carrier and space-charge-limited, but a large fraction of the electrons are trapped and the appropriate expression for the current is, consequently,[17]

$$J = \frac{9}{8} \theta\epsilon\mu \frac{V_s^2}{L^3} \qquad , \qquad (3)$$

where $\theta$ is the ratio of free to trapped electrons, and $\theta \ll 1$. The comparative independence of current on temperature and the nearly linear dependence on magnitude of beam current indicates that the emission of charge carriers from traps is not thermally produced but is instead the result of a photon flux which is generated over the range of the incident primary beam, that is, in the gate and in the first few hundred Angstroms of the oxide near the gate.

In order to investigate the foregoing effects further, we are currently arranging the equipment for illumination of the sample with light from a high-intensity monochromator.
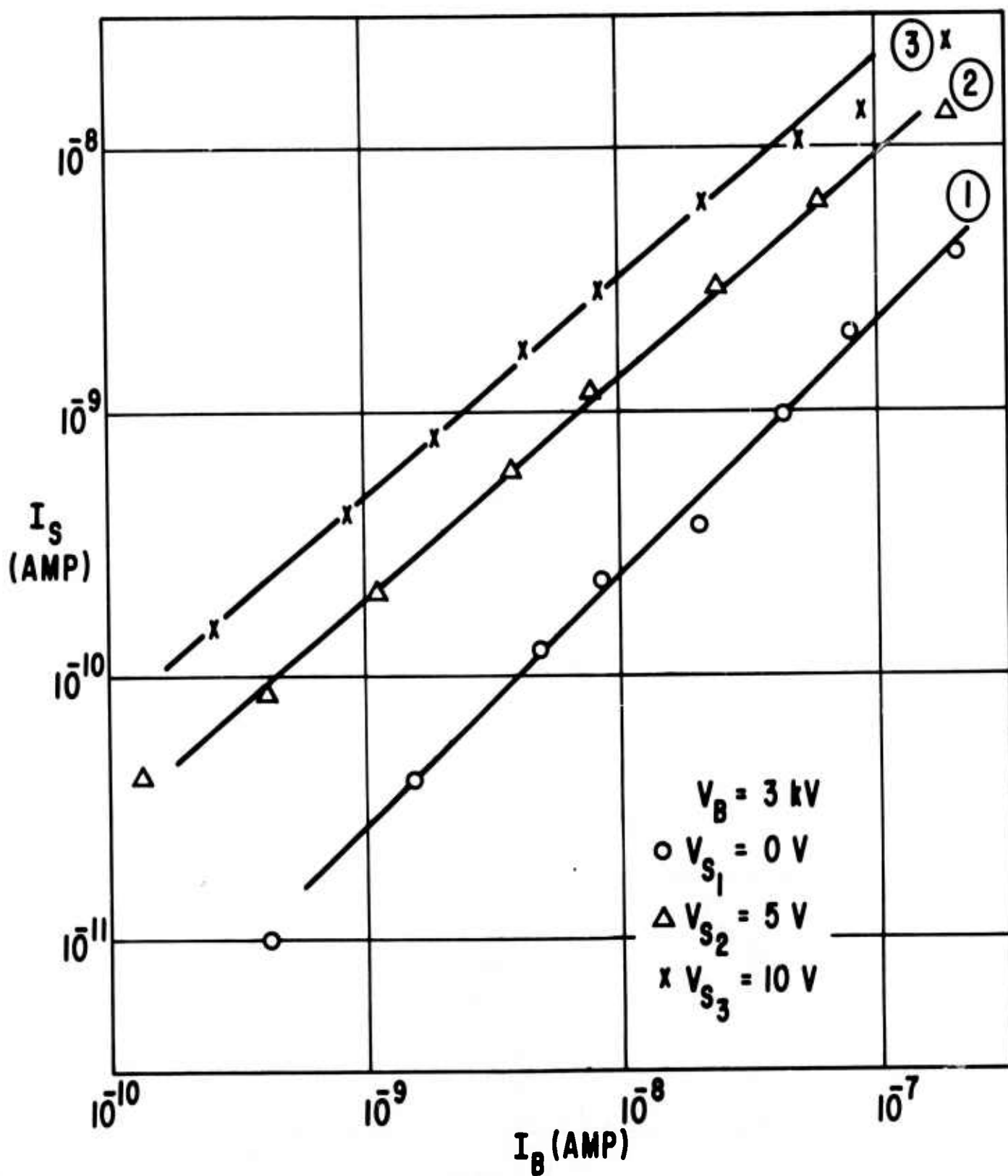
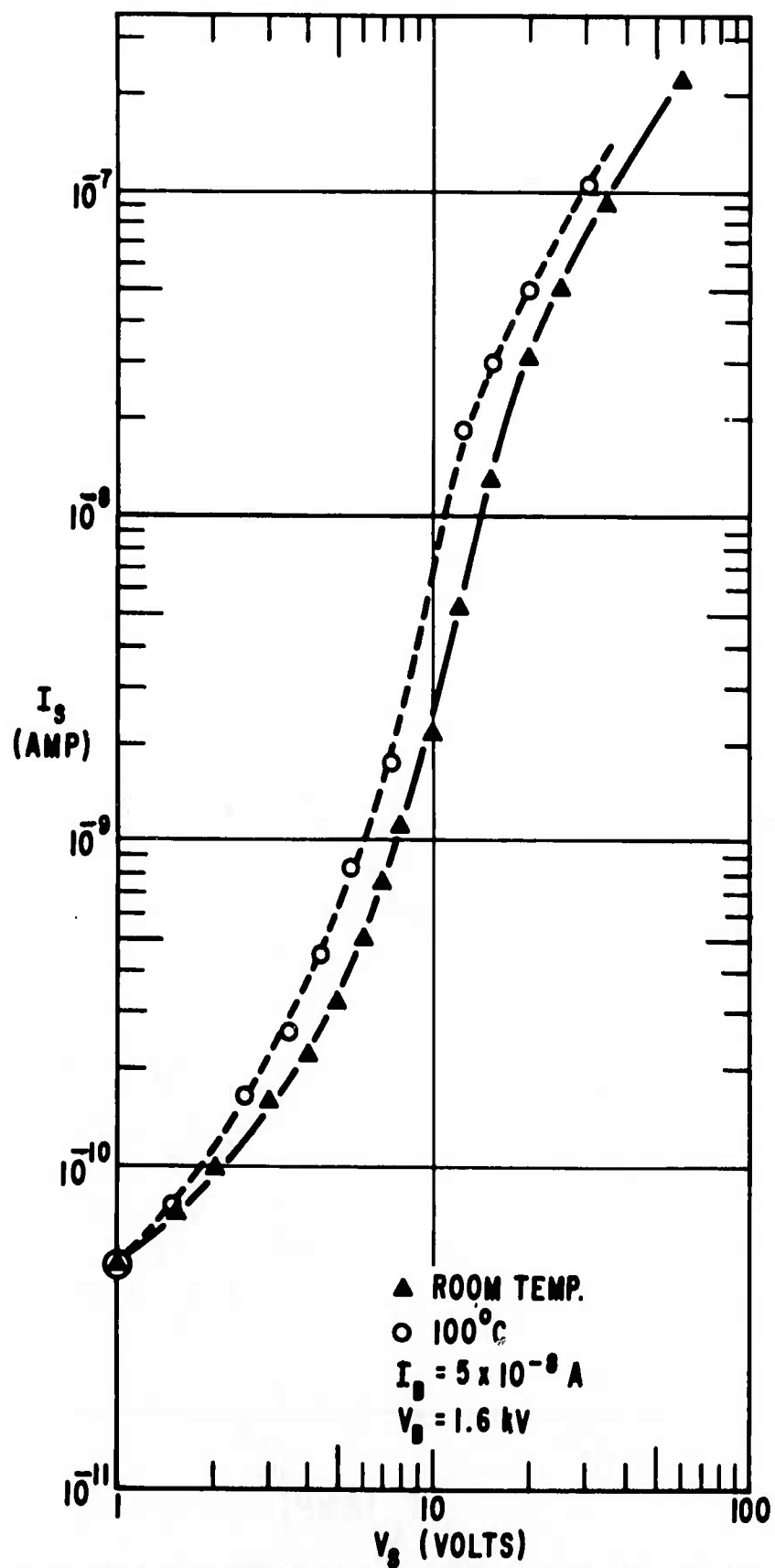FIG. 10 SAMPLE CURRENT $I_S$ vs BEAM CURRENT AT FIXED BEAM AND SAMPLE VOLTAGES

FIG. II SAMPLE CURRENT $I_s$ vs SAMPLE VOLTAGE $V_s$ AT
TWO TEMPERATURES (INCIDENT BEAM PARAMETERS
FIXED)

This will permit us to study the effect on θ of the intensity and photon energy of the light and will provide a method of investigating the density of traps and their distribution in energy.

6. <u>Secondary-Electron Spectrometry</u> (D. Guterman collaborating)
   A. <u>Background Discussion</u>

In the past few years secondary electron spectroscopy has become a powerful tool for the analysis of solid surfaces. Two separate analytical techniques have been developed for this purpose using a spectroscopy of secondary electrons. The first is Auger electron spectroscopy (AES) designed to determine the elemental composition of a surface. The second is electron spectroscopy for chemical analysis (ESCA) which is designed to determine the chemical environment in which the atomic constituents of a surface reside. The construction of a secondary electron spectrometer with both high resolution and high sensitivity will allow an extension of AES to perform analysis of the chemical environment of the atoms on a solid surface and to probe the band structure near the surface, much as is done in external photoemission studies. In AES the sample is bombarded with an electron beam of a few thousand electron volts energy and the distribution of secondary electrons is measured. The energies at which peaks occur in the secondary emission spectra correspond to energy level differences in the emitting atom. Therefore the elemental species may be identified through a measurement of the peak energies. The amplitude of these peaks above the background level is a measure of the relative abundance of the various atomic species found on the surface. This technique has a sensitivity in the range of $10^{-2}$ to better than $10^{-3}$ monolayers depending on the shot noise in the particular detector system, the particular elements being measured, and the elemental composition of the background matrix. In addition to this powerful capability of identifying atomic species on a surface there is a great deal of information stored in the fine structure of the Auger peaks which has yet to

be fully explored and utilized. The energy of an Auger peak is determined by the energy level differences within the atom and, particularly where valence orbitals are involved, these differences are altered by the chemical bonding configuration of an atom. Therefore small shifts in energy of a particular peak can be related to the chemical bonding conditions of the atom being probed. The fine structure on the low energy side of the Auger peaks and the primary electron beam can be associated with plasmon and phonon excitations. A spectrometer with sufficient energy resolution would therefore also have the capability of measuring the plasmon and phonon spectra near the surface.

The shape of the Auger peaks is determined in large part by the density of states in the valence band near the surface. This is due to the fact that the probability of an Auger electron of energy $E_1$ to be emitted in a WXY transition (W denotes the band where the initial vacancy is formed by the incident electron beam, X the band of origin for the electron decaying to fill the W band vacancy, and Y the band of origin for the electron ejected to relax the energy difference between bands W and X) is proportional to the density of filled states in the X and Y bands. Experimentally this means that, knowing the distribution of electrons in an Auger peak, one can determine the density of filled states in the bands participating in the emission process. For transitions of the type KVV or LVV where the valence bund is involved we may determine the electron density of states in the valence band. The analysis is simplified in these two cases by the fact that the K and L bands are usually very narrow and therefore may be considered mono-energetic. The benefits to be derived from an appropriately designed secondary electron spectrometer and a highly focused electron beam for exciting the secondaries may be summarized as follows:

1. Elemental analysis of a surface may be carried out with a sensitivity of better than $10^{-3}$ monolayers under optimum conditions.

2. The chemical bonding state of the elements on the surface of a solid may be determined with essentially the same sensitivity as the elemental analysis.

3. A measurement of the density of occupied states near the surface, for bands participating in the Auger emission, may be carried out.

4. High spatial resolution for the analytical capabilities in 1-3 above may be achieved. The resolution is limited only by the size of the incident electron beam.

B. Secondary-Electron Spectrometer

In order to obtain all of these benefits in an electron spectrometer we have designed a system which has the maximum possible collection efficiency and throughput for the secondary electrons and the lowest possible shot noise. In addition, the spectrometer was designed with a high energy resolution so that the measurement of fine structure in the Auger peaks as well as an accurate measurement of the peak positions would be possible. The system resulting from these design considerations is shown in Fig. 12. High collection efficiency is accomplished since the spectrometer entrance subtends an angle of 96 degrees with respect to the sample. The throughput is limited only by the transparency of the first two grids and is maintained at a high level by using a wire mesh for the grids with an optical transparency of 90 per cent. The functions of individual components of the spectrometer are as follows:

1. Grid one is grounded during normal operation to provide a field free region around the sample and thereby prevent errors in the Auger energies caused by fields between the sample and the detector entrance. To increase the collection of secondary electrons, when high resolution is not necessary, grid one may be biased positive with respect to the sample.

2. Grid two is biased negatively with respect to the sample by a ramp power supply. This provides a low energy cut-off filtering of the secondary electrons. The wire mesh used to fabricate this grid is very fine, resulting in a theoretical
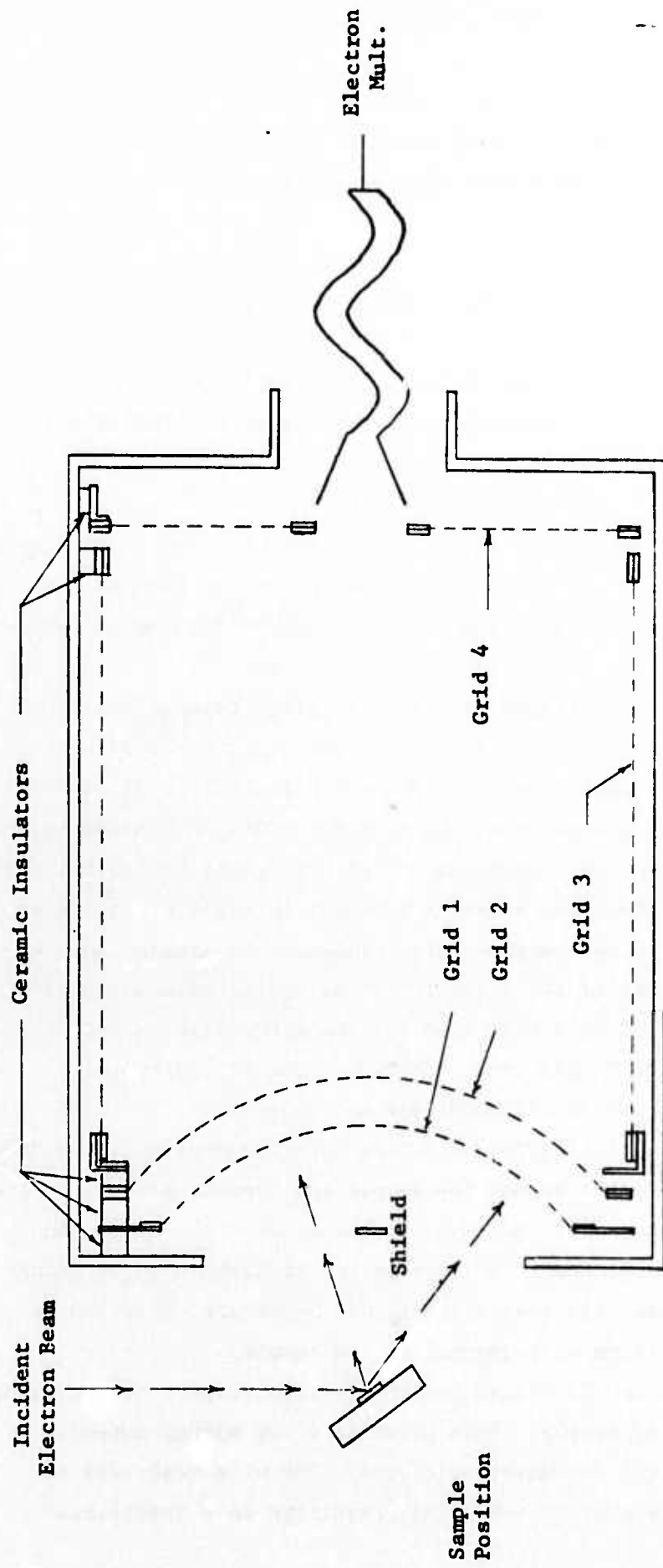
Fig. 12  Diagram of the Secondary Electron Spectrometer

resolution of 0.01 percent of the energy of the secondaries.

3. Grid three is held at a potential slightly more negative than that of grid two. This has two beneficial effects; the first is the focusing of low energy electrons passing through grid two toward the aperture in grid four. The second is to prevent secondaries, generated on the walls of the detector body by high energy electrons reflected from the sample, from entering the spectrometer, thereby keeping the shot noise to a minimum.

4. Grid four is held exactly at the potential of grid two. This provides a low field region where electrons passing through the second grid are focused, by the collector potential and the potential on grid three, toward the collector. Electrons which pass through the second grid with high energy are not deflected to the collector by this low-strength focusing field and therefore the necessary high cut-off filter is established. This minimizes the current through the detector and thereby the shot noise of the spectrometer.

5. The shield between the sample and grid one prevents high-energy, reflected electrons from reaching the collector and thereby contributing to the shot noise of the system.

6. The collector is a high gain, low noise, continuous, dynode electron multiplier. The potential at the front of this detector is positive with respect to grid two to draw low energy electrons into the multiplier and it may be varied to provide a real-time control of the resolution-sensitivity trade-off. The potential drop across the multiplier is controlled separately to ensure the highest possible gain which does not saturate the multiplier under various signal strength conditions.

7. The outer body of the detector provides structural strength to the grid structure, prevents electrons scattered in the vacuum chamber from entering the spectrometer, and provides the magnetic shielding essential to the efficient operation of the spectrometer.

The response of this system has been modeled on the IBM 360 model 91 computer and the design has been optimized for

resolution and collection efficiency. The results of this
modeling indicate that the resolution under optimum conditions
may be as high as 0.025 electron volts. In practice the
resolution is determined by the second grid and the shot noise
which is limited by the high energy cut-off. Figure 13 shows a
plot of the trajectory of the electrons passing through the
spectrometer and it illustrates the high energy cut-off properties
of the spectrometer. Figure 14 shows the calculated efficiency
of the spectrometer as functions of the potential of the third
grid and the front of the electron multiplier with respect to
the grid-two potential. It illustrates another valuable feature
of this electron spectrometer, namely that the resolution-
sensitivity trade-off may be controlled by altering the potentials
in the spectrometer without any requirement for alteration of
the physical arrangement as is necessary with the conventional
cylindrical mirror system.

C. Preliminary Results

The spectrometer and an appropriate power supply have
been completed. Preliminary spectra have been taken with this
spectrometer and as a standard they have been compared with the
spectra from a commercial (Varian Associates) LEED-Auger device.
At the present time the new system is exhibiting a signal-to-
noise ratio more than fifty times better than the commercial
device under identical conditions of excitation. Figures 15 and
16 show typical spectra taken from the new spectrometer and the
LEED-Auger device using the same electron gun in the same
vacuum chamber. Figure 15 shows a spectrum taken with the
LEED-Auger device with 250 microamps incident beam current
and a modulation (necessary for differentiation of the signal
with a lock-in amplifier) of 10 volts peak-to-peak. These
parameters represented the minimum for obtaining a usable
spectrum. Figure 16 shows a spectrum taken with the new detector
with 30 microamps incident beam current and a modulation of
5 volts peak-to-peak. These changes in the parameters reduced
the signal by more than a factor of six and the signal-to-
noise ratio has improved approximately by a factor of eight.

Electron Multiplier

Grid 2
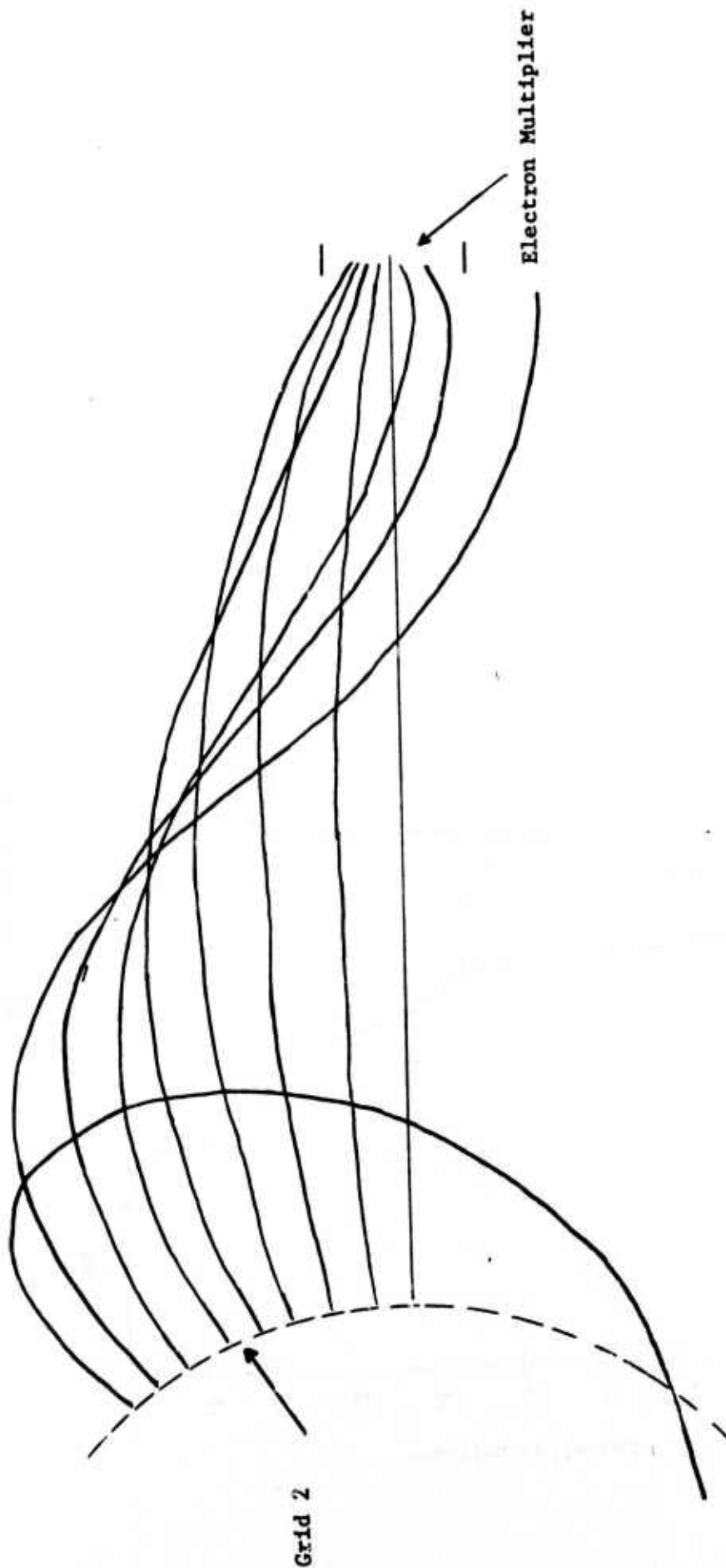
Figure 13

Computer calculated electron trajectories
through the spectrometer illustrating both
low energy and high energy cut-off trajectories

Electron Energy (eV)
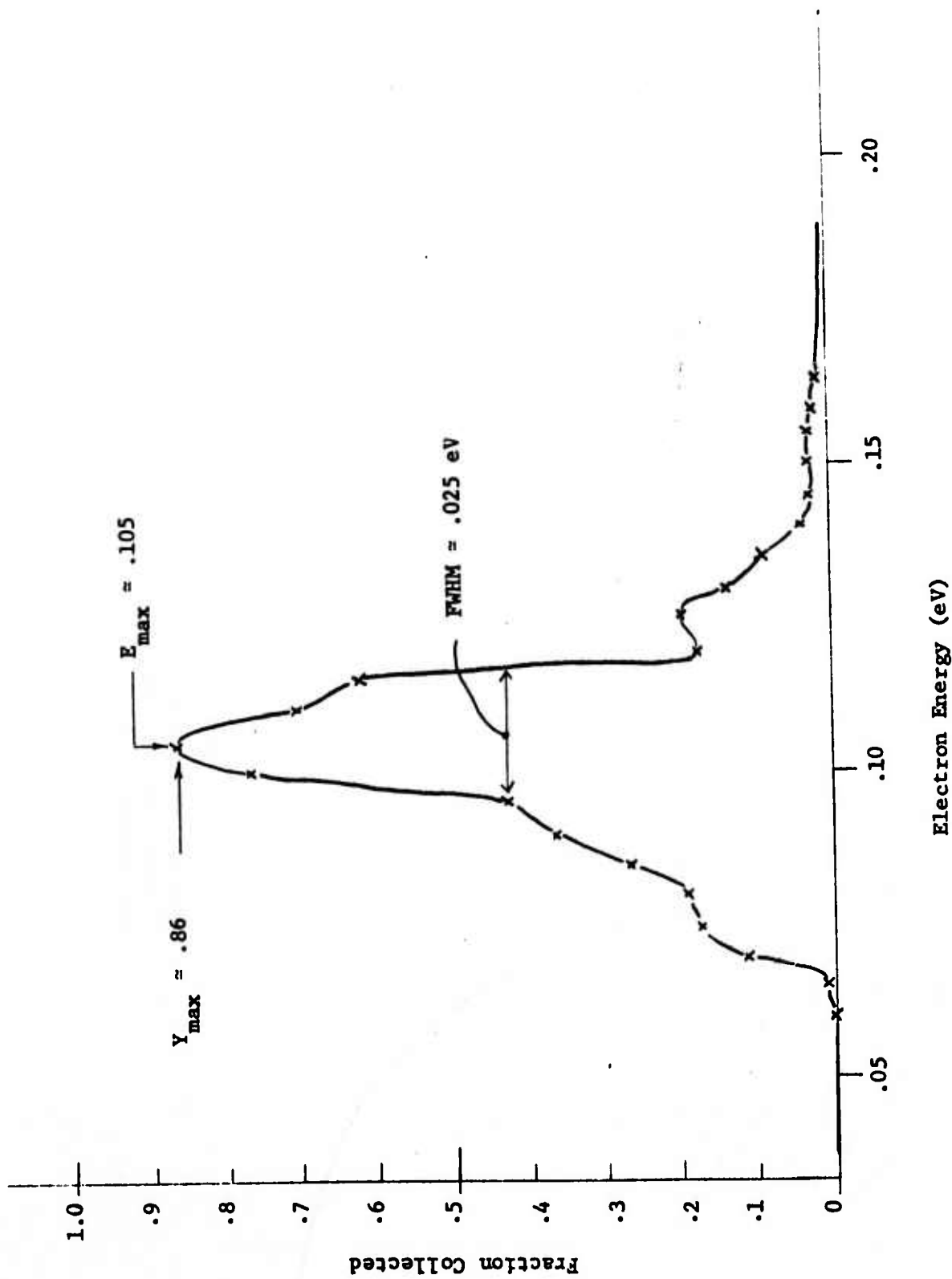
Fig. 14

Collection efficiency for 3rd grid at 0.1 volts and 50 volts
collecting voltage at the front of the electron multiplier
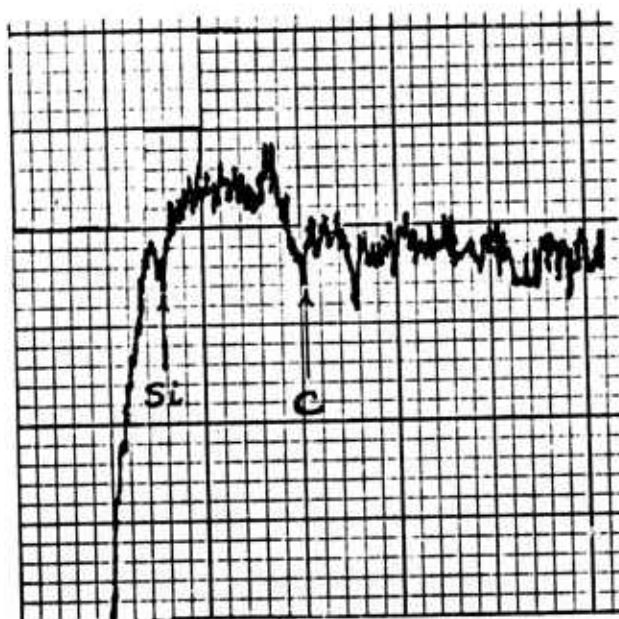
Figure 15

Auger spectrum of a Si surface taken with a commercial LEED-Auger
device.   Incident current 250 microamps, 10 volts peak to peak
modulation.
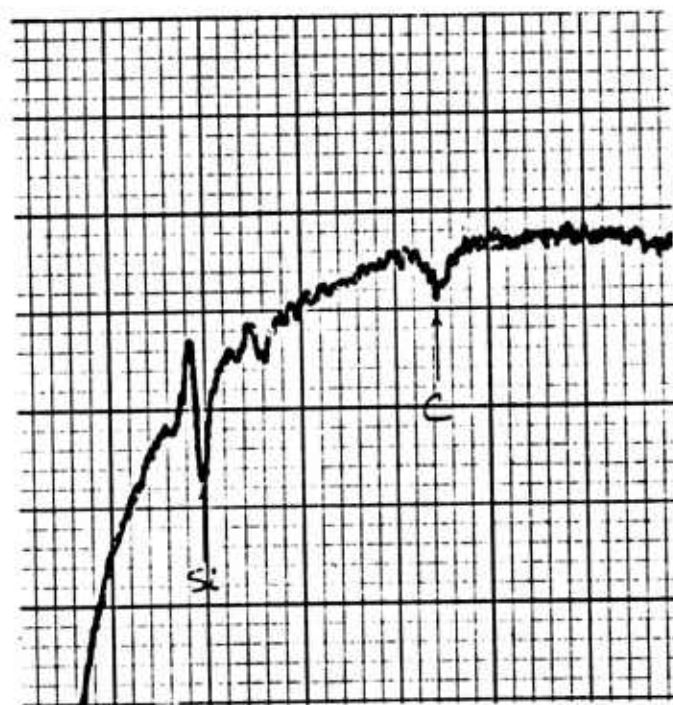
**Figure 16**

Auger spectrum of a Si surface taken with the new spectrometer.
Incident current 80 microampsl 5 volts peak to peak modulation.

This system will be applied to the study of the elemental distribution, chemical composition, and surface band structure of thin insulating films.

The spatial resolution of the electron spectrometer described above is limited by the size of the exciting electron beam. Therefore, in order to attain the best possible spatial resolution, this system is to be mounted on the specimen chamber of a scanning electron microscope (SEM). Since this technique is essentially a surface analysis, due to the short elastic range of the secondary electrons, it is necessary that the experimental chamber provide an environment in which the nature of the specimen surfaces can be maintained constant for the duration of a measurement. Commercially available SEM equipment does not have the required vacuum capability and therefore such a system has been built at Princeton University. At present, a system capable of $10^{-9}$ torr in the specimen chamber has been completed and a modification is presently underway to provide this system with an air lock so that the SEM can be maintained at constant high vacuum, except for infrequent maintenance requirements. The specimen chamber is equipped with X-ray fluorescence spectroscopy, induced current probes, transmitted electron probes, voltage contrast capability, as well as the traditional detector for topographic imaging. Measurements on silicon dioxide have been performed in the SEM using the Auger spectrometer but, as yet, the system has not been perfected to allow the observation of band structure in the specimen. An example of these preliminary spectra, Fig. 17, shows that the surface is composed of silicon, oxygen and carbon. The silicon-to-oxygen ratio was found to differ slightly from one part of the sample to the next although at the present time we have no quantitative measure of this observation. The quality of the analytical information available should be greatly improved by the completion of the system within the next few months.

This SEM system has been used to study pyrolytic $Al_2O_3$ thin films (900 to 1400Å thickness) grown on p-type (100)
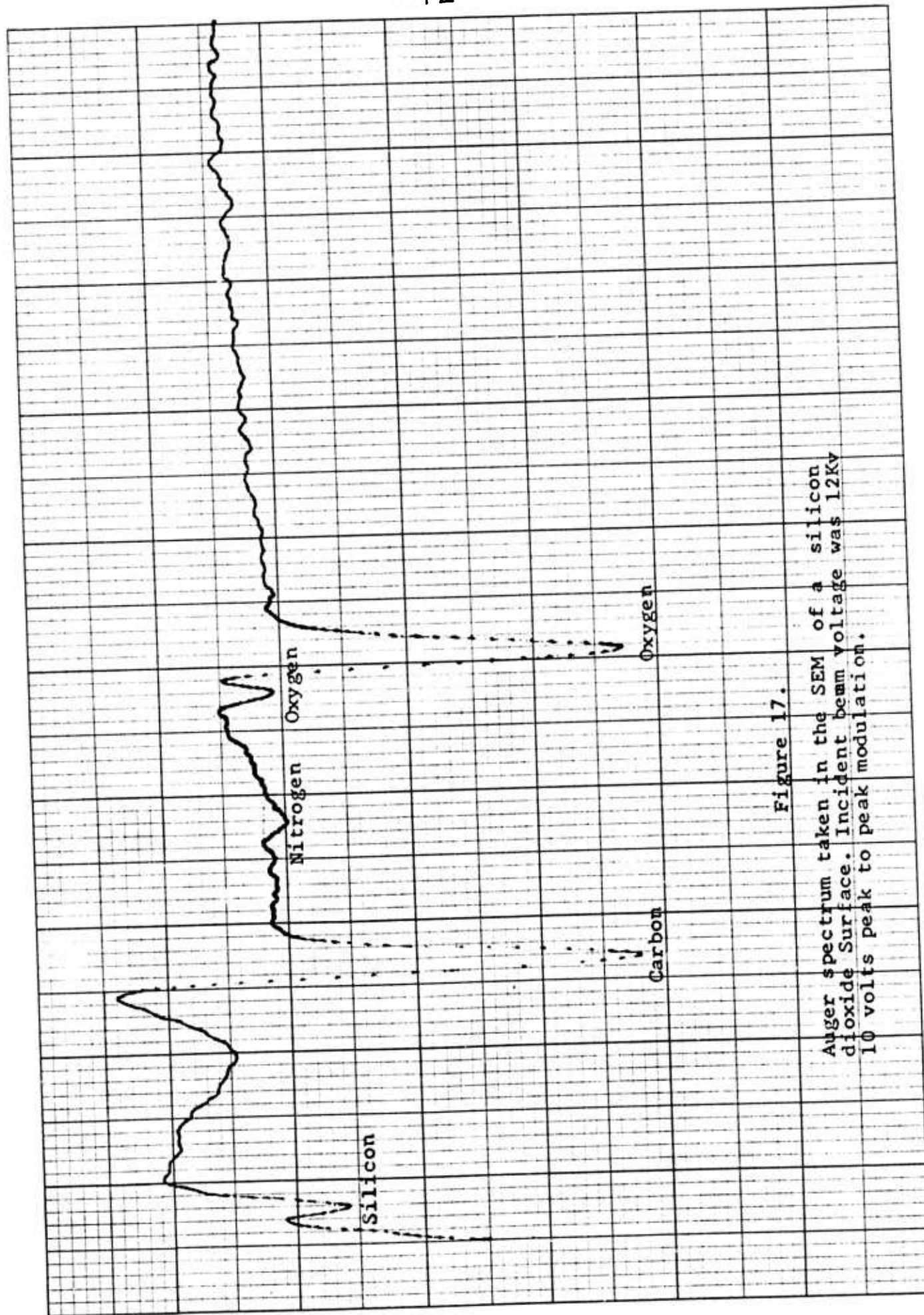
Figure 17.

Auger spectrum taken in the SEM of a silicon dioxide Surface. Incident beam voltage was 12Kv 10 volts peak to peak modulation.

silicon substrates. Utilizing the standard secondary electron topographic image, these samples were found to be smooth and flat out to the limits of detectability over most of their surface. This places an upper bound on the topographic variations on the surface of the order of 100Å. There were several large defects found distributed over the surface of each of the pyrolytic $Al_2O_3$ samples which were of two distinct types. The first was a round hole with pointed crystallites rising from the center and the second was a large (up to one micron in diameter), irregular shaped piece of crystalline material. There was no spatial correlation between these defects or any other measureable parameter on the samples. The identification of the material centered in the round holes shown in Fig. 18 was accomplished by X-ray fluorescence. The material is predominantly silicon and it is likely some artifact of the film fabrication process. Similarly, the irregular crystalline material found on the same samples was determined to be aluminum, also interpreted as an artifact of the growth process. Additional $Al_2O_3$ samples are being prepared under different conditions. Study of these new samples should allow us to determine the origin of the defects.

### D. Optical Instrumentation

In conjunction with the electron spectrometry studies of thin films, optical studies of both internal and external photoemission will be carried out. A high energy light source has been set up and is presently operational. It is composed of a high intensity vacuum ultra-violet discharge lamp of the Hinteregger type, a Specs 1500 vacuum ultraviolet high intensity monochromator (6.8 optics), and a LiF window and adapter to various sample vacuum systems with a half silvered mirror in the light path for calibration. This light source and monochromator combination provides in excess of 1000 times the intensity previously available at Princeton for the wavelengths useful in this study. The light source monochromator system have been calibrated in wavelength, intensity and long term stability and
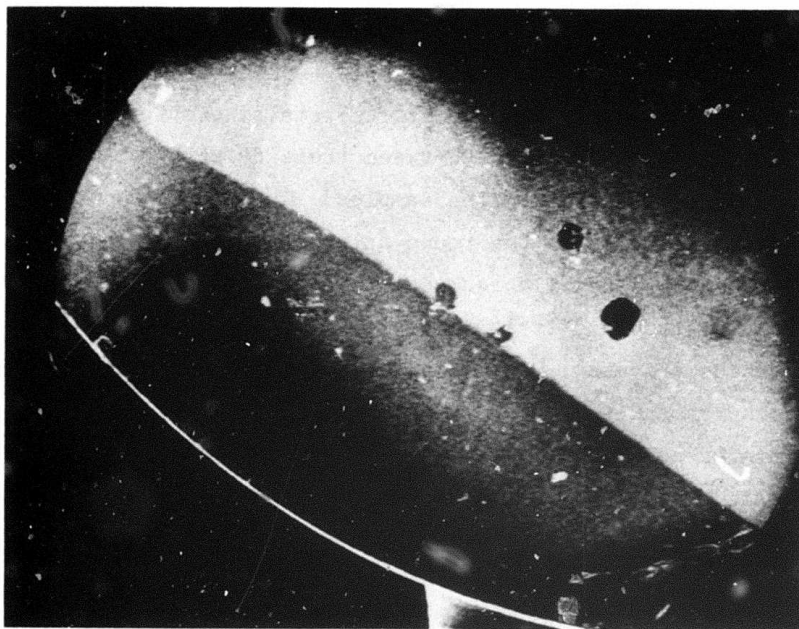
Figure 18

SEM micrograph of an $Al_2O_3$ film on a silicon substrate showing holes in the $Al_2O_3$ layer in which silicon crystals are growing.

the output curve attached in Fig. 18b shows high intensity out
to 1400 angstrom units. The capability of this system will be
applied to the characterization of thin films of $Al_2O_3$ , $SiO_2$ ,
and $Si_3N_4$ in the coming months.

7. Monte Carlo Studies of Hot-Electron Behavior in Insulating
   Films at High Fields (S. Baidyaroy and B. Zee collaborating)

   A. Background Discussion

   In order to obtain an understanding of the physical
mechanisms underlying electrical breakdown of thin insulating
films at high applied fields it is necessary to obtain a reasonable
description of hot-electron behavior at the high fields. This
is an extremely difficult theoretical problem which, in the
context of the thin-insulating-film problem, is completely
beyond the reach of analysis. We have therefore sought
efficient means of utilizing the high-speed digital computer
to study the problem. The costs of computation have provided
a strong stimulus to find truly simple, namely one-dimensional,
models to simulate the main features of the full three-
dimensional problem.

   The problem we have addressed ourselves to is as follows:
An electron with a specified initial energy is injected into the
film in a randomly chosen direction at one end of the film
taken at $z = 0$. The electron is driven by the field toward the
other end of the film, at $z = t$, where t is the film thickness.
In moving through the film the electron picks up energy from
the applied field, but it is also randomly scattered by
collisions with phonons (quantized 'lattice' vibrations in the
film). It is assumed that, at the high fields of interest in
the breakdown problem, namely in the range $10^6$ to $10^7$ V/cm,
the only significant scattering events are optical-phonon
emissions, the fixed energy $\varepsilon_{ph}$ being lost in each such collision.
(An electron with energy $E < \varepsilon_{ph}$ is not permitted to make an
energy-loss collision). The field-driven electron is followed,
as a classical particle, in its randomly-colliding course through
the film, using the Monte Carlo (random number) method[18] of
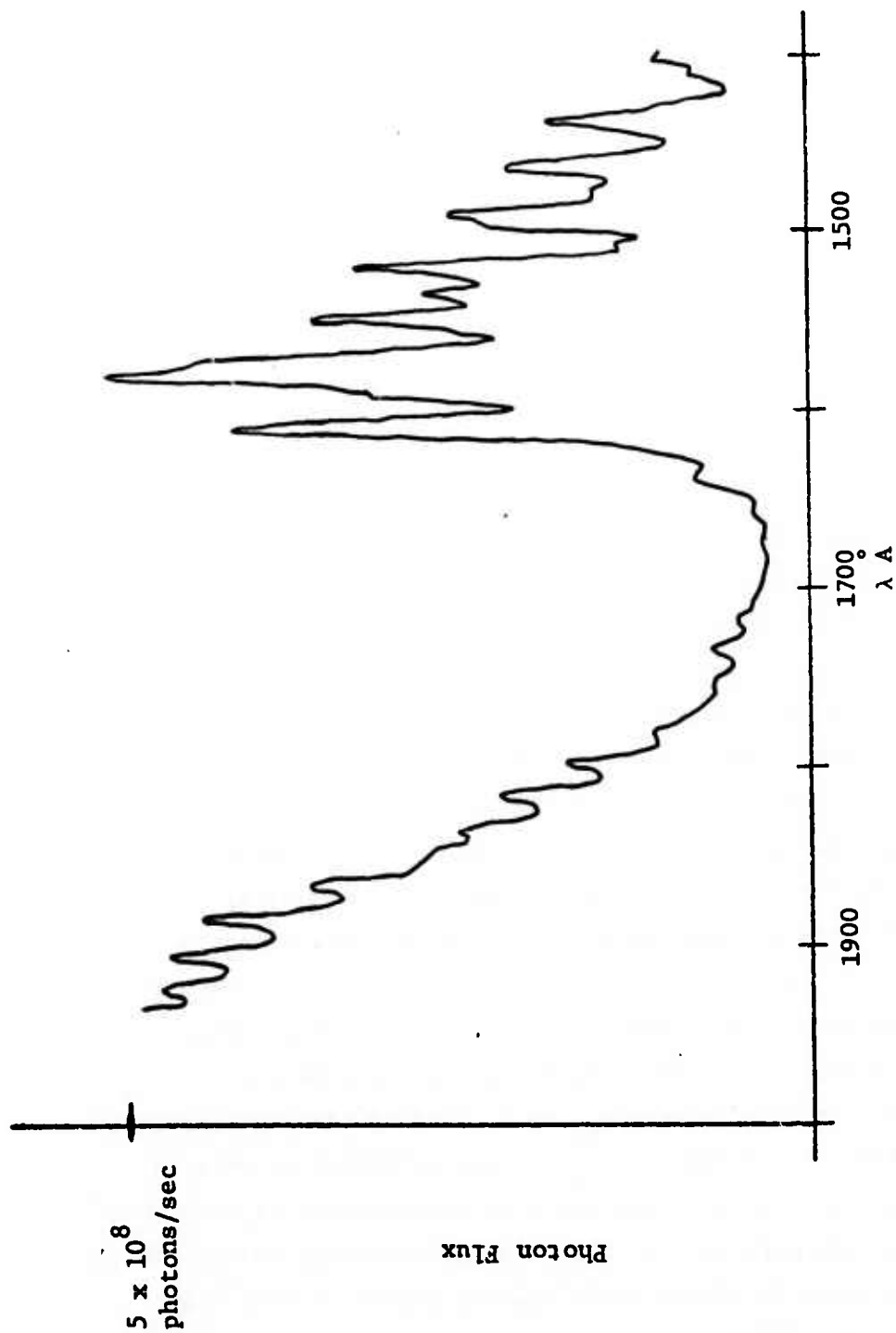
Fig. 18b

Output spectra of the specs 1500 vacuum UV monochromator

dealing with the probabilistic features of its trajectory history. At the exiting end of the film, at z = t, the energy and angle of emergence are noted (as well as the lateral distance traversed by the electron). A second electron is then injected and followed until emergence at the plane z = t, then a third electron and so on, up to 200 or more electrons. In this way a histogram of emerging electron energies is complied (likewise, one for emerging angles). These particular histograms are of special interest because experimental determination of emergent electron energies is feasible - as compared to the extraordinary difficulties of experimental determination of hot-electron distributions _inside_ a medium. A considerable number of situations have been studied on the computer in this way, mostly constant-mean-free-path (independent of energy) problems with different scattering laws, corresponding to isotropic scattering, dominant (polar optical phonon) forward scattering. In order to simplify the computer calculations, in particular to avoid numerically solving an integral equation over and over again, we have utilized the ingenious self-scattering method of Rees,[19] explained below. Further, we have systematically explored one-dimensional simulations of the full three-dimensional problems, and have shown that these simulations are extremely useful in that they reproduce the salient features of the latter. We have further shown that strong forward scattering, by itself, is insufficient to lead to instability of the hot-electron distribution, that is, to 'runaway' of the distribution. Finally, we have initiated the study of the practically important class of problems in which the mean-free-path is energy dependent. If the mean-free-path increases fast enough with energy we would expect runaway of the distribution, and we have shown that this is indeed so. Further, we have shown that the problem of distribution stability can be studied graphically using the already-obtained results of the far simpler constant-mean-free-path computations.

## B. Mathematical Formulation

The mean free path (mfp) $\lambda$ is defined such that the probability of scattering in the increment of path length ds is ds/$\lambda$. For constant mfp (independent of electron energy) this leads to the decay law: $n - n_o \exp(-s/\lambda)$ where n is the electron concentration (or number) after the distance s along the trajectory has been traversed and $n_o$ the corresponding concentration (or number) at $s = 0$. Defining P(s) as the probability that the electron has gone the distance s without scattering, we readily obtain the equation

$$\frac{dP}{P} = - \frac{ds}{\lambda} \qquad , \qquad (4)$$

which has the solution

$$P(s) = \exp\left(- \int_o^s \frac{ds}{\lambda}\right) \qquad , \qquad (5a)$$

which, for constant mfp becomes

$$P(s) = \exp\left(- \frac{s}{\lambda}\right) \qquad , \qquad (5b)$$

Defining $P_{sc}(s)$ as the probability density that the electron scatter in incremental path length ds after traversing path length s without scattering, we have

$$P_{sc}(s) = \frac{P(s)}{\lambda} = \frac{1}{\lambda} \exp\left(- \int_o^s \frac{ds}{\lambda}\right) \qquad , \qquad (6a)$$

which for constant mfp reduces to

$$P_{sc}(s) = \frac{1}{\lambda} \exp\left(- \frac{s}{\lambda}\right) \qquad , \qquad (6b)$$

Note that $P_{sc}(s)$ is properly normalized, that is, that $\int_{0}^{\infty} ds\, P_{sc}(s) = 1$. Also note that, for constant mfp, $\int_{0}^{\infty} s\, P_{sc}(s)\, ds = \lambda$. The correspondence with the random number variable $r'$ lying between 0 and 1 is

$$dr' = P_{sc}(s)\, ds \qquad , \qquad (7)$$

which integrates to

$$\int_{0}^{r'} dr = r' = \int_{0}^{s} P_{sc}(s')\, ds' \quad , \qquad (8)$$

Using a suitable computer routine to generate the random number $r'$, the corresponding trajectory length s between successive collisions is determined by solution of the integral equation (8). In the general case this integral equation will be analytically intractable and will have to be solved numerically (over and over again). A very important exception is the constant mfp problem, for which (8), using (6b), has the simple analytic solution

$$r' = 1 - \exp\left(-\frac{s}{\lambda}\right) \qquad , \qquad (9)$$

or, letting $1-r' = r$,

(constant mfp) $\qquad s = -\lambda \ln r \qquad , \qquad (10)$

where r is also a random variable in the interval 0 to 1. Thus, for the constant mfp problem s is given simply by (10), once the computer has generated r.

Without further simplification a formidable computer calculation still remains. Consider the relatively simple hot-electron problem of constant mfp and isotropic scattering. It is easy to see that, because of the assumed scattering isotropy, this problem can be studied as a two-dimensional problem, one dimension being along the field, i.e., along z, and the other transverse to

the field, along y. Now suppose that a collision has just taken
place, at time $t_i$ and at the co-ordinates $y = y_i$ and $z = z_i$, and
that we have determined the two velocity components, $v_{y,i}$ and $v_{z,i}$,
with which the electron emerges from the collision. The computer
now generates a random number r, and (10) then determines the
path length s to the next collision. It remains to determine the
electron co-ordinates, $y = y_f$ and $z = z_f$, at this collision, as
well as the electron energy $E_f$. In order to do this it is
necessary first to determine the time $t_f$ of the second collision.
This is given by solution of the integral equation

$$s = \int_{t_i}^{t_f} d\tau \sqrt{v_{y,i}^2 + (v_{z,i} + \frac{qF}{m} \tau)^2} \quad , \qquad (11)$$

with q the electronic charge, m the electronic mass, F the applied
field, and with s given by (10). In his earlier work, Martinelli[20]
solved this equation numerically, by the technique of successive
iteration. [Noting that the (indefinite) integral in (11) is
basically of the form $\int dT \sqrt{1 + T^2} = \frac{1}{2} T \sqrt{1 + T^2} + \frac{1}{2} \ln \{T + \sqrt{1 + T^2}\}$,
we see that the integral equation (11) can indeed be replaced by
an algebraic, transcendental equation. However, this must obviously
be solved by some method of successive approximation and consequently
there may not be any substantive saving in computer time over Martinelli's
direct, iterative solution of (11)]. Having now determined $t_f$, and
setting $t = t_f - t_i$, the electron co-ordinates and energy at the time
$t_f$ of the next collision are given respectively by

$$z_f - z_i = v_{z,i} t + \frac{F}{2m} t^2 \qquad , \qquad (12a)$$

$$y_f - y_i = v_{y,i} t \qquad , \qquad (12b)$$

and

$$E_f = \frac{1}{2} m [v_{y,i}^2 + (v_{z,i} + \frac{qF}{m} t)^2] \qquad . \qquad (13)$$

The electron loses the energy $\varepsilon_{ph}$ through single phonon emission at each collision, and then starts on a new trajectory in a randomly chosen direction, determined by a computer-generated random number in the manner discussed below. The cycle is repeated until the electron emerges from the film at $z = t$. An energy (and angular) distribution for the emerging electrons is then obtained by repeating this entire process for a reasonably large number of electrons, generally not less than 200 electrons, and in certain cases more.

We have described above the general scheme of the Monte Carlo calculation for our problem (with additional details supplied below). Martinelli's earlier experience[20] with his relatively simple problem made it clear that without further simplification a comprehensive computer study of the hot-electron problem would be too expensive. The simplification that we decided to employ is the ingenious self-scattering technique of Rees which has proven itself eminently useful in the study of the Gunn effect and related phenomena at the microscopic level.

If there is a constant (energy independent) mean free time (mft) $\tau$ between successive collisions then, by direct analogy with (8b) we can write for $P(t)$, the probability that the electron has gone for time t without scattering,

$$P(t) = \exp\left(-\frac{t}{\tau}\right) \qquad . \qquad (14a)$$

More generally, the scattering time $\tau$ is not a constant, but depends on the (crystal) momentum $\underset{\sim}{k}$: $\tau = \tau(\underset{\sim}{k})$. In this case $P(t)$ is given by the more general relation,

$$P(t) = \exp\left(-\int_0^t \frac{dt}{\tau}\right), \qquad (14c)$$

which is the direct analogue of (8a).

The quantity $\tau(\underset{\sim}{k})$ is normally related to microscopic processes through standard perturbation theory which yields the relation:

$$W_1 = W_1(\underset{\sim}{k}) = \frac{1}{\tau_1(\underset{\sim}{k})} = \int d\underset{\sim}{k}' \, S_1(\underset{\sim}{k},\underset{\sim}{k}') \,, \qquad (15)$$

where $S_1(\underset{\sim}{k},\underset{\sim}{k}') \, d\underset{\sim}{k}'$ is the transition probability, per unit time, for the electron to scatter from state $\underset{\sim}{k}$ to states in the interval $d\underset{\sim}{k}'$ about $\underset{\sim}{k}'$. The subscript '1' has been added to identify the quantities as arising from a given scattering process, of type 1. The quantity $W_1$ is called the scattering frequency (for processes of type 1).

In analogy with $P_{sc}(t)$, previously defined, we define $P_{sc,1}(t)$ as the probability density that the electron scatter in the incremental time interval dt after moving for the time t without scattering. In analogy with (6a) and (6b) we have, respectively:

$$P_{sc,1}(t) = \frac{P_1(t)}{\tau_1} = W_1 P_1(t) = W_1 \exp\left(-\int_o^t W_1(t')dt'\right), \quad (16a)$$

and, for constant mft,

$$P_{sc,1}(t) = \frac{1}{\tau_1} \exp\left(-\frac{t}{\tau_1}\right) = W_1 \exp(-W_1 t) \,. \qquad (16b)$$

The correspondence with the random number variable r' lying between 0 and 1 is given by the direct analogues of (7) and (8), namely,

$$dr' = P_{sc,1}(t) \, dt \qquad , \qquad (17)$$

and

$$r' = \int_o^t P_{sc,1}(t')dt' \qquad (18)$$

Since, by (13a), $P_{sc,1}(t) = \frac{-d}{dt} \exp\left(-\int_o^t W_1(t')dt'\right)$, Eq. (18)

can be written as

$$r = 1 - r' = \exp\left(-\int_o^t W_1(t') \, dt'\right). \qquad (19)$$

If there are different scattering processes then, under the assumption that they operate independently of each other, the total scattering frequency W is the sum of the scattering frequencies characterizing the separate processes: $W = \sum_{i=1}^{n} W_i$, and Eq. 19 generalizes simply to

$$r = \exp\left(-\int_{0}^{t} dt' \sum_{i=1}^{n} W_i(t')\right) \qquad . \qquad (20)$$

For the simple constant mft problem the integration in (19) is easily performed to yield the direct analogue of (10), namely

$$t = -\tau \ln r \qquad . \qquad (21)$$

In general, of course, the integration in (20) cannot be performed analytically. Here the ingenious idea of Rees is brought into play; namely, a fictitious self-scattering process is introduced such that when it is included in the sum $\sum_i W_i$ the integration in (20) can be performed to yield a simple result. The choice of the self-scattering transition probability $S_0(k,k')$ is straightforward:

$$S_0(k,k') = (\Gamma - \sum_{i=1}^{n} W_i) \; \delta(k - k') \qquad , \qquad (22)$$

where $\Gamma$ is an arbitrary, constant frequency which need only exceed $\sum_{i=1}^{n} W_i$, and the delta function is included to ensure self-scattering.

The corresponding self-scattering frequency $W_0$ is given by

$$W_0 = \int dk' \, S_0(k,k') = \Gamma - \sum_{i=1}^{n} W_i \qquad . \qquad (23)$$

But (23) can be re-written in the form

$$\Gamma = \sum_{i=0}^{n} W_i \qquad . \qquad (24)$$

If now the integrand in (20) is extended to include
the self-scattering, i.e., the sum $\sum\limits_{i=1}^{n} W_i$ is replaced by $\sum\limits_{i=0}^{n}$ ,
gives the simple result

$$t = - \frac{1}{\Gamma} \ln r \tag{25}$$

With the parameter $\Gamma$ chosen at the outset, the computer-
generated random number r determines the interval t between
collisions. It still remains to determine the nature of the
collision, whether self-scattering or physical. This requires
another random number. We illustrate this for the simple model
of a single physical scattering mechanism which we assume
corresponds to a constant mfp $\lambda$. The corresponding scattering
time $\tau$ is energy-dependent and is given by

$$\tau_1 = \tau_1(E) = \frac{\lambda}{v(E)} \tag{26}$$

where $v(E)$ denotes the electron velocity at energy E. The
choice of $\Gamma$ must be such what $\Gamma > \frac{1}{\tau_1(E)} = W_1(E)$ for most
energies E that will be encountered.[1] A new, computer-generated
random number r' will now determine whether the collision is

$$\text{physical:} \qquad 0 < r' \leq \frac{W_1(E)}{\Gamma} \tag{27a}$$

or      self-scattering: $\dfrac{W_1(E)}{\Gamma} < r < 1$ . $\tag{27b}$

If the collision is self-scattering the particle proceeds
in its Newtonian trajectory as if it had not made a collision
(hence the terminology, 'self-scattering'). If the collision is
'physical' it is allowed provided $E(t) > \varepsilon_{ph}$ where $\varepsilon_{ph}$ is the
assumed optical phonon energy. If $E(t) < \varepsilon_{ph}$ the collision is
treated as a self-scattering one. For the usual situation,
$E(t) > \varepsilon_{ph}$, the electron emerges from the collision with energy
$E(t) - \varepsilon_{ph}$, and we need further random numbers (as discussed below)

to determine the electron trajectory following the collision.

Note that the choice of a suitable $\Gamma$ is not critical. It should be large enough, but not too large. If it is too large, an inordinate amount of computer time is spent generating self-scattering collisions, which contain no physical information. If one chooses a reasonable $\Gamma$ which then, in mid-calculation, proves to be not large enough, one can increase its value to a new $\Gamma'$ without impairing the calculation.

It remains to discuss the angular distribution of the immediately following the collision. Taking the $k$-vector of the electron just prior to the collision to define a polar axis, the element of solid angle defining the post-collision trajectory can be written as

$$d\Omega = \sin\theta d\theta d\phi = d\mu d\phi \quad , \quad \mu = \cos\theta \quad , \quad (28)$$

where $\theta$ is the polar angle, i.e., the angle between $k'$ and $k$, and $\phi$ is the azimuthal angle.

If $P(\mu)$ is the normalized probability density (in $\mu$) for scattering into the angle $\mu$, then the connection with a computer-generated random number $r$ in the interval 0 to 1 is:

$$r = \int_{-1}^{\mu} P(\mu) \ d\mu \quad , \quad \text{with} \quad \int_{-1}^{1} P(\mu) \ d\mu = 1. \quad (29)$$

The several cases we have studied are as follows:

(i) Isotropic scattering

Here all $\mu$ are weighted equally so that (29) gives

$$P_I(\mu) = \frac{1}{2} \quad , \text{independent of} \quad \mu, \quad r = \frac{1}{2} \ ( \mu + 1), \quad (30a)$$

or

$$\mu = 2r - 1. \quad (30b)$$

The subscript I in (30a) is used to denote isotropic scattering.

Likewise all $\phi$ are weighted equally so that

$$P(\phi) = \frac{1}{2\pi} \quad , \quad r = \int_{0}^{\phi} P(\phi)d\phi = \frac{\phi}{2\pi} \quad , \qquad (31a)$$

or

$$\phi = 2\pi r \qquad . \qquad (31b)$$

## (ii) Dominant Forward Scattering

Here we have arbitrarily taken the simplest forward scattering law, namely $P_F(\cos\theta) \propto 1 + \cos\theta$, to represent schematically the effects of dominant forward scattering:

$$P_F(\mu) = \frac{1}{2}(1 + \mu) \quad , \quad r = \frac{1}{2}(\frac{1}{2}\mu^2 + \mu + \frac{1}{2}) \quad , \qquad (32a)$$

or, solving for $\mu$ :

$$\mu = 2\sqrt{r} - 1 \qquad . \qquad (32b)$$

The distribution of the azimuthal angle $\phi$ is again given by (31a) and (31b).

## iii) Dominant Backward Scattering

As with forward scattering, we have taken the simplest backward scattering law to represent schematically the effects of dominant backward scattering, namely $P_B(\cos\theta) \propto 1 - \cos\theta$, or

$$P_B(\mu) = \frac{1}{2}(1 - \mu) \quad , \quad r = \frac{1}{2}(\frac{1}{2}\mu^2 - \mu + \frac{1}{2}) , \qquad (33a)$$

or, solving for $\mu$ ,

$$\mu = 1 - 2\sqrt{r} \qquad . \qquad (33b)$$

The distribution of the azimuthal angle $\phi$ is again given by (31a) and (31b).

(iv) Polar Optical Phonon Scattering

Here the starting point is the scattering relationship[21]

$$W_{PO}(\mu) = \frac{const}{|k'-k|^2} = \frac{const}{k'^2 + k^2 - 2kk'\mu} \qquad . \qquad (34)$$

Through some straightforward algebra we obtain the desired relation of $\mu$ with the random number $r$ :

$$r = \frac{\ln\left[\dfrac{(k + k')^2}{(k-k')^2 + 2kk'(1-\mu)}\right]}{\ln\left[\dfrac{(k + k')^2}{(k - k')^2}\right]} \qquad . \qquad (35)$$

Conservation of energy, for phonon emission, is:

$$E = \frac{\hbar^2 k^2}{2m} = \frac{\hbar^2 k'^2}{2m} + \hbar\omega_0 \qquad . \qquad (36)$$

Further algebra enables us to express conveniently $\mu$ in terms of $r$:

$$\mu = 1 - \frac{(\sqrt{\eta} + \sqrt{\eta-1})^2 \exp(^{-r}\eta) - (\sqrt{\eta} - \sqrt{\eta-1})^2}{2\sqrt{\eta}\sqrt{\eta-1}} \qquad , \quad (37a)$$

with

$$r_\eta = r \ln\left(\frac{\sqrt{\eta} + \sqrt{\eta-1}}{\sqrt{\eta} - \sqrt{\eta-1}}\right)^2 \qquad , \quad \eta = \frac{\cdots}{ph} \qquad . \qquad (37b)$$

C. Computer Results for Constant MFP Problems

    (i) Three-Dimensional Computations, Isotropic Scattering

The above discussion presents in considerable detail the basic ingredients that have gone into our Monte Carlo studies of the hot-electron problem. Beyond this point we are dealing with

straight programming which need not be discussed here. We there-
fore proceed directly to the results. In Fig. 19 is plotted the
average energy $E_{ave}$ of the electron emerging from the film as a
function of film thickness t, for the situation of constant mfp
and isotropic scattering. Six different cases are plotted,
corresponding to two different starting energies: $E_o$ = 0.01ev and
$E_o$ = 16 ev, three different field strengths: F = 5 x $10^5$ V/cm,
F = 1 x $10^6$V/cm and F = 2 x $10^6$ V/cm, and three different mfp's:
$\lambda$ = 25Å, $\lambda$ = 50Å and $\lambda$ = 100Å. However, for all cases F$\lambda$ is
the same, namely F$\lambda$ = 0.5 V; likewise $\varepsilon_{ph}$ is common to all cases,
namely $\varepsilon_{ph}$ = 0.1 ev. It is seen that , at sufficiently large
thicknesses t $\stackrel{>}{\sim}$ 4500Å, all of the cases have converged to the
common value, $E_{ave,ss}$ = 2.1 ev. (subscript 'ss' denotes steady
state). This one plot already leads to the conclusion that
$E_{ave,ss} \propto (F \lambda)^n$. From theoretical work of Wolff[22], as well as
further computer studies (see Figs. 23, 28, 29), the more precise
relation follows:

$$E_{ave,ss} = k \frac{(F \lambda)^2}{\varepsilon_{ph}} \quad , \quad k = 0.87 \quad . \tag{38}$$

This relation had already been found in the earlier computer
studies of Martinelli[20], who determined k = 0.88. We have
shown (38) to hold (with a variance of k less than 10%) over
the range of energies 0.5 $\stackrel{<}{\sim} E_{ave,ss} \stackrel{<}{\sim}$ 18 ev. (An actual
plot of $E_{ave,ss}$ vs. $(F \lambda)^2/\varepsilon_{ph}$ is given in Fig. 23, the middle
straight line).

It has also been found through the computer studies
that, for the constant mfp isotropic-scattering problem, the
electrons warm up or cool down to the steady-state energy in an
exponential manner:

$$E_{ave} - E_{ave,ss} = (E_o - E_{ave,ss}) \exp(- \frac{t}{D}) \tag{39}$$

AVERAGE ENERGY OF EMERGENCE
ISOTROPIC SCATTERING

| | $E_0$(eV) | F(V/cm) | $\lambda$(Å) |
|---|---|---|---|
| ● | .01 | $2 \times 10^6$ | 25 |
| ▲ | 16 | $2 \times 10^6$ | 25 |
| + | .01 | $5 \times 10^5$ | 100 |
| × | 16 | $5 \times 10^5$ | 100 |
| △ | .01 | $1 \times 10^6$ | 50 |
| ○ | 16 | $1 \times 10^6$ | 50 |

NUMBER OF PARTICLES = 500
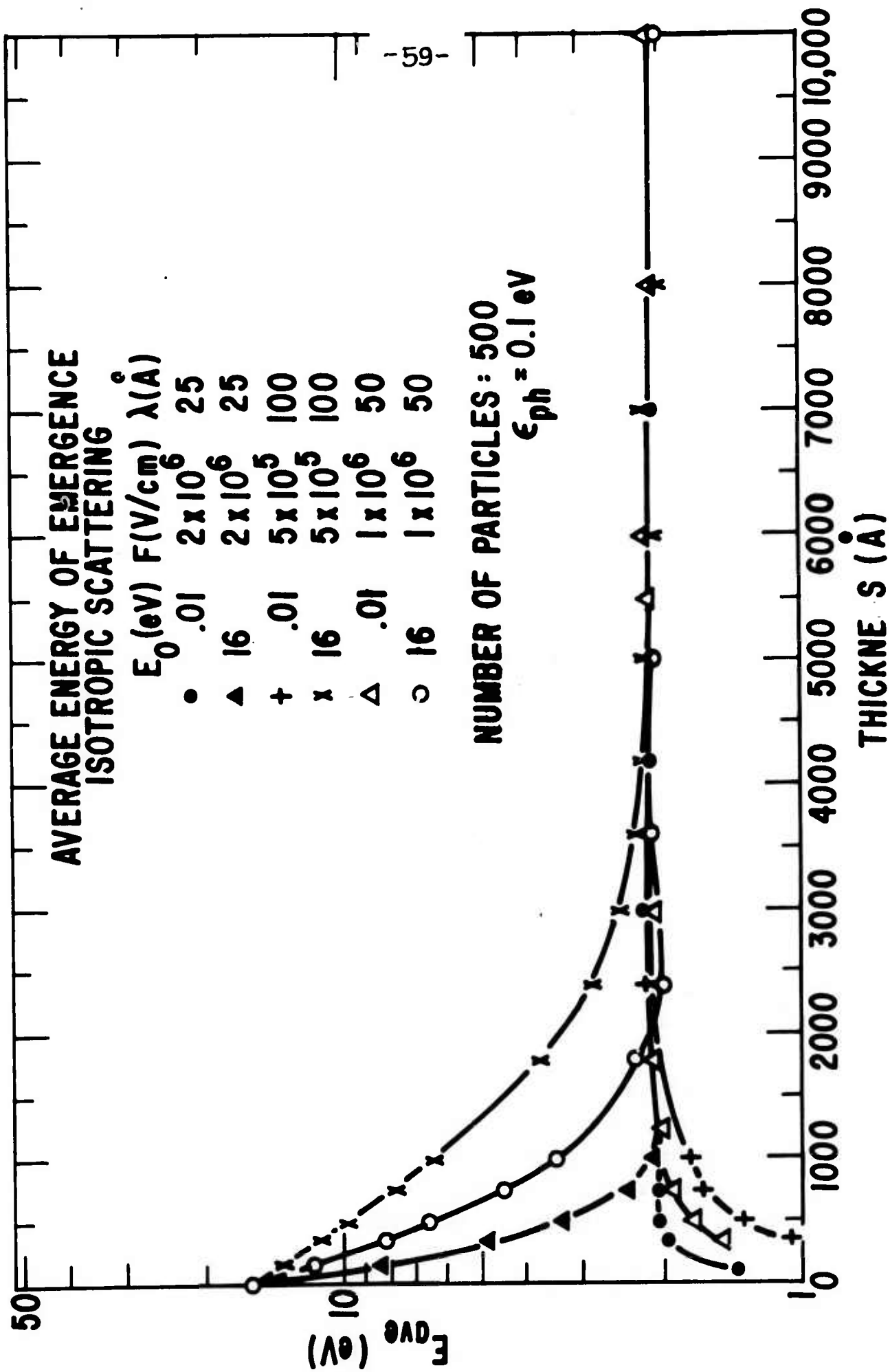$\epsilon_{ph} = 0.1$ eV

THICKNESS (Å)

FIG. 19

-59-

with $E_o$ the initial energy of the electrons, at the entrance plane $t = 0$.

In our computer studies to-date we have taken $E_o$ as mono-energetic; if the electrons enter with an energy distribution, then presumably (39) still holds (at least, approximately) with $E_o$ replaced by $E_{o,ave}$. The development distance obeys an approximate scaling law similar to (38), namely

$$D = k' \frac{F\lambda^2}{\varepsilon_{ph}} \quad , \qquad \text{with } 1 \lesssim k' \lesssim 2. \qquad (40)$$

Martinelli[20], in his more restricted study, found $k' = 1.27$. The development distance for the six cases considered in Fig. 19 is established by the plots in Fig. 20.

### (ii) Three Dimensional Computations, Anisotropic Scattering

In addition to the isotropic scattering case, anisotropic scattering cases have also been studied for the constant mfp problem. In Fig. 21 is plotted the average energy $E_{ave}$ of the emerging electrons vs. film thickness t for two different examples of forward scattering: moderate forward scattering characterized by a $(1 + \cos \theta)$ distribution and with $\mu$ related to r through (32a) and (32b), polar-optical forward scattering as given by (34) thru (37b). For each of the two examples we have taken two widely separated starting energies, a low energy and a high energy. We see that there is indeed a steady-state average energy for each of the two examples, and that this energy is higher for the polar-optical case, $E_{ave,ss} = 12.2$ ev, than for the $(1 + \cos \theta)$ case, $E_{ave,ss} = 3.0$ ev, both being calculated for the same parameter values: $\lambda = 50\text{Å}$, $\varepsilon_{ph} = 0.1$ ev and $F = 1 \times 10^6$ V/cm. This result is expected since polar-optical scattering is more strongly peaked in the forward direction. The vertical line bracketing each average-energy point is not an error bar; rather, it gives directly the half-width of the energy

DEVELOPMENT DISTANCE OF AVERAGE ENERGY
ISOTROPIC SCATTERING

$$D = k' \frac{F\lambda^2}{\epsilon_{ph}}$$

| | F(V/cm) | λ(Å) | $\epsilon_{ph}$(eV) | $E_0$(eV) | k' | D(Å) |
|---|---|---|---|---|---|---|
| o | $10^6$ | 50 | 0.1 | 0.01 | 1.11 | 278 |
| ▲ | $10^6$ | 50 | 0.1 | 16.0 | 1.66 | 416 |
| x | $5 \times 10^5$ | 100 | 0.1 | 0.01 | 1.03 | 514 |
| ● | $5 \times 10^5$ | 100 | 0.1 | 16.0 | 1.66 | 831 |
| + | $2 \times 10^6$ | 25 | 0.1 | 0.01 | 1.07 | 134 |
| □ | $2 \times 10$ | 25 | 0.1 | 16.0 | 1.65 | 206 |

$\left| \dfrac{E_{ave} - E_{ave,ss}}{E_0 - E_{ave,ss}} \right|$

0.1

0.01

1000    2000    3000    4000    5000    6000

THICKNESS (Å)

FIG. 20

FIG. 21

SPATIAL DEVELOPMENT OF DISTRIBUTION FOR FORWARD SCATTERING

POLAR OPTICAL DISTRIBUTION

$1 + \cos\theta$ DISTRIBUTION

$\lambda = 50\ \text{Å}$
$\epsilon_{ph} = 0.1\ \text{eV}$
$F = 10^6\ \text{V/cm}$

THICKNESS (Å)

$E_{ave}$ AND WIDTH OF DISTRIBUTION
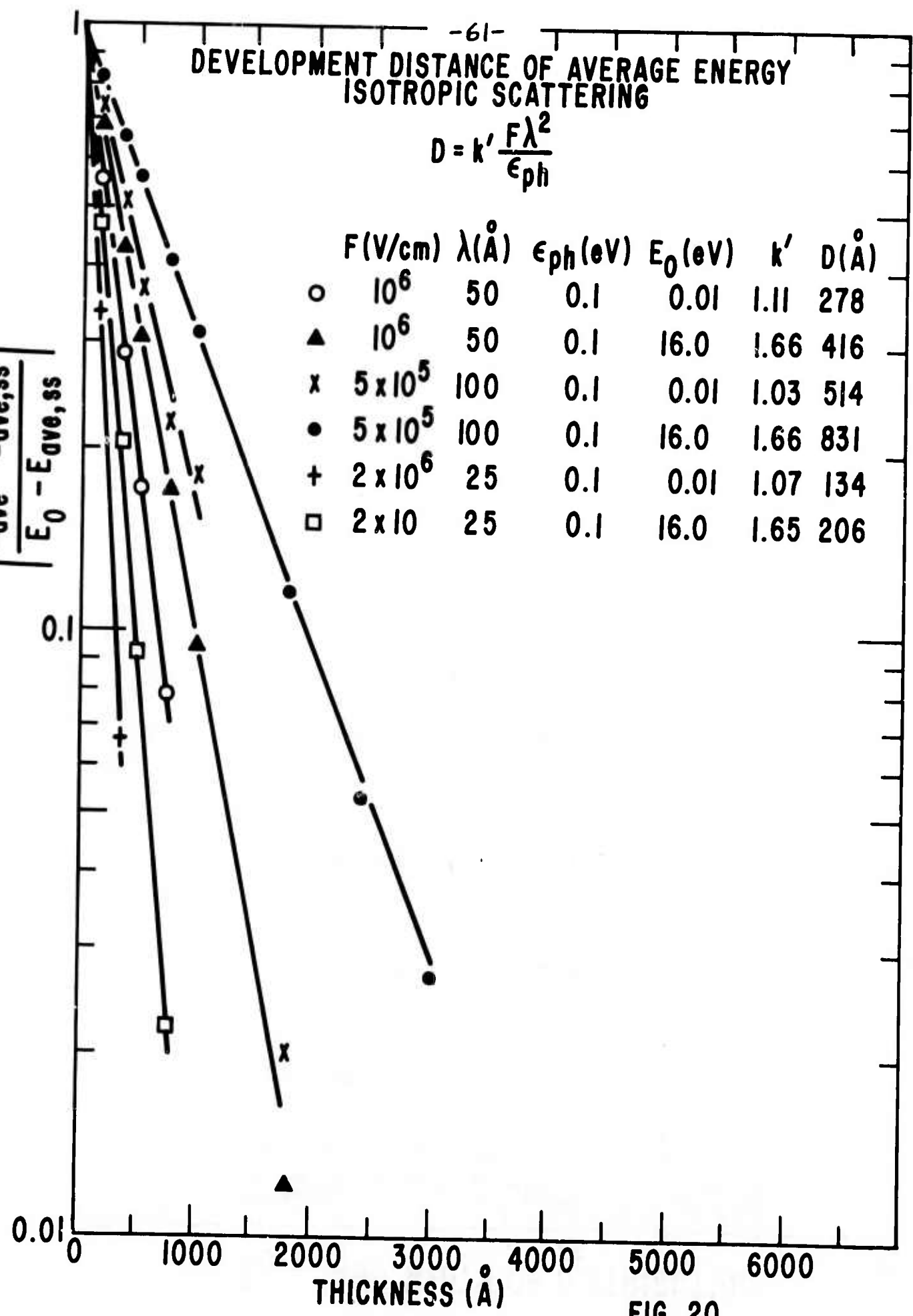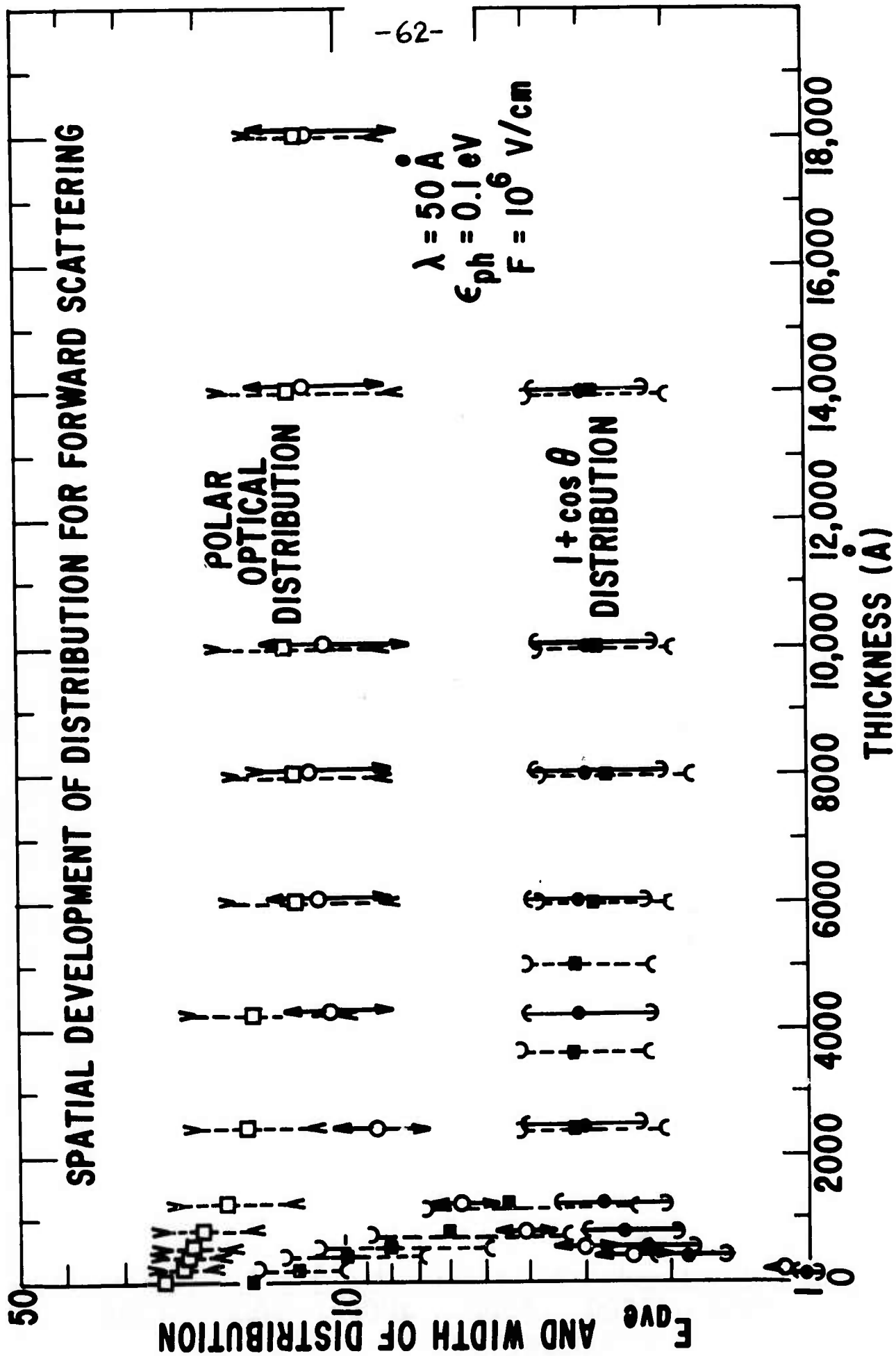
distribution. [In a precise formulation of the polar-optical
scattering problem the mean free path is not a constant, but is
energy-dependent, increasing with increasing energy. We have an
approximate formulation of energy-dependent mean-free-path problems,
discussed below, which enables us to study them first as constant
mean-free-path problems.] A corresponding plot for moderate
backward scattering characerized by a $(1 - \cos \theta)$ distribution
and with related to r through (33a) and (33b) is presented in
Fig. 22. The $\lambda$, $\epsilon_{ph}$ and F are the same as in Fig. 21. The value
of $E_{ave,ss}$ is now 1.6 ev, lower than the two values for the
forward scattering examples of Fig. 21, as expected.

We have already noted the proper scaling law for
$E_{ave,ss}$, for the isotropic scattering case, in Eq. (38). The
same scaling law holds for the moderate anisotropies: forward
scattering characterized by a $(1 + \cos \theta)$ distribution, and
backward scattering characterized by a $(1 - \cos \theta)$ distribution,
as seen by the straight-line plots for the three kinds of
scatterings in Fig. 23. The corresponding proportionality
constants $k_I$, $k_F$, $k_B$ (I for isotropic, F for forward and B for
backward) are $K_I = 0.87$, $k_F = 1.27$ and $k_B = 0.66$. Note that
$k_B < k_I < k_F$, as physically expected. An approximate scaling
law exists for polar optical scattering (however, with constant
mfp), and is mentioned below.

The fact that anisotropic scattering, no matter how
strongly forward [short of pure (100%) forward scattering] by
itself (that is, without an energy-dependent mfp) leads to a
stable distribution has been verified by calculations with a
one-dimensional model, as described below. This situation can
be understood theoretically by noting that even though the
probability for forward scattering along a trajectory is large,
there is a finite probability that the electron be backward
scattered. Once a high energy electron, the trajectory of which
is not appreciably affected by the field, is back-scattered in
the direction against the field, it will continue to travel in

SPATIAL DEVELOPMENT OF DISTRIBUTION
FOR BACKWARD SCATTERING
$(1-\cos\theta)$

$\lambda = 50\ \overset{\circ}{A}$
$\epsilon_{ph} = 0.1\ eV$
$F = 10^6\ V/cm$

$E_{ave}$ AND WIDTH OF DISTRIBUTION

THICKNESS $(\overset{\circ}{A})$

FIG. 22

3-dim CALCULATIONS
FOR CONSTANT mfp

○ ISOTROPIC
● $1 + \cos\theta$
▲ $1 - \cos\theta$

$E_{ave,\,ss}$ (eV)

$(F\lambda)^2/\epsilon_{ph}$ (eV)
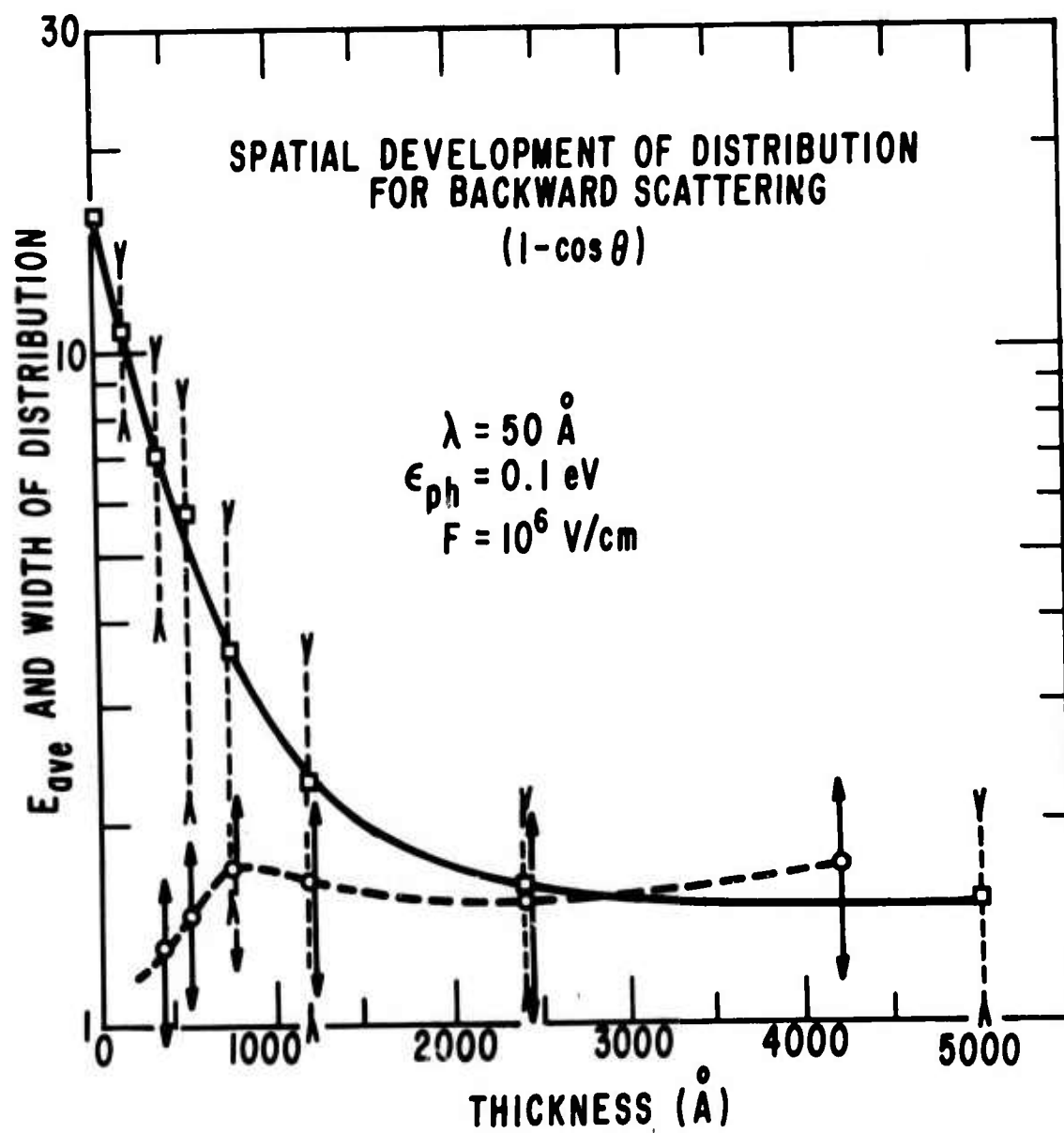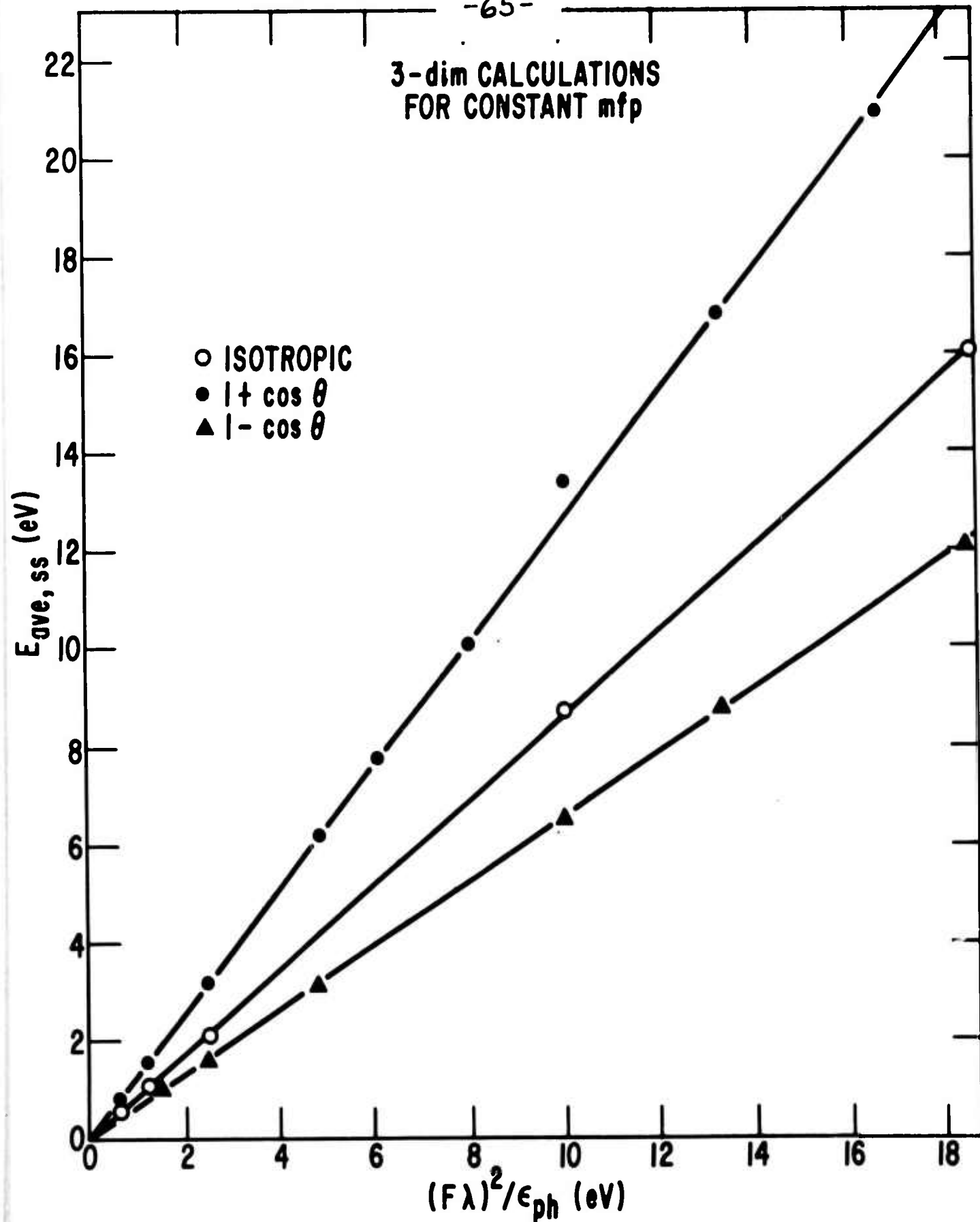
FIG. 23

that direction (as the electron has high probability of being
scattered forward along the trajectory) until the small-
probability event that it be scattered in the opposite direction
from the direction of the trajectory occurs, or until it loses
enough energy such that the field can turn it around along its
own direction.  The existence of this cooling mechanism
stabilizes the electron energy distribution and a steady
state thus exists.

### (iii) One-Dimensional Simulations

Even with the saving in computer time gained through use
of the self-scattering technique, the three-dimensional calculations
required with anisotropic scattering are still quite costly.
Therefore further simplification is highly desirable.  With this
aim in mind we decided to explore the usefulness of one-dimensional
models in simulating the full three-dimensional problems.  The
simplest possible one-dimensional model is the random walk in one
dimension.  The particle is constrained to move on a line and after
moving a fixed distance $\lambda$ (the same $\lambda$ which characterizes the con-
stant mfp problem in three dimensions) along its trajectory on
the line it makes a collision.  Note however that this is not the
classical random-walk problem, which deals with force-free
situations.  Here the electron is acted on by the electric field
(directed along the line) throughout its motion.  In other
words, our problem is a random walk in a force field.  The first
problem of this kind which we studied is the analog of the
isotropic scattering problem.  Here, and in the following, we
shall always be referring to constant mfp situations, both in
three and in one dimensions.  The obvious one-dimensional analog
of isotropic scattering is equal probabilities for scattering
forward and backward on the line respectively.  In Fig. 24 we
compare the spatial evolution of the average energy $E_{ave}$ for
the two problems with the same parameters: $E_o$ = 0.01 ev,
$\lambda$ = 50Å , $\varepsilon_{ph}$ = 0.1 ev, and F = 1 x $10^{\prime}$ V/cm.

ISOTROPIC SCATTERING

$\epsilon_{ph} = 0.1$ eV
$F = 10^6$ V/cm
$E_0 = 0.01$ eV
$\lambda = 50$ Å

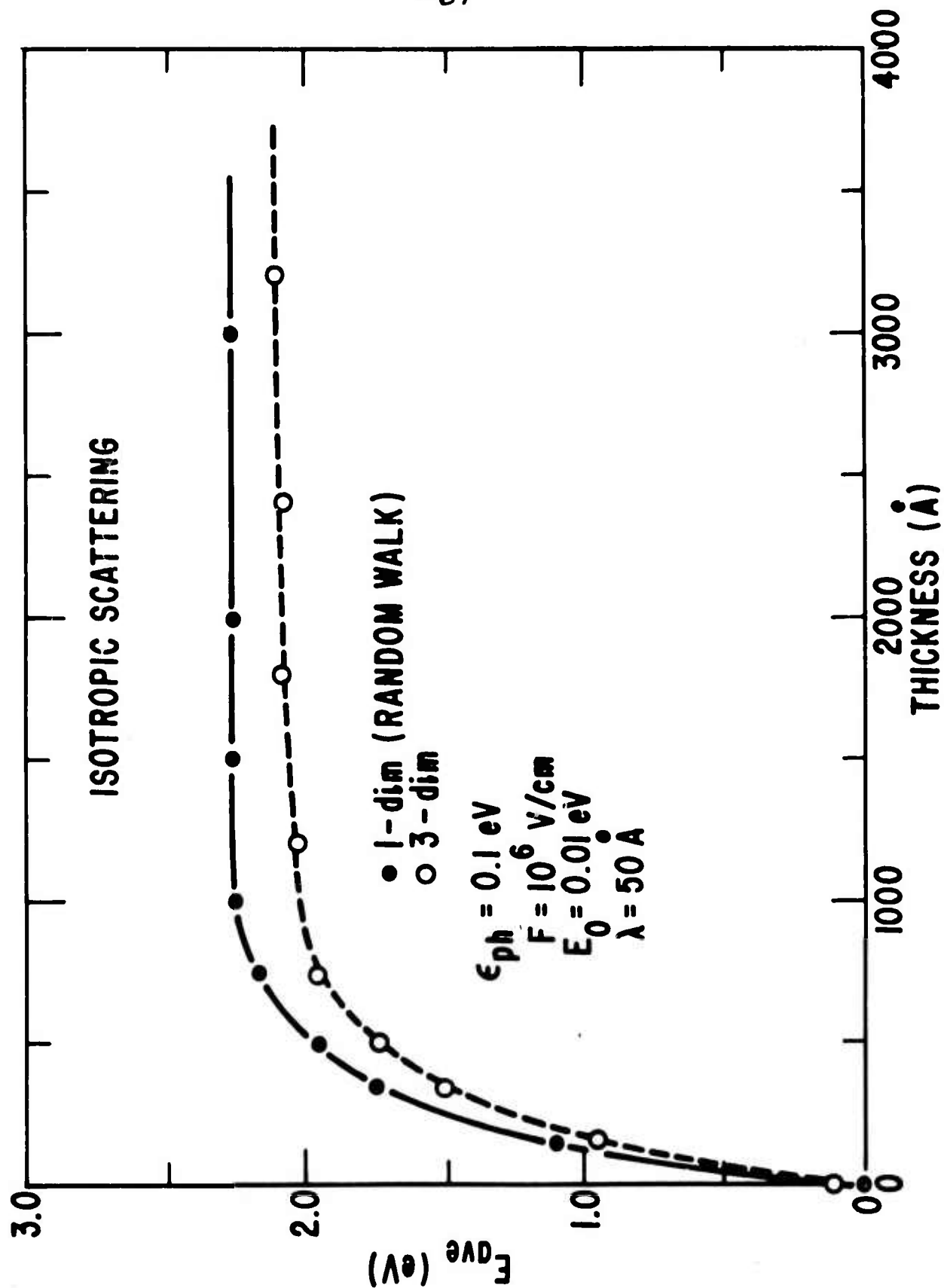• 1-dim (RANDOM WALK)
○ 3-dim

THICKNESS (Å)

FIG. 24

$E_{ave}$ (eV)

In Fig. 25 the spatial evolutions of $E_{ave}$ for the two problems are compared for the same parameters except for $E_0$ which is now a higher energy. Figures 24 and 25 indicate how good a simulation the one-dimensional random walk furnishes for the three-dimensional problem. The one-dimensional curves in Figs. 24 and 25 are re-plotted in Fig. 26 to show their convergence to a common value of $E_{ave,ss}$. The development distance for five cases, in one dimension, is established by the plots in Fig. 27 (the analog to Fig. 20).

The problem of finding the most suitable one-dimensional random walk (in a force field) to simulate a given anisotropic three-dimensional problem is one step more subtle. The added complexity comes from the need to establish the proper value for f, the probability for 'forward' scattering on the line (1-f is then the probability for 'backward' scattering on the line). After trying unsuccessfully to establish the proper value of f by guessing 'appropriate' averages for the three-dimensional anisotropy, we switched to a very simple, straightforward trial-and-error method. We have already noted, in Fig. 23, that for each of the three-dimensional problems: isotropic, $(1 + \cos \theta)$ and $(1 - \cos \theta)$ scattering, $E_{ave,ss} \propto (F \lambda)^2/\varepsilon_{ph}$. It would seem reasonable that, whatever the value of f between 0 and 1 the same scaling law would hold; but with a different constant-of-proportionality $k_f$ corresponding to each f. That this is indeed true is seen in Fig. 28. Knowing the k of the scaling law (assumed given by Eq. (38) for any given anisotropic, three-dimensional problem it is only necessary to find that f for which $k_f$ is the same k. Using this criterion, we find from Fig. 28 that the appropriate f for the one-dimensional simulation of the $(1 + \cos \theta)$-anisotropy is $f = 0.6$, and that the appropriate f for the simulation of the $(1 - \cos \theta)$-anisotropy is $f = 0.4$. We would also expect that the spatial development of $E_{ave}$ to its steady-state value $E_{ave,ss}$ is given by Eq. (39), with the same

ISOTROPIC SCATTERING

▲ 1-dim (RANDOM WALK)
○ 3-dim

$\lambda = 50 \text{ Å}$
$E_0 = 16.0 \text{ eV}$
$\epsilon_{ph} = 0.1 \text{ eV}$
$F = 10^6 \text{ V/cm}$

THICKNESS (Å)

FIG. 25

$E_{ave} \text{ (eV)}$

ISOTROPIC SCATTERING

1-dim (RANDOM WALK)

$\lambda = 50$ Å
$\epsilon_{ph} = 0.1$ eV
$F = 10^6$ V/cm

FIG. 26

THICKNESS (Å)

$E_{ave}$ (eV)

SPATIAL DEVELOPMENT FOR
1-dim (RANDOM WALK) WITH ISOTROPIC
SCATTERING (0.5, 0.5) AND $E_0 = 0.01$ eV

| | F (V/cm) | $\lambda(\overset{\circ}{A})$ | $\epsilon_{ph}$(eV) | $F\lambda^2/\epsilon_{ph}(\overset{\circ}{A})$ |
|---|---|---|---|---|
| x | $10^6$ | 25 | 0.05 | 125 |
| ● | $10^6$ | 50 | 0.1 | 250 |
| □ | $2\times10^6$ | 50 | 0.2 | 250 |
| ○ | $2\times10^6$ | 50 | 0.1 | 500 |
| ▲ | $2\times10^6$ | 100 | 0.2 | 1000 |

THICKNESS ($\overset{\circ}{A}$)

FIG. 27

COMPARISON OF 1-dim (RANDOM WALK) AND 3-dim CALCULATIONS FOR CONSTANT mfp PROBLEMS
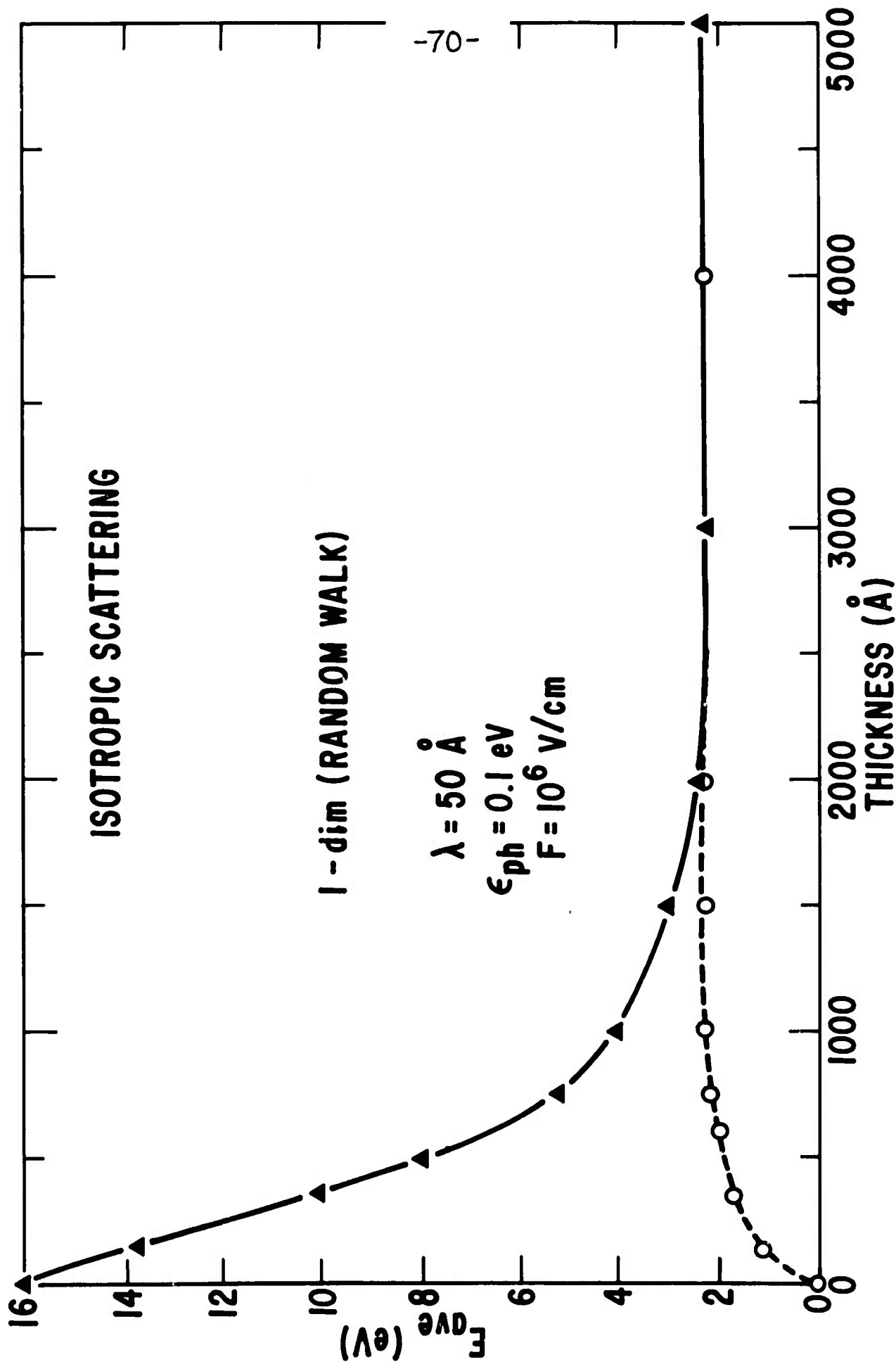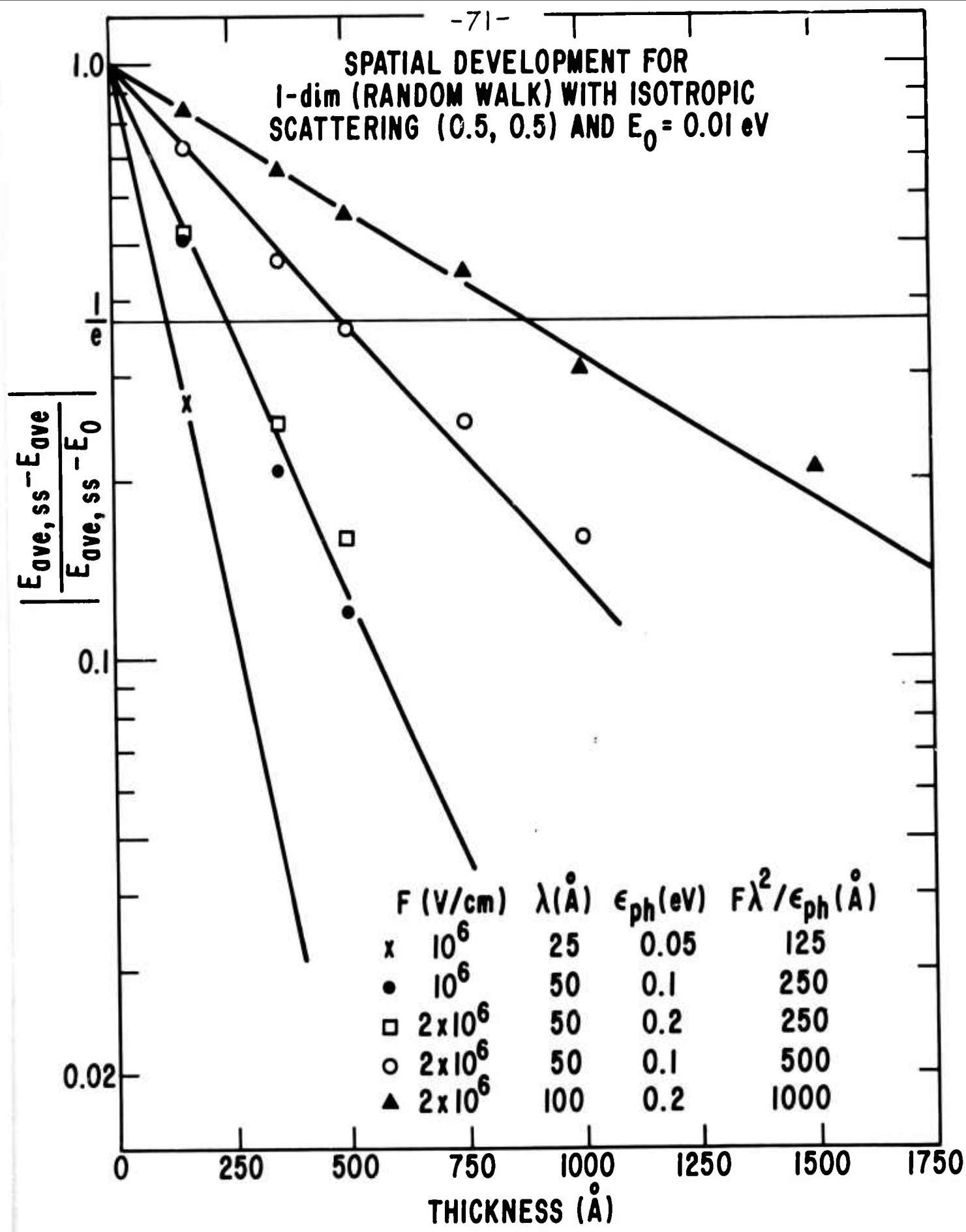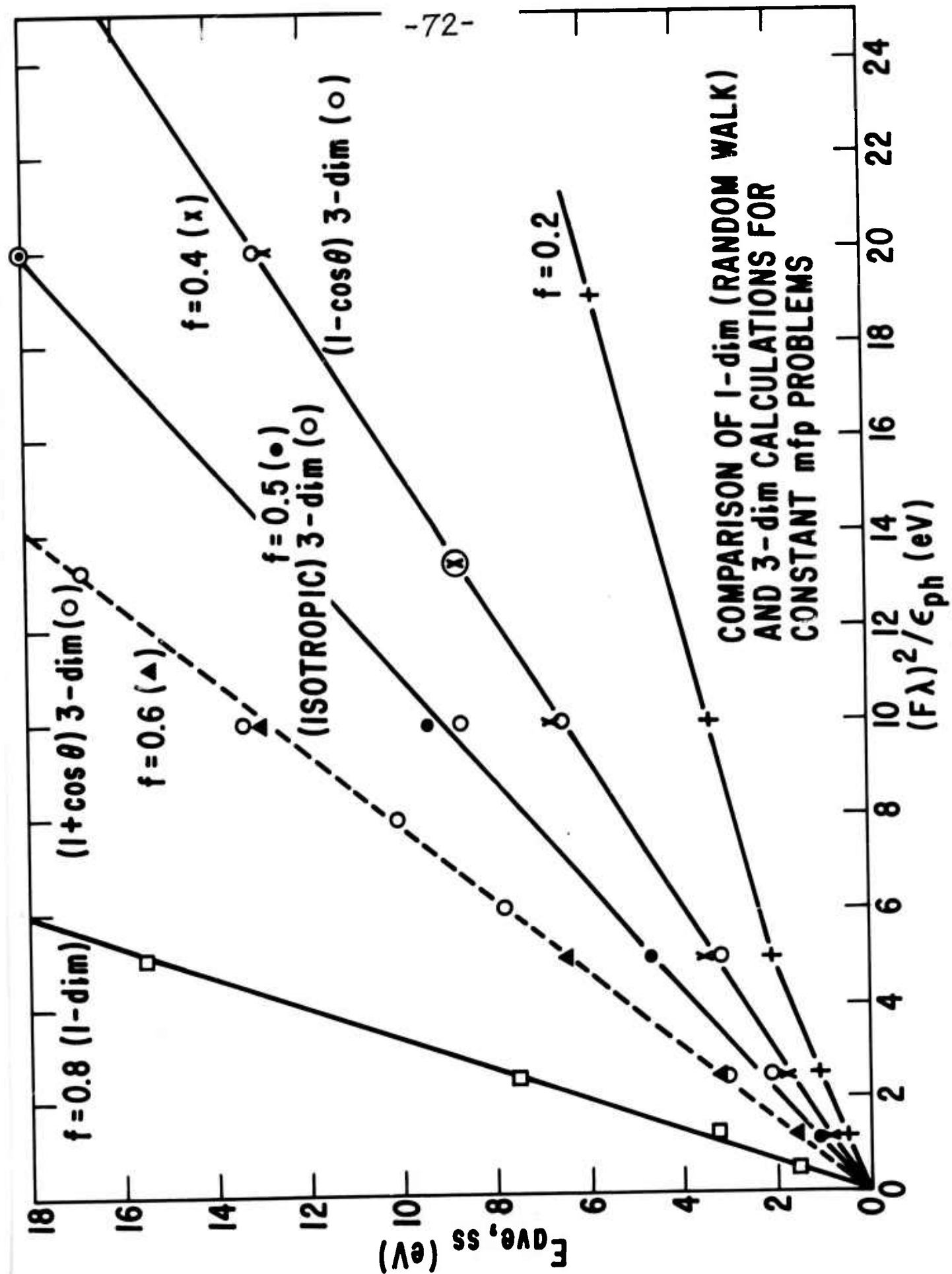FIG. 28

-72-

scaling law (40) for D, only a new constant $k'_f$ corresponding to
the new value of f. That this is indeed true is seen in Fig. 29
which gives a plot of the development distance D vs. $F \lambda^2/\epsilon_{ph}$
for the three one-dimensional cases: f = 0.6 (moderately forward
scattering) and k' = 1.40, f = 0.5 (isotropic scattering) and
k' = 0.94 [ compared to $1 \lesssim k' \lesssim 2$ for the three-dimensional
isotropic case], and f = 0.4 (moderately backward scattering)
and k' = 0.68.

A direct comparison of three-dimensional (1 + cos θ)-
scattering and f = 0.6 one-dimensional scattering is given in
Fig. 30, which presents a plot of $E_{ave}$ vs. film thickness t for
the two problems under 'identical' conditions: $E_o$ = 0.01 ev,
$\lambda$ = 100Å, $\epsilon_{ph}$ = 0.1 ev, and F - 1 x $10^6$ V/cm. The agreement
is seen to be excellent. Note also that the relative widths
of the two distributions is almost identical: $(\sigma/E_{ave})_{ss}$ = 0.53
and 0.51 for the three-and one-dimensional cases respectively.
Here
$$\sigma = \sqrt{(E^2)_{ave} - E_{ave}^2}$$
and ss, as usual, denotes the

steady state. Figure 31 describes the approach to the steady
state as a function of film thickness for five cases for the
one-dimensional, f = 0.6 problem.

A direct comparison of three-dimensional (1 - cos θ)-
scattering and f = 0.4 one-dimensional scattering is given in
Fig. 32 for the two problems under 'identical' conditions for
two choices of parameter values: $E_o$ = 0.01 ev, $\lambda$ = 100Å,
$\epsilon_{ph}$ = 0.075 ev, and F - 1 x $10^6$ V/cm; $E_o$ = 0.01 ev, $\lambda$ = 50Å,
$_{ph}$ = 0.1 ev, and F = 1 x $10^6$ V/cm. Again, the agreement is
seen to be excellent. Figure 33 describes the approach to
the steady state with film thickness for five cases for the
one-dimensional, f = 0.4 problem.

Before leaving the constant mfp problem we show two
sets of results for the polar optical phonon scattering problem
treated as a constant mfp problem ( $\lambda$ = const, but the anisotropy

FIG. 29

FORWARD SCATTERING

- 1-dim (RANDOM WALK) (0.6, 0.4); $\left(\dfrac{\sigma}{E_{ave}}\right)_{ss} = 0.53$

o 3-dim $(1 + \cos\theta)$; $\left(\dfrac{\sigma}{E_{ave}}\right)_{ss} = 0.51$

$\lambda = 100 \text{ Å}$
$E_0 = 0.01 \text{ eV}$
$\epsilon_{ph} = 0.1 \text{ eV}$
$F = 10^6 \text{ V/cm}$

THICKNESS (Å)

$E_{ave}$ (eV)

FIG. 30

SPATIAL DEVELOPMENT FOR
1-dim (RANDOM WALK) WITH FORWARD
SCATTERING (0.6, 0.4) AND $E_0 = 0.01$ eV

| F (V/cm) | $\lambda(\mathring{A})$ | $\epsilon_{ph}$(eV) | $F\lambda^2/\epsilon_{ph}(\mathring{A})$ |
|---|---|---|---|
| ▲ $10^6$ | 100 | 0.1 | 1000 |
| ○ $10^6$ | 25 | 0.05 | 125 |
| ✗ $10^6$ | 50 | 0.1 | 250 |
| ● $10^6$ | 50 | 0.05 | 500 |
| □ $2 \times 10^6$ | 100 | 0.2 | 1000 |

THICKNESS ($\mathring{A}$)    FIG. 31

BACKWARD SCATTERING
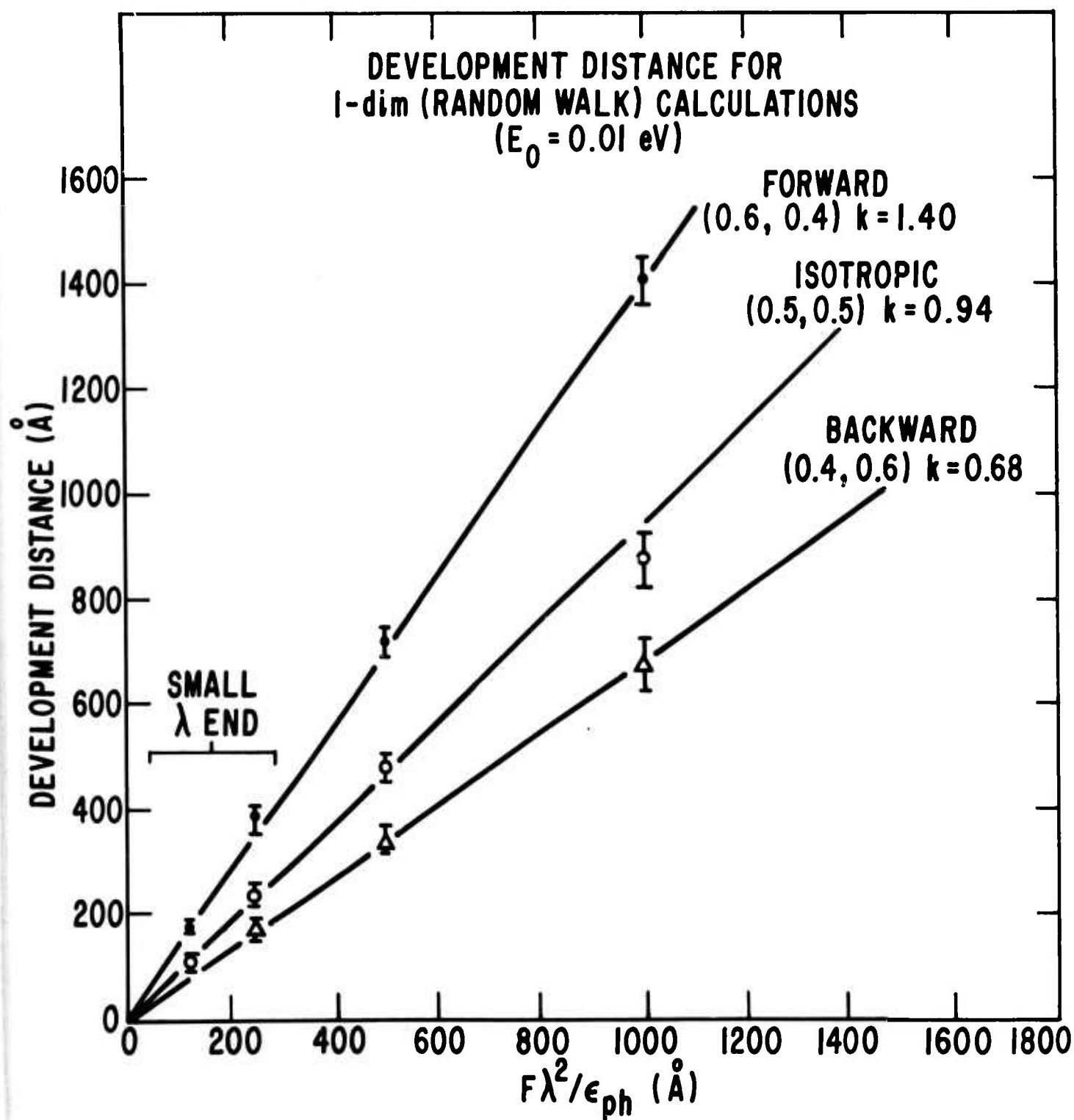
FIG. 32

FIG. 33

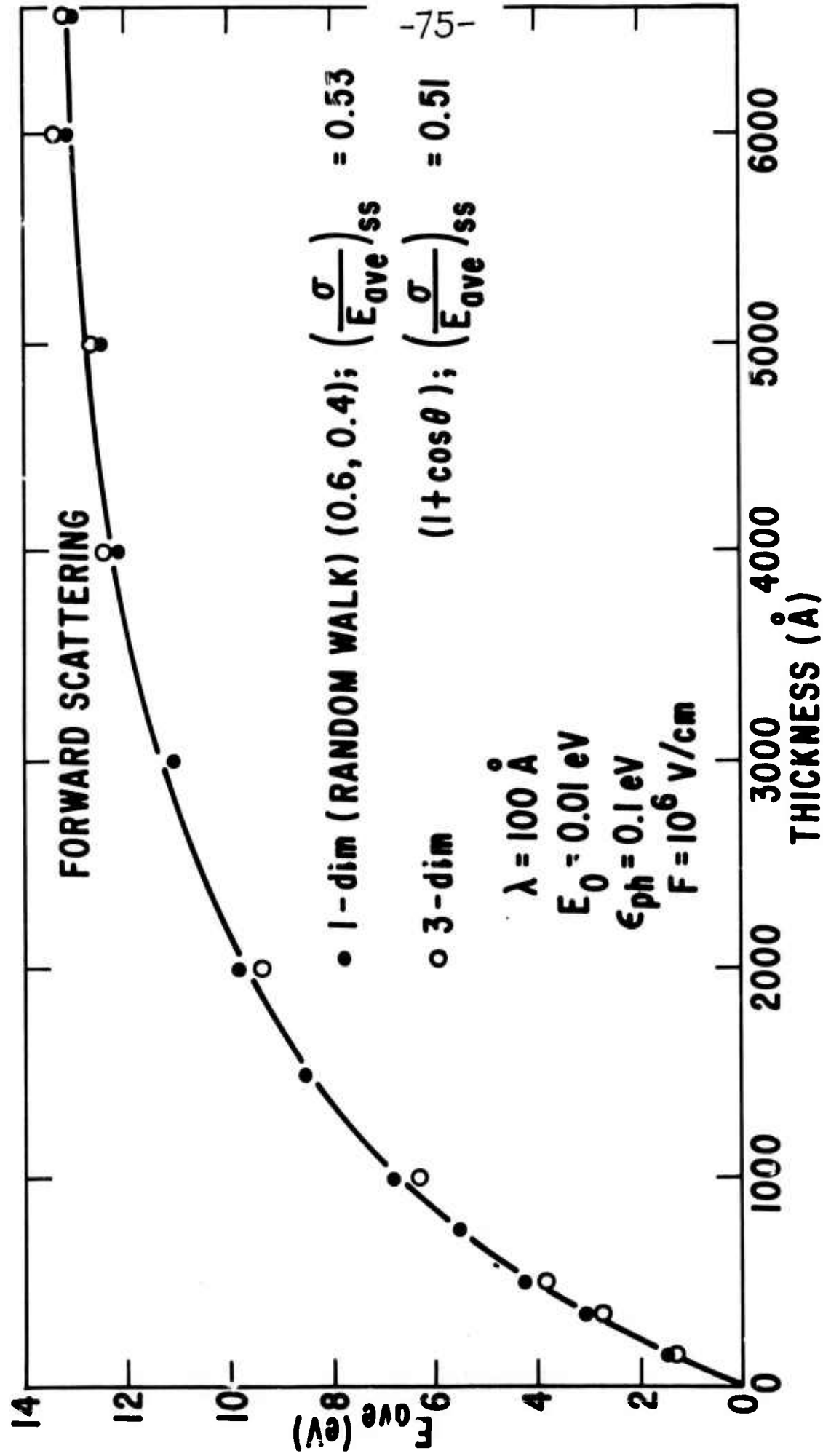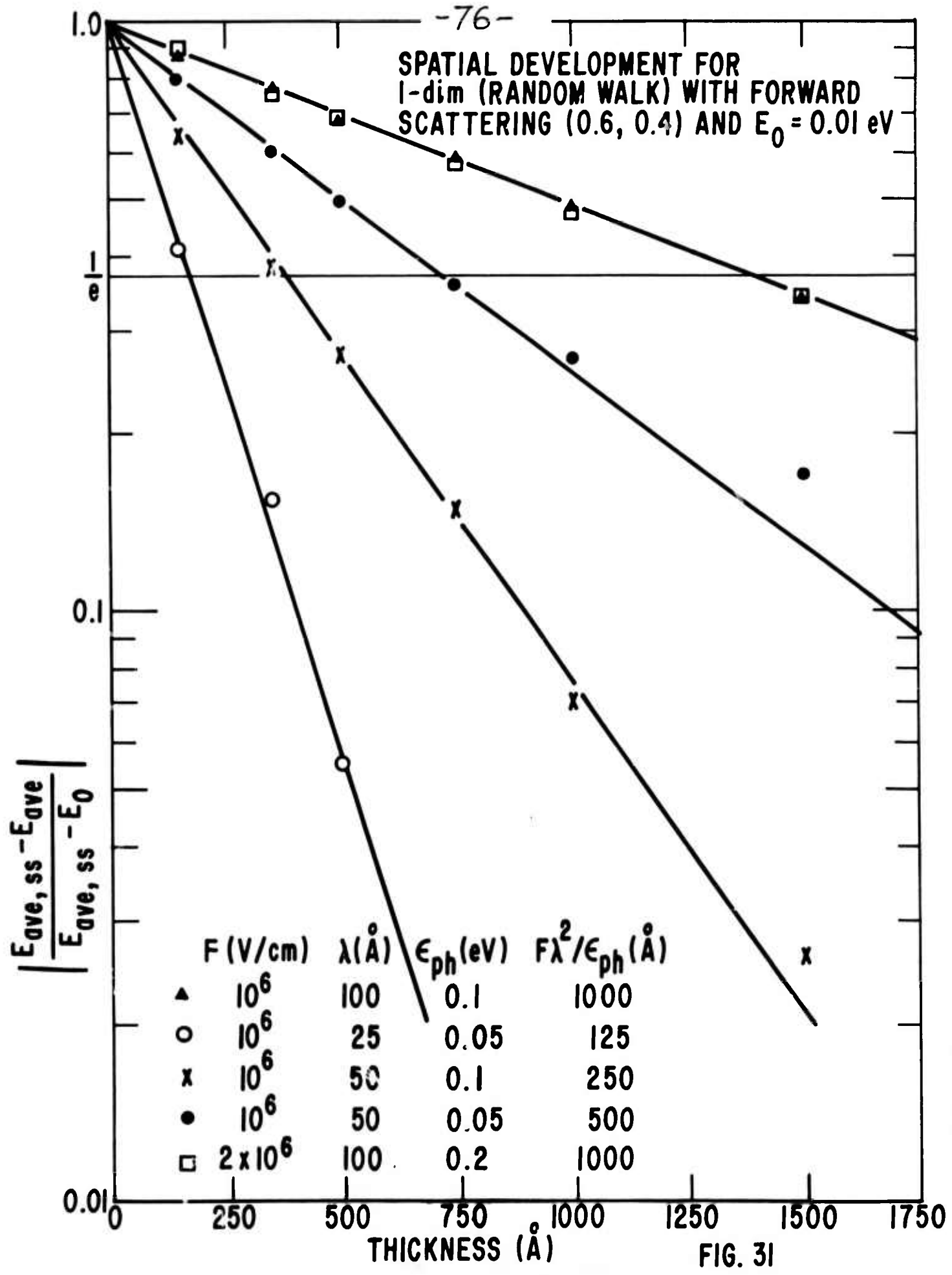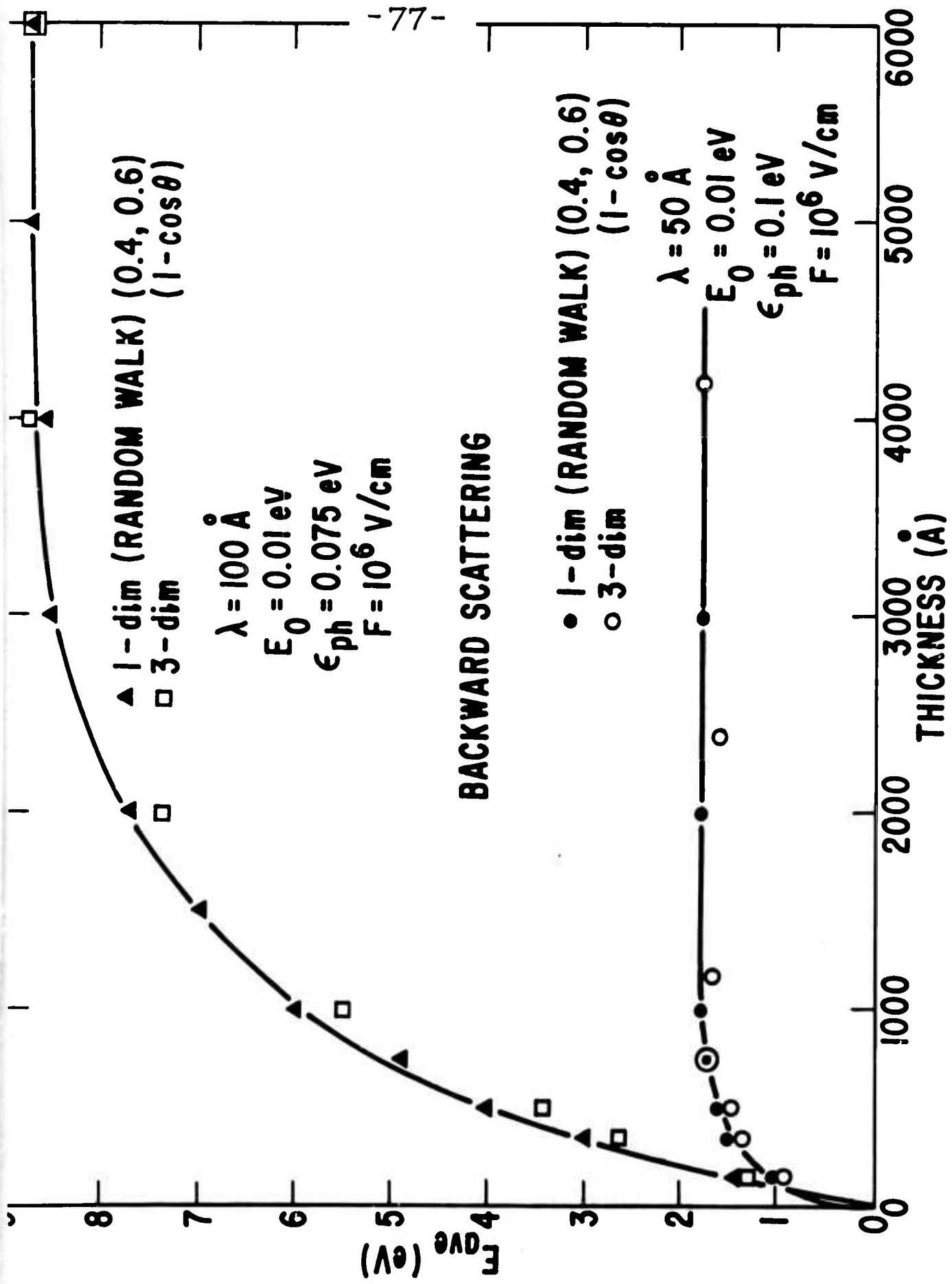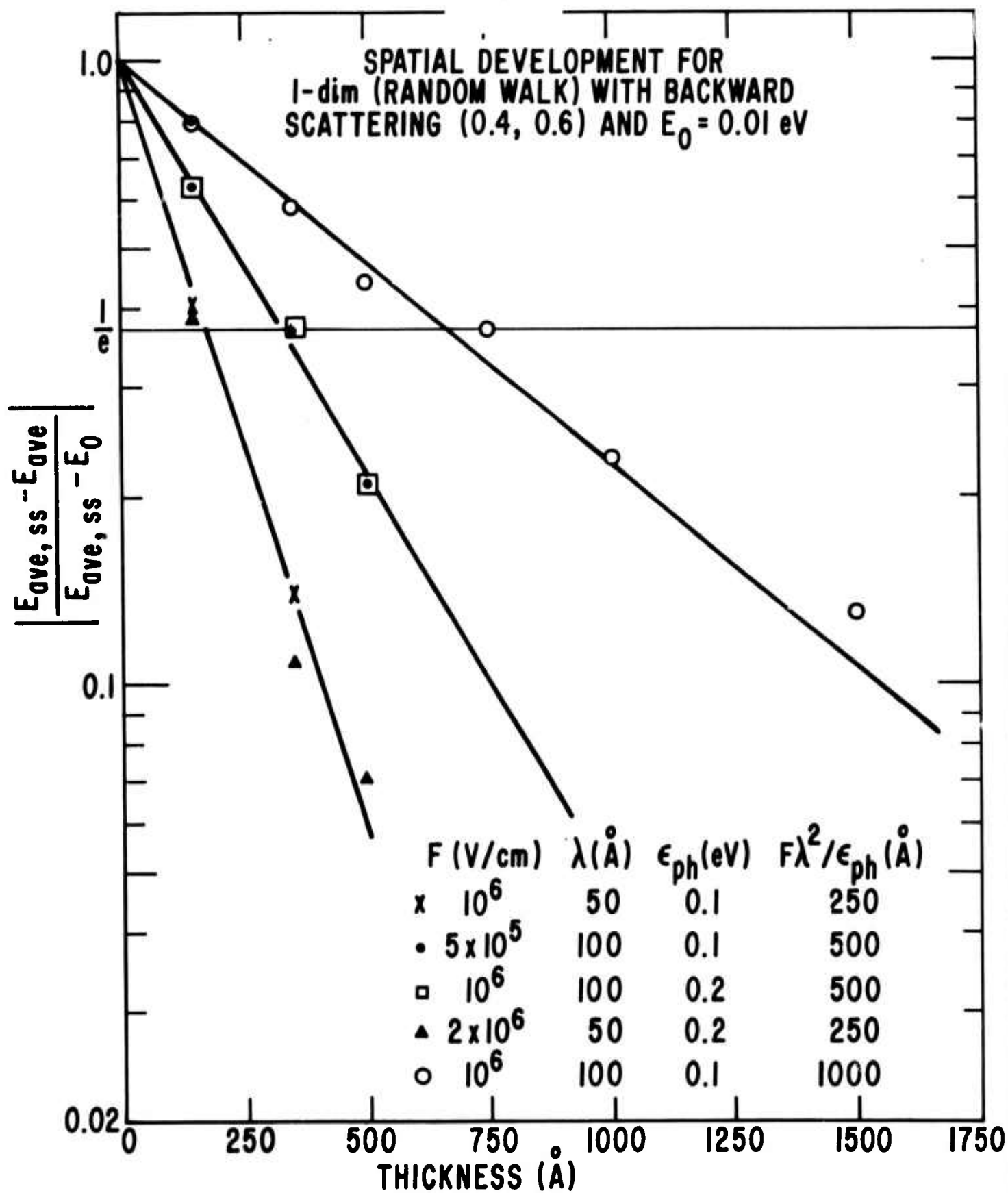of the scattering correctly described by (34) thru (37b). In Fig. 34, we have plotted $E_{ave}$ vs. film thickness t for three cases: $\lambda = 12.5\overset{o}{A}$ giving $E_{ave,ss} = 0.32$ ev, $\lambda = 25\overset{o}{A}$ giving $E_{ave,ss} = 1.89$ ev, and $\lambda = 40\overset{o}{A}$ giving $E_{ave,ss} = 6.66$ ev (for all three cases, $E_o = 0.01$ ev, $\varepsilon_{ph} = 0.1$ ev and $F = 1 \times 10^6$ V/cm). These calculations yeild the scaling law: $E_{ave,ss} = K_{po} (F\lambda)^{8/3}/\varepsilon_{ph}^{5/3}$ with $k_{po} \simeq 3.5$. Figure 35 describes the approach to the steady state with film thickness for five cases of polar-optical scattering with (arbitrarily assumed) constant mfp. Note that, unlike the previous problems plotted in this manner, these curves are not straight lines on the semi-log plot.

## D. Computer and Graphical Results for Energy-Dependent MFP Problems

The final major topic to be considered in this interim report on our hot-electron calculations is the energy-dependent mean free path: $\lambda = \lambda(E)$. This is a particularly important problem because the origin of instability of the distribution function (runaway) lies precisely in a $\lambda(E)$ which increases with E sufficiently rapidly. In the framework of the self-scattering technique there is very little change in the calculation as already described for constant mfp. Once again the time interval between scatterings is given by (25). We now need only know the particle energy E at the time of the collision to assert that the relative probabilities for real scattering and self-scattering respectively are $v(E)/\Gamma\lambda (E)$ and $1 - [v(E)/\Gamma\lambda (E)]$. A random number is used in the usual manner to determine which kind of scattering has occurred.

Up to the present we have studied two simple 'proto-typical' cases of energy-dependent mfp: 1) $\lambda = \lambda_o + \lambda_1\sqrt{E/\varepsilon_{ph}}$, and 2) $\lambda = \lambda_o' + \lambda_o' E/\varepsilon_{ph}$ where $\lambda_o$, $\lambda_o'$ are constant mfp's and $\lambda_1$, $\lambda_1'$ are suitable constants with the dimension of length (we actually used $\lambda_1 = \lambda_1' = 1\overset{o}{A}$). Three kinds of situations have been encountered: i) stability, ii) quasi-stability and iii) run-

AVERAGE ENERGY OF EMERGENCE
FORWARD SCATTERING (POLAR OPTICAL)

$$E_{ave,ss} = k \frac{(F\lambda)^{8/3}}{\epsilon_{ph}^{5/3}}$$

$k = 3.56$
$E_{ave,ss} = 6.66$ eV
$\lambda = 40$ Å

$E_{ave,ss} = 1.89$ eV
$\lambda = 25$ Å
$k = 3.54$

$\epsilon_{ph} = 0.1$ eV
$F = 10^6$ V/cm
$E_0 = 0.01$ eV

$E_{ave,ss} = 0.32$ eV
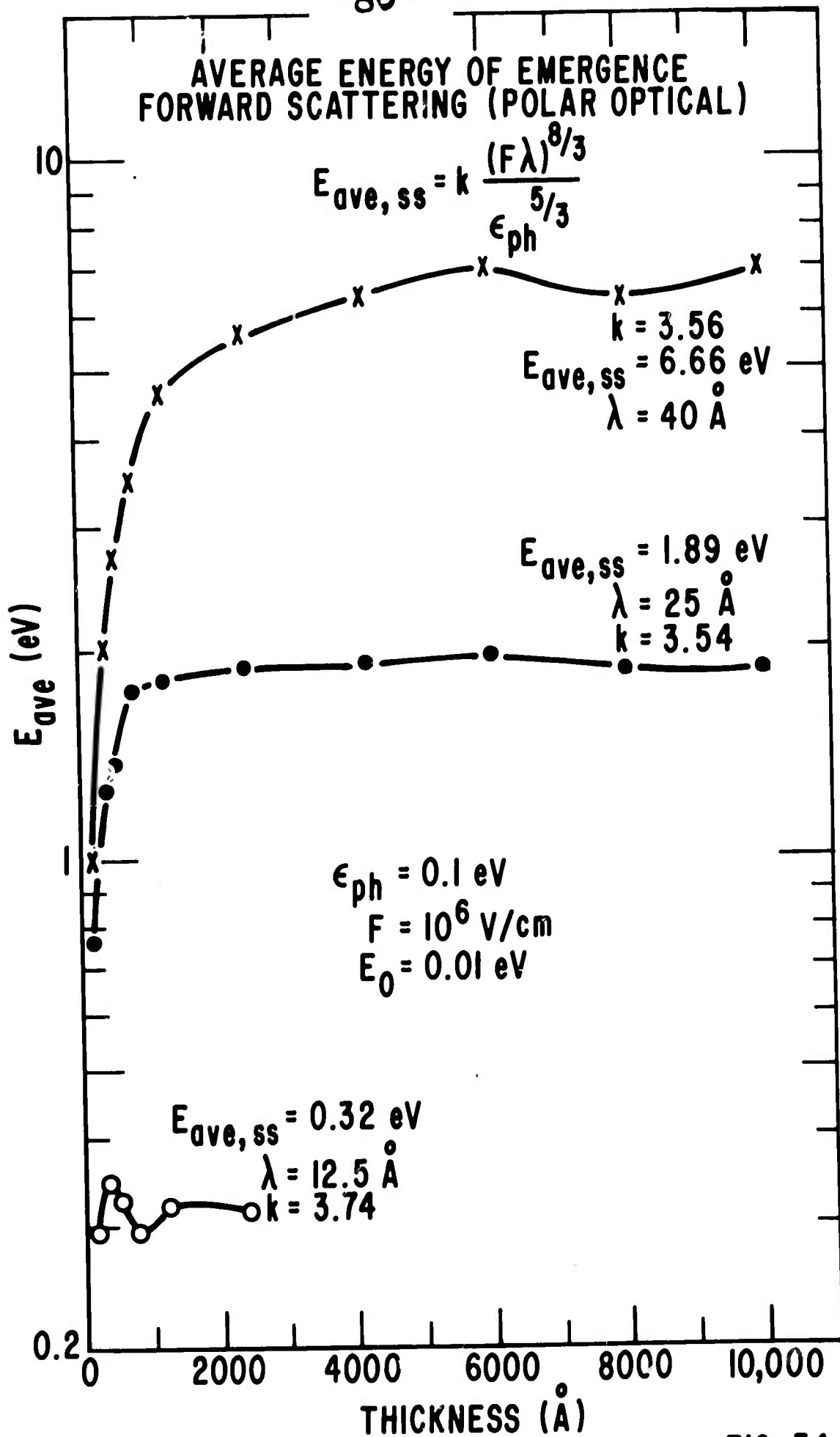$\lambda = 12.5$ Å
$k = 3.74$
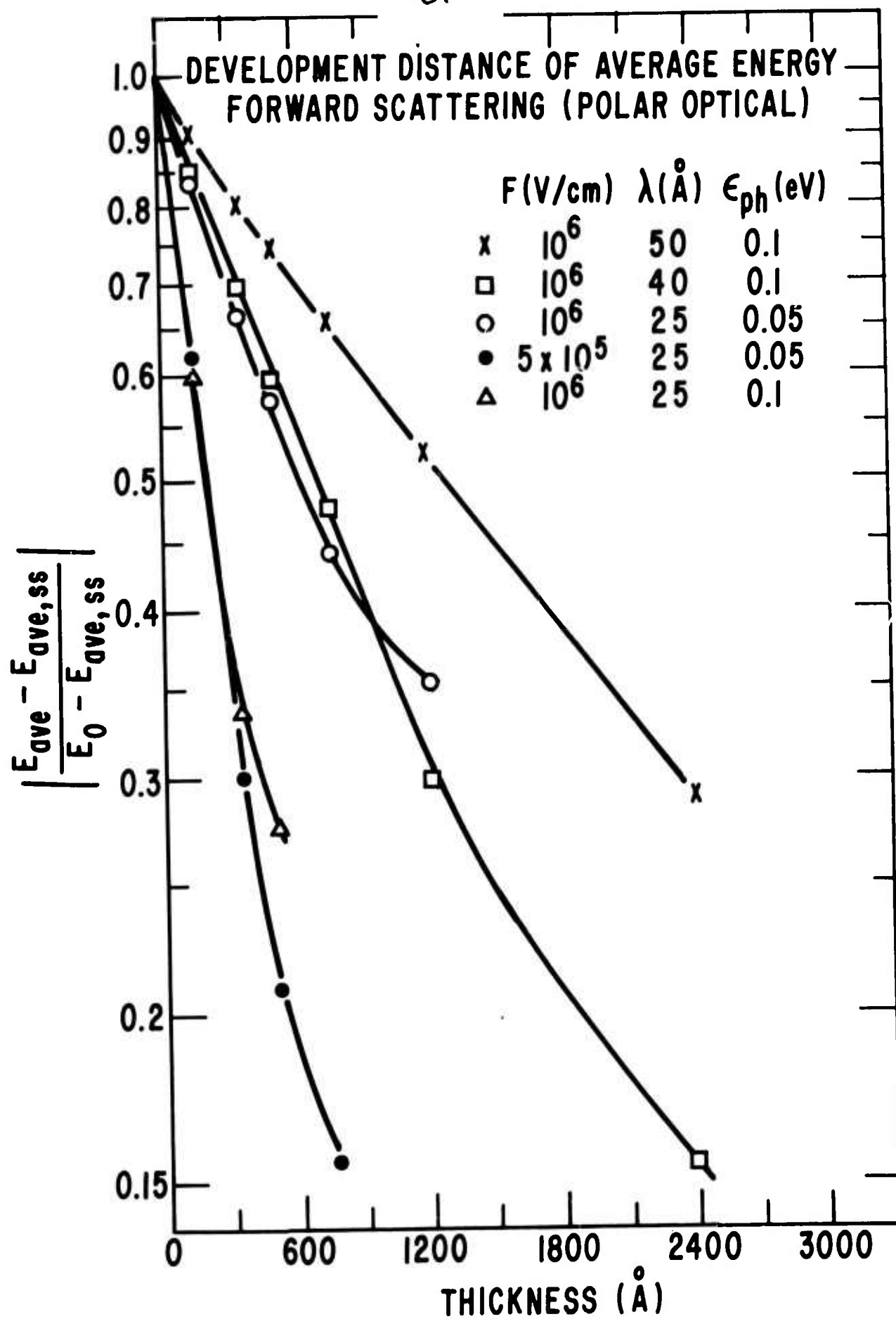
THICKNESS (Å)

FIG. 34

FIG. 35

away.  Further we have found that these three situations can be predicted through graphical solution of the simultaneous equations

$$\lambda = \lambda(E) \qquad \text{and} \quad E_{ave,ss} = E_{ss}(\lambda F, \epsilon_{ph}), \tag{41}$$

where in the latter equation $\lambda$ is taken as a <u>constant</u>.

For the cases studied to-date (excepting polar optical scattering) we have, more specifically, to deal with the pair:

$$\lambda = \lambda(E) \qquad \text{and} \quad E_{ave,ss} = k\,\frac{(F\lambda)^2}{\epsilon_{ph}} \qquad . \tag{42}$$

If there is only one solution to the pair of simultaneous equations then there is a stable steady state.  Such is the situation in Fig. 36, where we have taken $\lambda = \lambda_o + 2\sqrt{E/\epsilon_{ph}}$ (angstroms).  The corresponding $E_{ave}$ vs. t plots, as determined directly from the self-scattering calculations, are exhibited in Fig. 37.  It is seen that the calculated $E_{ave,ss}$ values are very close to those predicted by the graphical intersection points in Fig. 36, namely the heavy dots in Fig. 36.  (The two dots in Fig. 36 for the $\lambda_o = 25\overset{o}{A}$ case correspond to the different starting energies in Fig. 37: $E_o = 4.0$ ev. and $E_o = 0.01$ ev.  The two dots should coincide; their difference is small enough to lack significance.

Figure 38 indicates a situation where there are two intersections or none, namely $\lambda = \lambda_o + \lambda_1\,E/\epsilon_{ph}$ and there are two for $\lambda_1 \lesssim 1$ and none for $\lambda_1 \gtrsim 1$.  In the two-intersection cases, the two points of intersection are wider apart the smaller $\lambda_1$ is. For $\lambda_1$ near 1 the intersection points are close together and the corresponding $E_{ave}$ vs. t plots, exhibited in Fig. 39 are quite erratic – as if the distribution has difficulty making up its mind on what to do – but appears headed for runaway.  This unusual situation (two close intersection points) certainly needs further study.  On the other hand with widely separated intersection points, $\lambda_1 = 0.5$, we see from the $E_{ave}$ vs. t plots in Fig. 40 that there is at least quasi-stability.  Finally, with $\lambda_1 = 2$ in

AVERAGE ENERGY OF EMERGENCE
STEADY STATE; STABLE EQUILIBRIUM
ISOTROPIC SCATTERING

$$\lambda \propto \sqrt{\frac{E}{\epsilon_{ph}}} + \text{CONSTANT}$$

$$E_{ave,ss} = k\,\frac{(F\lambda)^2}{\epsilon_{ph}}$$

NUMBER OF PARTICLES; 200
$\epsilon_{ph} = 0.1$ eV
$F = 10^6$ V/cm

$\lambda = 40\,\overset{\circ}{A} + 2\sqrt{\dfrac{E}{\epsilon_{ph}}}$

$\lambda = 25\,\overset{\circ}{A} + 2\sqrt{\dfrac{E}{\epsilon_{ph}}}$

E (eV)

$\lambda$ (Å)

FIG. 36

FIG. 37

QUASI-STEADY-STATE; UNSTABLE EQUILIBRIUM
ISOTROPIC SCATTERING

$$\lambda \propto \frac{E}{\epsilon_{ph}} + CONSTANT$$

$$E_{ave,ss} = k \frac{(F\lambda)^2}{\epsilon_{ph}} \rightarrow$$

$$\lambda = \lambda_0 + 0.9 \frac{E}{\epsilon_{ph}} \rightarrow$$

$$\lambda = \lambda_0 + \frac{E}{\epsilon_{ph}}$$

$$\lambda = \lambda_0 + 0.8 \frac{E}{\epsilon_{ph}} \rightarrow$$

$$\lambda = \lambda_0 + 2.0 \frac{E}{\epsilon_{ph}}$$

$$\lambda = \lambda_0 + 0.7 \frac{E}{\epsilon_{ph}} \rightarrow$$

$$\lambda = \lambda_0 + 0.5 \frac{E}{\epsilon_{ph}}$$

$$F = 10^6 \ V/cm$$

$$\epsilon_{ph} = 0.1 \ eV$$

NUMBER OF PARTICLES; 200

E (eV)

$\lambda (\mathring{A})$

FIG. 38

FIG. 39

ENERGY DEPENDENT MEAN-FREE-PATH
ISOTROPIC SCATTERING

$$\lambda = \lambda_0 + 0.5 \frac{E}{\epsilon_{ph}}$$

$E_0 = 16$ eV

$E_0 = 4.0$ eV

$E_0 = 0.01$ eV

NUMBER OF PARTICLES; 200
$\epsilon_{ph} = 0.1$ eV
$\lambda_0 = 25$ Å
$F = 10^6$ V/cm
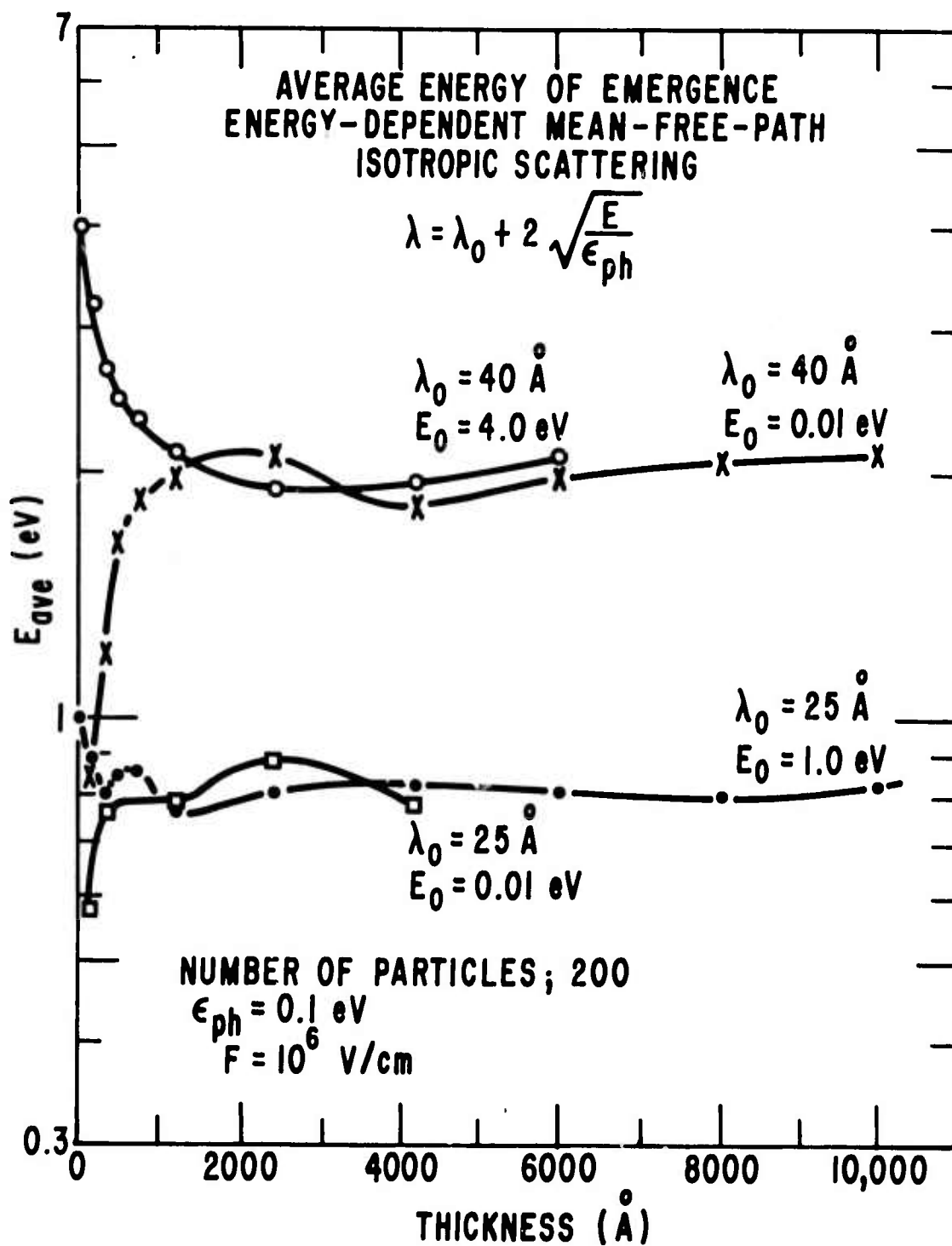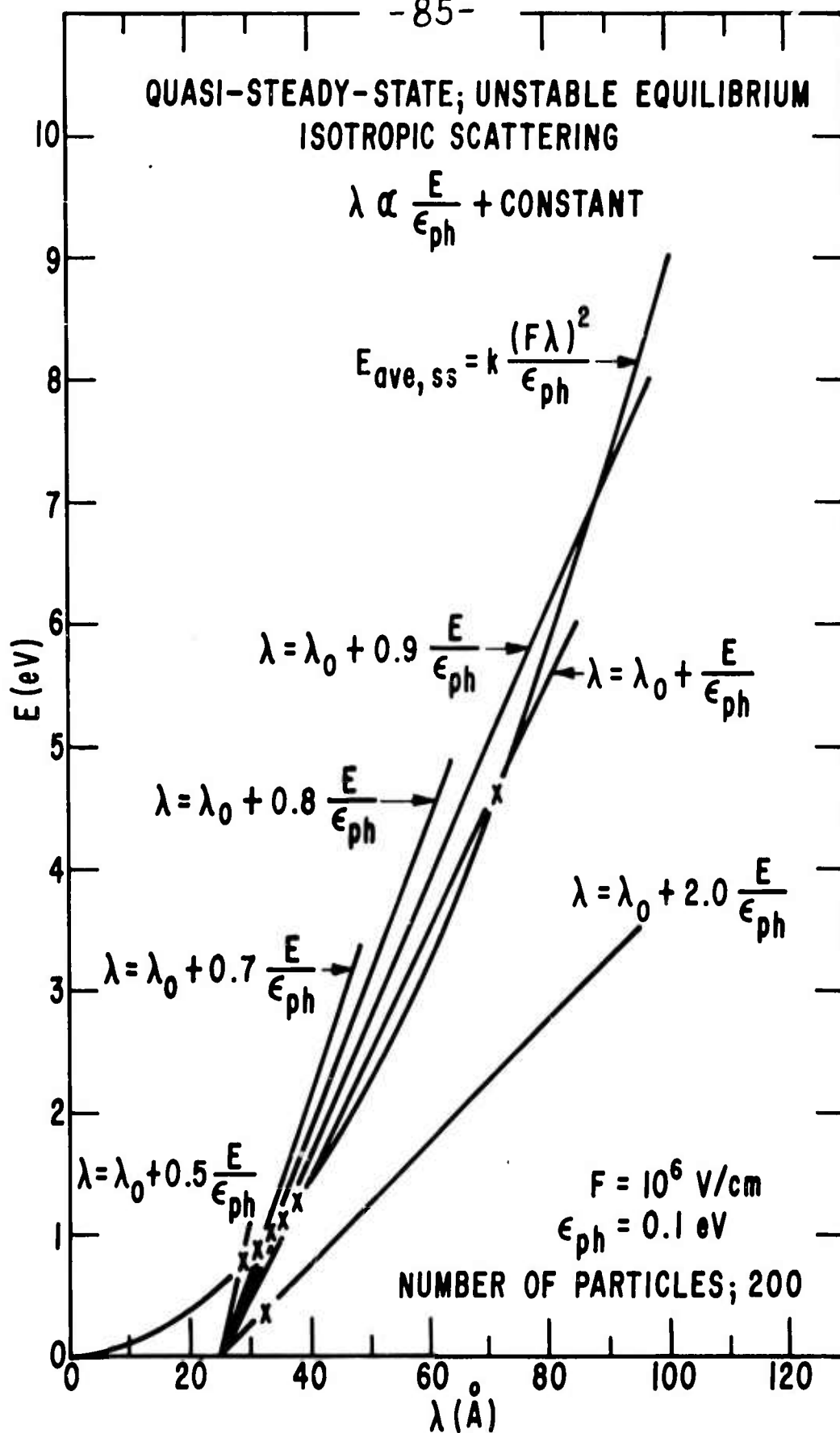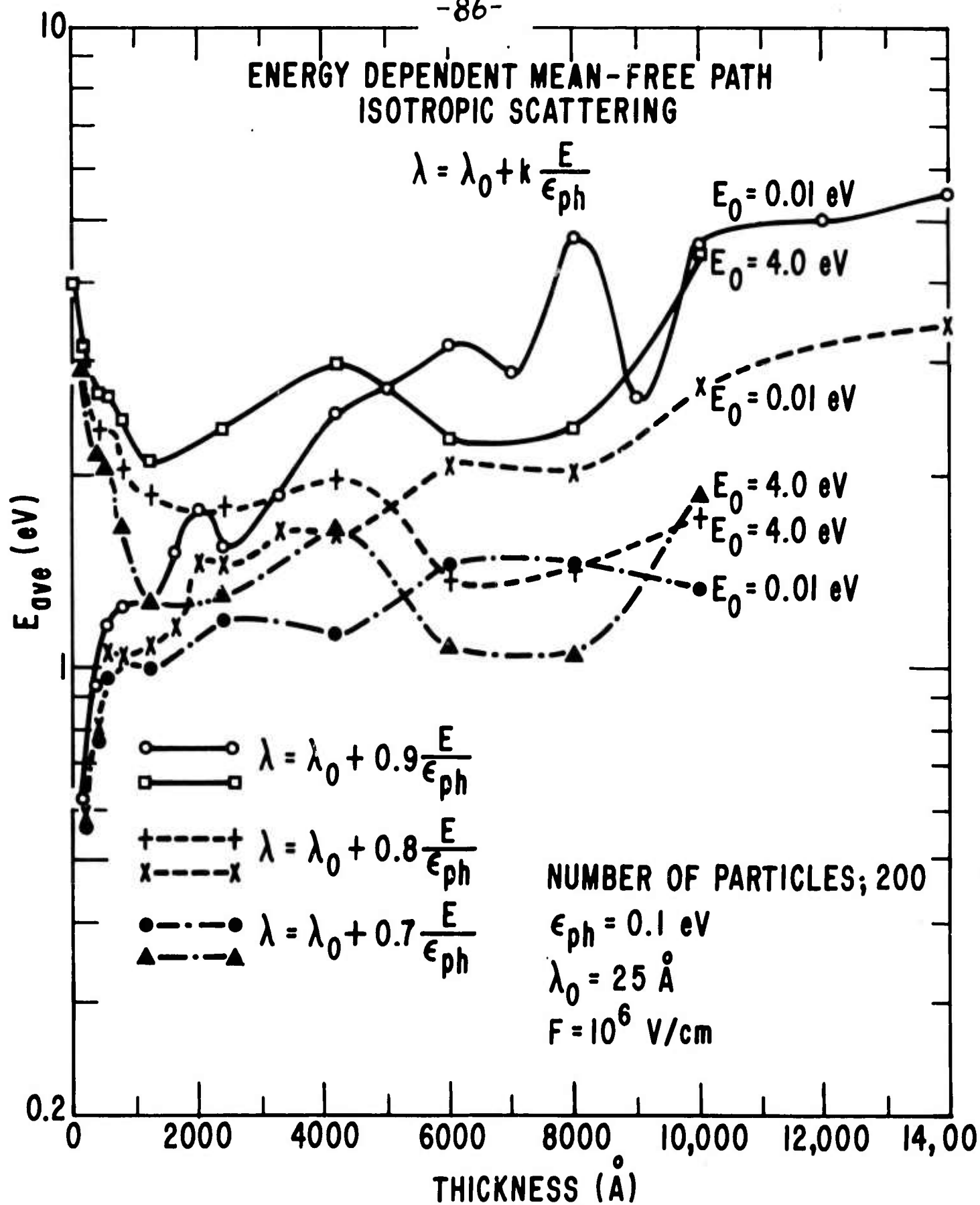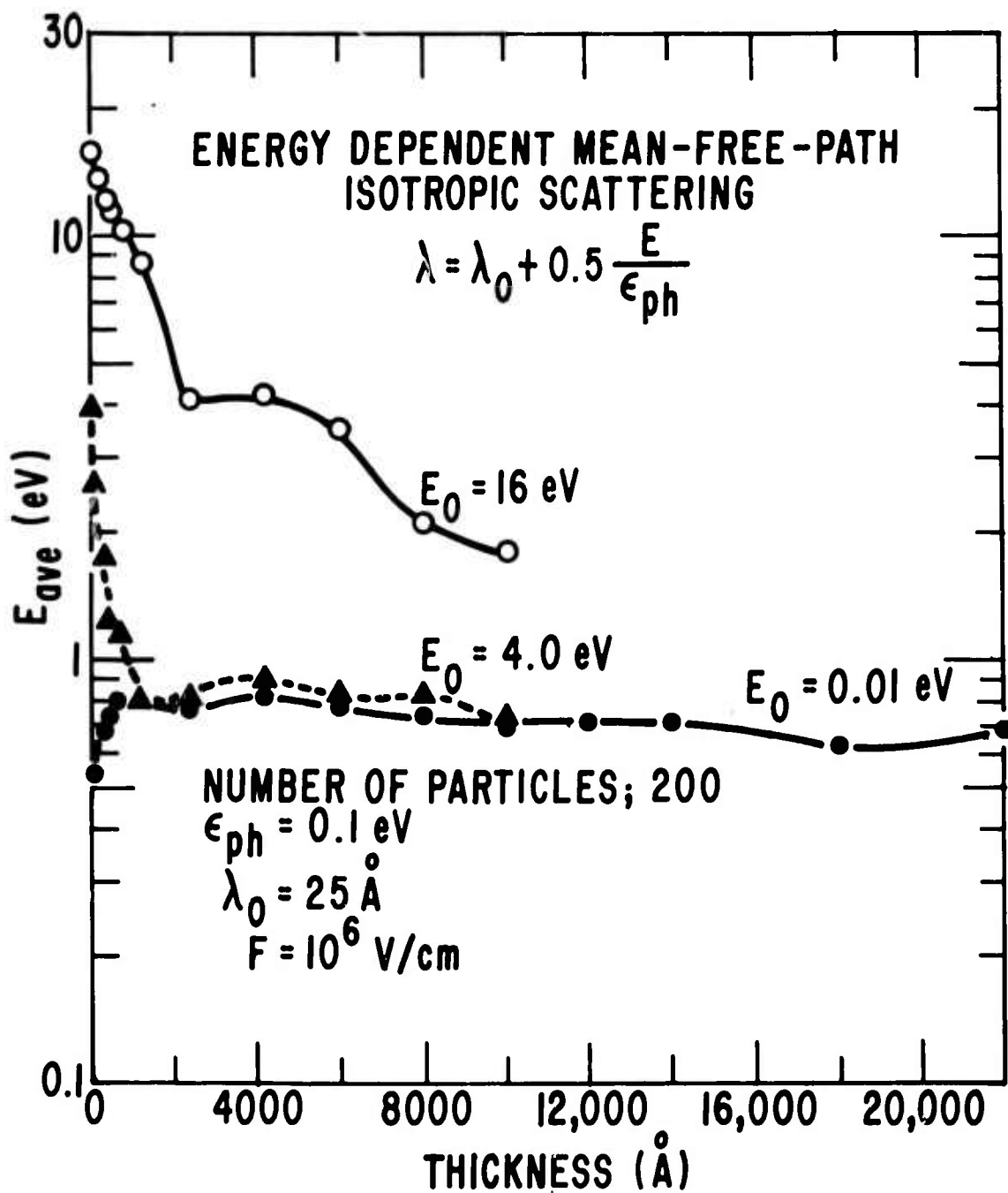
FIG. 40

Fig. 38, there are no intersection points and accordingly the distribution simply runs away, as is clearly visible in the $E_{ave}$ vs. t plot in Fig. 41.

The energy-dependent mean-free-path studies reported here are fragmentary in nature. Since this case is technologically an important one, more systematic studies will be made. It remains to be seen whether the one-dimensional simulations, either random walk or non-random walk, will prove as useful for the study of this class of problems.
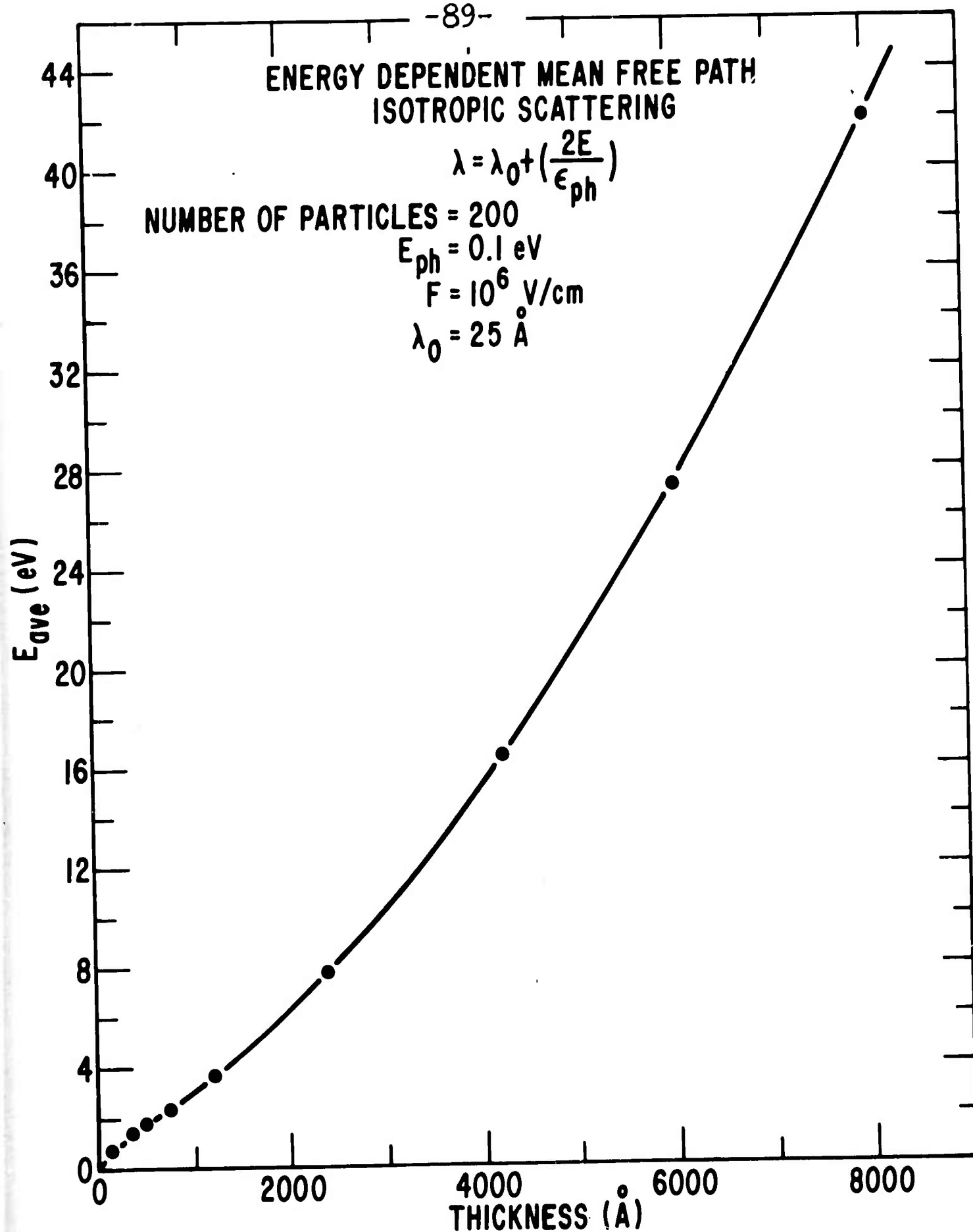
ENERGY DEPENDENT MEAN FREE PATH
ISOTROPIC SCATTERING

$$\lambda = \lambda_0 + \left(\frac{2E}{\epsilon_{ph}}\right)$$

NUMBER OF PARTICLES = 200
$E_{ph} = 0.1$ eV
$F = 10^6$ V/cm
$\lambda_0 = 25$ Å

FIG. 41

## References

1. A. M. Goodman, Phys. Rev. 152, 780 (1966).
   R. J. Powell & G. F. Durbenwick, IEEE Trans. NS-18, 99, (1971).
   J. F. Verwey, Jour. Appl. Phys. 43, 2273 (1972) and Appl.
   Phys. Lett. 21, 417 (1972).

2. T. H. DiStefano and D. E. Eastman, Phys. Rev. Lett. 27, 1560 (1971).

3. G. Carter and J. S. Colligon, Ion Bombardment of Solids
   (Heineman, London, 1968).

4. C. W. White and N. H. Tolk, Phys. Rev. Lett., 26, 486 (1971).

5. R. Williams and M. H. Woods, private communication.

6. C. N. Berglund, IEEE Trans. Electron Dev., ED-13, 701 (1966).

7. T.H. DiStefano, Appl. Phys. Lett. 19, 280 (1971).
   R. Williams and M. H. Woods, Jour. Appl. Phys. 43, 4142 (1972).

8. D. V. McCaughan and V. T. Murphy, IEEE Trans. Nuclear Sci.,
   NS-19, 249 (1972).

9. E. H. Nicollian, private communication.

10. M. M. Shahin, Photographic Sci. and Eng., 15, 322 (1971)

11. N. Klein and H. Gafni, IEEE Trans. Electron Devices ED-13,
    281 (1966).
    N. Klein, "Electrical Breakdown in Solids", Adv. in Electronics
    and Electron Physics 26 , 1969, Academic Press, N.Y.

12. J. E. Carnes, Final Report, Contract N00019-70-C-0129, Naval
    Air Systems Command, Department of the Navy, Wash., D.C.
    (pp. 32-51).
    J.E. Carnes and M.T. Duffy, Hour. Appl. Phys. 42, 4350, 1971.

13. N. Klein, IEEE Trans. ED-13, 788 (1966).

14. A. von Hippel, E. P. Gross, J. G. Jelatis, and M. Geller,
    Phys. Rev. 91, 568 (1953).

15. M. D. Tabak and P. J. Warter, Phys. Rev. 173, 899 (1968).

16. A. Rose, Concepts in Photoconductivity and Allied Problems
    (Wiley, New York, 1963).

17. M. A. Lampert and P. Mark, Current Injection in Solids
    (Academic Press, New York, 1970).

18. An elementary exposition will be found in "Monte Carlo Methods"
    by J. M. Hammersley and D. C. Handscomb (Methuen, Wiley, N.Y.,
    1964).
    A variety of applications of the method will be found in "Methods
    in Computational Physics, Volume 1: Statistical Physics"
    (Academic Press, N.Y., 1963). An extensive bibliography will
    be found in the University of California Lawrence Radiation
    Laboratory Report UCRL-7823, "Monte Carlo Methods, A Bibli-
    ography: 1949-1963." In the context of the hot-electron

18. (continued)

transport problem, see T. Kurosawa, Jour. Phys. Soc. of Japan 20, 937 (1965) and also Proc. Int'l Conf. Phys. of Semicond., Kyoto 1966, p. 424 (also published as the Jour. Phys. Soc. of Japan, 21, Supplement, 1966).

19. H. D. Rees, Physics Letters 26A, 416 (1968) and J. Phys. Chem. Solids 30, 643 (1969).

20. R. V. Martinelli and E. D. Savoye, Quarterly Progress Report No. 6, Contract No. DA 44-009 AMC-1276 (T), U.S. Army Mobility Equipment Research and Development Center, Fort Belvoir, Va.

21. D.J. Howarth and E. H. Sondheimer, Proc. Roy. Soc. 219, 53 (1953). W. P. Dumke, Phys. Rev. 167, 783 (1968).

22. P. A. Wolff, Phys. Rev. 95, 1415 (1954).